

AKARI and Spinning Dust Emission
A look at microwave dust emission via the Infrared
Doctoral Thesis
Submitted to The University of Tokyo
DRAFT

Aaron Christopher Bell

December 7, 2017

Contents

2	1 Introduction	2
3	1.1 All-sky Astronomy	2
4	1.2 Infrared astronomy	2
5	1.3 Microwave foregrounds	5
6	1.3.1 Anomalous Microwave Emission	6
7	1.3.2 Proposed explanations	9
8	1.3.3 Excitation factors	11
9	1.3.4 AME vs. IR in the literature	12
10	1.4 Scope of this Dissertation	13
11	1.4.1 An application of all-sky archival data	13
12	1.4.2 Testing the spinning PAH hypothesis	13
13	1.4.3 Limitations	13
14	1.4.4 Code availability	14
15	2 Data Sources	15
16	2.1 A collection of skies	15
17	2.2 AKARI	16
18	2.2.1 AKARI/Infrared Camera (IRC)	16
19	2.2.2 The AKARI Far Infrared Surveyor (FIS)	20
20	2.2.3 Planck Observatory High Frequency Instrument (HFI)	20
21	2.3 Infrared Astronomical Satellite (IRAS)	21
22	2.4 Planck COMMANDER Parameter Maps	22
23	2.4.1 Synchrotron	22
24	2.4.2 Free-free emission	22
25	2.4.3 Thermal dust emission	24

26	2.4.4	AME data	24
27	2.5	All-sky Data Processing	29
28	3	Analysis of an interesting AME region: λ Orionis	31
29	3.1	An interesting AME region	31
30	3.1.1	Where does the ring come from?	31
31	3.1.2	A well-studied region	32
32	3.2	Investigative approach	32
33	3.3	Data preparation	35
34	3.3.1	Extraction from HEALPix maps	35
35	3.3.2	Point-source and artifact masking	35
36	3.3.3	PSF Smoothing	36
37	3.3.4	Background subtraction	37
38	3.4	Multi-wavelength characterization	37
39	3.4.1	Bootstrap analysis	40
40	3.5	Comparison with SED Fitting	40
41	3.5.1	Comparison with unmasked results	45
42	3.6	Discussion	45
43	3.6.1	PAH Ionization fraction	46
44	4	All-sky Analysis	48
45	4.1	Resolution matching	48
46	4.2	All-sky cross correlations	49
47	4.3	Masked Comparison	51
48	4.3.1	Pixel mask	51
49	4.4	Spatial variation of correlations	55
50	4.5	Discussion	55
51	4.5.1	AME:Dust	55
52	4.5.2	AME:PAH	60
53	4.5.3	AME: T, G_0	60
54	4.5.4	Microwave foreground component separation	61

⁵⁵ List of Figures

56	1.1 An example of a potential makueup of microwave emission components. Photometry	
57	points are extracted from the Planck and WMAP all-sky maps (Planck Collaboration	
58	et al. 2014b), for a part of the region well-known for prominent AME, ρ Ophiuchus	
59	(Planck Collaboration et al. 2011b). The AME curve is produced from a warm neutral	
60	medium spinning dust template (Ali-Haïmoud et al. 2009), with a frequency-shift	
61	applied to approximately fit the microwave data s in Planck Collaboration et al. (2016b)	7
62	1.2 Two AME prominent regions investigated by Planck Collaboration et al. (2011b);	
63	Tibbs et al. (2011), ρ Ophiuchus and Perseus, as they appear in the PAH-feature-	
64	tracing AKARI/IRC $9\mu\text{m}$ all-sky data at native resolution (Ishihara et al. 2010). White	
65	contours show AME at 1-degree resolution, extracted from the map by Planck Col-	
66	laboration et al. (2016b). The IRC data shown here is of a much finer resolution than	
67	the AME data, at around $10''$, demonstrating the critical gap in resolvability of all-sky	
68	AME-tracing data itself vs. the IR dust tracers we hope to compare it to.	8
69	2.1 Relative spectral response curves of the bands used in this study. Expected dust emis-	
70	sion components, assuming the dust SED model by (Compiègne et al. 2011) are also	
71	shown. The components are summarized as emission from big grains (BGs, dashed	
72	yellow line), emission from very small grains (VSGs, dashed blue line), and emission	
73	from PAHs (dashed grey line).	16
74	2.2 The I12 (orange) and A9 (green) filters coverage of modeled ionized (PAH1, red) and	
75	neutral (PAH0, purple)components of PAH features by Compiègne et al. (2011). The	
76	difference in the PAH feature coverage mainly comes from the $6.2\ \mu\text{m}$ and $7.7\ \mu\text{m}$	
77	feature.	17

78	2.3	Coverage of MIR wavelengths by the filters used in this work. An Spitzer/IRS spec-		
79		trum (see AOT4119040) of the galactic plane (thin blue line) demonstrates how IRC		
80		and IRAS photometric bands trace these features on an all-sky basis (Ishihara et al.		
81		2007). Strong PAH features overlap with the A9 and I12, while the A18 and I25		
82		micron bands only trace much weaker features.	18	
83	2.4	Ionization fraction of PAHs vs. band ratios of I12, I25, W12, W25 vs. A9, for three		
84		ISRF strengths: Top: $G_0 = 100$, Middle: $G_0 = 1000$, and Bottom: $G_0 = 10000$.		
85		These ratios are determined by assuming the SED template of Compiègne et al. (2011)	19	
86	2.5	AKARI/IRC 9 μm to IRAS 12 μm intensity ratio.	20	
87	2.6	AKARI/IRC 9 μm to IRAS 25 μm intensity ratio.	21	
88	2.7	r_s cross correlation matrix of the PCCS maps: temperature T , emissivity index β , and		
89		amplitude at 545 GHz $I_{dust}(545)$ of thermal dust; intensity of free-free emission ff		
90		at ; intensity of synchrotron emisison at 4 MHz $Sync$; intensity of the AME var. freq.		
91		component AME at 22.8 GHz.	23	
92	2.8	The peak frequencies of the varying component AME_{var} . The pink shaded re-		
93		gion indicates frequencies not covered by either WMAP or Planck The green line		
94		at 33.5 GHz indicates the peak frequency of AME_{fix}	25	
95	2.9	Histograms of the peak intensity AME maps calculated from the original COMMANDER-		
96		AME reference frequency maps. The dominant component, AME_{var} is indicated in		
97		blue, for all pixels in the map, with their spinning dust intensities evaluated their peak		
98		frequencies (see Fig. 2.8.) AME_{fix} gives the peak intensity of the spatially-constant		
99		frequency component, indicating it is essentially always the weaker component. . . .	26	
100	2.10	All-sky map of the peak frequencies of the varying component AME_{var} , correspond-		
101		ing to Fig. 2.8. Virtually all of the purple regions of the map correspond to pixels		
102		flagged for point sources in the LFI data. There are very few notable structures in the		
103		frequency map overall, other than the galactic plane itself, ρ Ophiuchus, and Perseus.	27	
104	2.11	Spdust template spinning dust profiles fitted by PC15X when calculating AME_{var} .		
105		The reference frequency, 22.8 GHz is indicated by the vertical green line. Each tem-		
106		plate has the same AME_{var} amplitude of 100 μK , indicated by the horizontal green		
107		line, plotted to highlight the potential deviation between AME_{var} and the actual peak		
108		intensity.	28	

109	2.12 All-sky map of the ratio of two COMMANDER components- the frequency-varying	
110	AME component divided by the intensity of thermal dust emission at 545 GHz. There	
111	are some recognizable AME emission regions, such as λ Orionis. Large-scale patches	
112	of AME excess are noted to correspond to synchrotron emission (Hensley et al. 2016)	29
113	3.1 λ Orionis as it appears in the AKARI 9 μm data. Contours indicate the AME, as given	
114	by the Planck PR2 AME map. The image is smoothed to a 1° PSF (much larger than	
115	the original 10 arcsec map). The λ Orionis star itself is approximately located at the	
116	center of the image.	33
117	3.2 λ Orionis as it appears in H-alpha emission by ?. Contours indicate AME emis-	
118	sion, from the variable frequency component. The colorbar indicates $H\alpha$ emission in	
119	Rayleighs. The field of view is slightly larger than that used for the IR comparison. .	34
120	3.3 Th λ Ore ionis region and its surroundings in AKARI FIS data, where A65 is blue,	
121	A90 is green, and A140 is red. The missing stripe patterns are visible, and affect all 3	
122	bands shown here as well as the A160 data.	36
123	3.4 A grid of thumbnails showing the λ Orionis region's structure, at 12 wavelengths,	
124	along with AME contours (shown in white countours. Spatial correlation seems to be	
125	the best at the shortest and longest wavelengths (AKARI/IRC 9 μm and Planck/HFI	
126	550 μm). The images are smoothed and interpolated for demonstration. Figure 3.1	
127	demonstrates the actual pixel grid used for the SED fitting and intensity correlation	
128	tests.	38
129	3.5 r_s correlation matrix for all of the data used in the λ Orionis analysis, similar to that	
130	presented for the Planck Commander component maps in Fig. 2.7. The shade and an-	
131	notation for each cell indicates the r_s score, where r_s of 1 indicates a monotonically	
132	increasing relationship for a given pair of images. The two AME components, as de-	
133	scribed in Ch. 2, are listed separately: AME_{var} for the frequency-varying component,	
134	and AME_{fix} for the constant frequency component.	39
135	3.6 Re-sampled (Bootstrap) correlation tests for IR emission in λ Orionis vs. AME, for	
136	both Spearman and Pearson correlation tests.)	41

137	3.7 Observed (black circles and errors) and synthetic photometry (gray dots) SED of a pixel within λ Orionis, along with the dust SED model fit results. Two SED fits are shown: one for the Bayesian fitting (magenta), and another showing the standard least-squares result for comparison (yellow). The fitted ISRF strength U , and fraction of mass in PAHs, q_{PAH} are also given.	42
142	3.8 The same as Fig. 3.7, but for a different pixel position. Corresponds to galactic coordinates.	43
144	3.9 Scatter plot with error ellipses generated through the Bayesian SED fitting, of total dust mass M_{dust} vs. I_{AME} scaled by U	43
146	3.10 The same comparison is given by 3.9, but showing total mass of PAHs (M_{PAH}) rather than total dust mass on the y-axis.	44
148	3.11 The same as in Figs. 3.9 and 3.10 , but specifically comparing an estimate of the ionized component of PAH mass.	44
150	3.12 Intensity cross-correlation for all pixels in the λ Orionis cut-out region. r_s indicates the Spearman rank correlation coefficient for each plot.	45
152	3.13 The Bayesian correlation probability distributions of Pearson's correlation coeffo- coemt (ρ) for the three physical parameters vs. the AME intensity: total dust mass, rho_{dust} (red); total PAH mass rho_{PAH} (green); and only the ionized PAH mass rho_{PAH+} (blue). Also given are the probabilities of either PAH component being better correlated with AME than dust mass, as well as the probability that ionized PAH mass correlates better than total PAH.	46
158	4.1 Point-density distributions of the AME intensity (Y-axis) vs. the IR bands' intensities. Darker regions indicated higher pixel densities. Only a simple mask of pixels near the ecliptic plane has been applied.	49
161	4.2 ALL-SKY cross-correlation matrix for the 12 infrared bands sampled, as well as the PC component maps described in Ch. 2: the two AME components evaluated at their peak frequencies AME_{var} , AME_{fix} ; Syncrotron, and free-free), and ancillary maps of N_H , H_α emission, and 408 MHz emission Haslam et al. (1982). The color-scale indicates (r_S). Results are based on the unmasked sky, but are split by Galactic latitude: pixels with $ \beta < 15deg$ (left) and $ \beta > 15deg$. The color and annotations indicate r_s as in Fig. 3.5.	50

168	4.3	All-sky map in A9 emission after applying the combined masks: ecliptic plane, galactic plane, point sources, and pixels with S/N < 1. This mask essentially outlines the galaxy, except for the most confused regions.	51
169			
170			
171	4.4	The same comparison as shown for Fig. 4.1, but with the mask applied as in Fig. 4.3.	52
172			
173	4.5	Similar comparison to Fig. 4.1, with the IR intensities scaled by U for each pixel.	53
174			
175	4.6	Cross-correlation (r_s) matrix for the IR intensities (unscaled) vs. each other, essentially the same comparison as in Fig. 4.2, except that the pixel mask is applied.	54
176			
177	4.7	Cross-correlation (r_s) matrix for the U -normalized IR intensities vs. each other, and also against the AME components, other PC products, and ancillary data. Only the IR maps are divided by U - other data is unchanged from Fig. 4.6)	54
178			
179	4.8	55
180			
181	4.9	Spatial map of r_s between the AME and IR intensity for 4 bands: $9 \mu m$, $12 \mu m$, $25 \mu m$, and $140 \mu m$. r_s is calculated for all NSIDE 256 pixels within each NSIDE 8 pixel-sized bin.	56
182			
183	4.10	56
184			
185	4.11	57
186			
187	4.12	57
188			
189	4.13	Spatial map of r_s between the AME and IR intensity as in Fig. ??, but with the AME and IR maps first normalized by dust radiance R	58
190			
191	4.14	58
192			
193	4.15	59
190	4.16	59
191			
192	17	Explained variance decline for principal component analysis performed on a set of 12 all-sky infrared maps. The first three components account for over 99% of the total variance. The PCA fit is performed on the whole sky, after whitening the data, using the “scikitlearn”	63
193			

¹⁹⁴

Chapter 1

¹⁹⁵

Introduction

¹⁹⁶

“It is now plain that about 75% of the data we would like to have can be obtained from good

¹⁹⁷

ground-based sites”

¹⁹⁸

-H. Johnson, 1966

¹⁹⁹

1.1 All-sky Astronomy

²⁰⁰

All-sky astronomy is not new. Indeed, the notion of capturing a particular “object” or “source” with a camera and saving it for later investigation would be completely alien to the first astronomers and astronavigators. Absence of telescopes forced us to describe the sky in terms of its larger patterns, brightest characters. What is new however is the notion of preparing an archive of the sky itself for not only the research whims of a single investigator, team, institute, or even a single nation rather, all-sky surveys tend to be international endeavors in their production, and even more so in their utilization.

²⁰⁶

1.2 Infrared astronomy

²⁰⁷

Infrared astronomy was essentially non-existent as recently as the 1920s, if we judge by the first IR observations (Pettit & Nicholson 1922, 1928). Mainstream IR astronomy is perhaps much younger, only really taking off — literally — in the post-war era, via balloon and rocket borne experiments (Johnson 1966). Compare this to visible wavelengths, a field so old we name it after the bio-evolutionary advent of sight, itself. Even radio astronomy with its own logistical and technological challenges, has been around since at least 1932.

²¹³

Astronomers have not been content to be constrained by atmospheric IR windows, even from the

TABLE 1.1 Timeline of all-sky surveys

1983	IRAS	Neugebauer et al. (1984)
1989	COBE	Boggess et al. (1992)
1990	ROSAT	Truemper (1982)
2001	WMAP	Bennett et al. (2003b)
2003	2MASS	Skrutskie et al. (2006)
2003	GALEX	Martin et al. (2005)
2006	AKARI	Murakami et al. (2007)
2008	Fermi	Atwood et al. (2009)
2009	Planck	Planck Collaboration et al. (2011a)
2009	WISE	Wright et al. (2010)

214 best of ground-based sites. Or perhaps interests have shifted so dramatically since 1966, that all of
 215 the investigations enabled by rocket-based, space-based, even Boeing 747-based IR astronomy (e.g.
 216 SOFIA, the Stratospheric Observatory for Infrared Astronomy, Young et al. (2012)) would have bored
 217 75% of astronomers in the '60s. The meaning of "far infrared" has even redshifted, so to speak, from
 218 the Johnson (1966) definition of "4 to 22 um" — consider the "Far Infrared Surveyor" instrument
 219 onboard the AKARI satellite (Murakami et al. 2007), which observed from 50 to 180 μm (Kawada
 220 et al. 2007a)

221 For our purposes, we consider the FIR to cover 60 to 550 μm , partially out of convenience—
 222 FIR bands, in this paper, means the Infrared Astronomical Satellite (IRAS) 60 and 100 μm (Neuge-
 223 bauer et al. 1984), all four FIS bands, and the Planck Observatory's High Frequency Instrument
 224 (HFI) 857 GHz and 545 GHz bands (Planck Collaboration et al. 2011a, 2014b). The two AKARI
 225 Infrared Camera (IRC) (Onaka et al. 2007; Ishihara et al. 2010) bands and the IRAS 12 and 25 μm
 226 bands we will refer to collectively as the mid-infrared (MIR) bands.

227 The ability to map and archive the sky with satellites - not only in the optical and infrared, but
 228 well into the microwave regime — has enabled interdisciplinary research of the ISM. The merits
 229 of multiwavelength based investigations arise from the simple fact that the ISM is very complex—
 230 both in terms of the myriad forms of matter present, from plasmas to dust grains — and in countless
 231 physical processes at play. Consider the complex case of a supernova remnant influencing surrounding
 232 ISM: through a combined analysis of radio, mid-far infrared, and X-ray data, Lau et al. (2015) were
 233 able to characterize the history of dust production, heating, and destruction within the Sgr A East
 234 supernova remnant.

In the case of interstellar dust emission, especially, multi-wavelength analysis is crucial to understanding the individual components of interstellar dust emission. If we assume that grains in local thermal equilibrium emit in an essentially classical manner, we will quickly become frustrated by multi-band IR observations. It is believed that factors such as variations in the optical properties of dust grains leads to a deviation from blackbody emission. The intensity of such emission has come to be represented by a “modified blackbody” function, provided in Onaka et al. (1999) as follows:

$$I_d(\nu) \propto \nu^{\beta_d} B_\nu(T_d), \quad (1.2.1)$$

where β is known as the “emissivity index”, and T_d is the dust temperature. Tracing this emission from microwave to IR wavelengths, in the diffuse Milky Way, Planck Collaboration et al. (2016d) find a typical value of 1.6 ± 0.1 for β , and 19.4 ± 1.3 K for the dust temperature (assuming a single temperature component).

Even after adopting a modified blackbody, we will still be unable to explain dust emission if we include wavelengths from the mid to Far-IR. A modified blackbody underestimates dust emission on the Wiens side, such as that traced by IRAS, an effect first reported by Boulanger et al. (1985), and also found later in data collected by the Cosmic Background Explorer (COBE)’s Diffuse Infrared Background Experiment (Sodroski et al. 1987, 1994). This excess cannot be explained by temperature variations of grains large enough to be in thermal equilibrium, and likely comes from a smaller population of interstellar dust grains (Purcell 1976; Sellgren 1984; Dwek 1986; Draine & Li 2001a).

From the mid-to-near IR however, spectroscopic observations enabled and required the simple-two populations model of larger and smaller dust (e.g. Mathis et al. (1977)), to be expanded. “Unidentified IR bands” from 3 to $11 \mu\text{m}$ (hereafter, UIR bands), demonstrate another divergence from the canonical dust emission story. The UIR bands were first reported at 8 to $13 \mu\text{m}$ in planetary nebulae and Hii regions by Gillett et al. (1973, 1975) in ground-based observations. Observations by Merrill et al. (1975) noted another unexplained feature at $3.27 \mu\text{m}$, noting: “there are [...] similarities in the 8-13 μm spectra of NGC 253, NGC 7027, and BD +303639 Gillett et al. (1975)”. Features at 6.2 and $7.7 \mu\text{m}$ were reported by Russell et al. (1977) using the first airplane-mounted IR telescope and predecessor to SOFIA, the Kuiper Airborne Observatory. Sellgren et al. (1983) reported features at 3.3 and $3.4 \mu\text{m}$ being detected in reflection nebulae.

From this point, the UIR bands become much less of property of select objects in targeted observations, are seen observed throughout the Milky Way. Balloon-based observation by Giard et al. (1994)

confirmed that the $3.3 \mu\text{m}$ feature pervades throughout the Galactic plane. The first-ever airborne IR observatory, Kuiper Several years later, space-based spectroscopy with the Infrared Telescope in Space (IRTS)(Murakami et al. 1996) and Infrared Space Observatory (ISO)(Kessler et al. 1996) enabled confirmation by Onaka et al. (1996) and Mattila et al. (1996) that the mid-infrared UIR features are not limited to selection objects, but are present even in the diffuse galactic ISM by. Dwek et al. (1997) even reported that photometric excess in the COBE/DIRBE $12 \mu\text{m}$ band may be caused by the UIR bands, in and suggested they may be from these UIR features have come to be explained via polycyclic aromatic hydrocarbons (PAHs), a possibility which had been considered earlier by Al-lamandola et al. (1985); Puget et al. (1985). PAHs are a class of molecules composed primarily of fused carbon rings such as corannulene. PAHs and/or similar amalgams containing aromatic structures (e.g. quenched carbonaceous composites (QCCs), Sakata et al. (1984)) have been incorporated into dust mixture SED models over the last two decades (Draine & Li 2001b, 2007a; Hony et al. 2001; Compiègne et al. 2011; Galliano et al. 2011; Jones et al. 2013, 2017).

Moving in the opposite direction, into the Rayleigh-Jeans regime of thermal dust emission, multi-wavelength observations have opened up a new discipline: the disentanglement of interstellar dust emission from non-dust emission components. Most notably, separating fluctuations in the cosmic microwave background (CMB) from the microwave extent of thermal dust emission. Those studying the Milky Way itself, from the far IR into microwave and radio frequencies, are now collaborating closely with those interested in the precise nature of the CMB.

1.3 Microwave foregrounds

Much of the motivation between recent galactic microwave emission research has little to do with galactic ISM astronomy itself. Rather, our galaxy presents an inconvenience to observational cosmology in that it 'contaminates' observations of the CMB. The average SED of the CMB is simple enough to model, with a 2.755 K blackbody function. This temperature however means that the peak occurs between several microwave foreground components, from interstellar dust and gas, as displayed in Fig. 1.1. The difficulty of decomposing the microwave sky into galactic ISM, extragalactic, and CMB components has brought the detailed decomposition of the microwaveradio regime of ISM to the forefront of Planck Collaboration paper titles (Planck Collaboration et al. 2011a, 2014a, 2016a). Without extragalactic research, there would be no need for the word "foreground" in describ-

293 ing galactic microwave emission.

294 The ISM has intruded into cosmological studies perhaps most prominently with the first claimed
295 detection of B-mode polarization (Hanson et al. 2013; BICEP2 Collaboration et al. 2014; Flauger et al.
296 2014), and multiple response papers. The main consensus being that the validation of CMB-related
297 claims require a careful estimate of the contribution, in intensity and polarization, from interstellar
298 dust and the subsequent counterclaim that this detection arose from galactic dust(Planck Collabora-
299 tion et al. 2017; Sheehy & Slosar 2017). More recently AMI Consortium et al. (2012) had noted a
300 peculiar SunyaevZeldovich effect based galaxy cluster detection, AMI-CL J0300+2613. Perrott et al.
301 (2018) have since proposed that this may in fact arise from high galactic latitude dust via “anomalous
302 microwave emission” (AME).

303 1.3.1 Anomalous Microwave Emission

304 In our efforts to decompose and understand galactic microwave emission itself, there remains a con-
305 stant antagonist. Galactic foregrounds had been broken down into 3 dominant components: free-free
306 emission from ionized regions, synchrotron emission generated by electrons relativistically by the
307 Milky Way’s magnetic field, and the microwave extent of thermal dust emission (Bennett et al. 2003a;
308 Leach et al. 2008; Planck Collaboration et al. 2014c). Deviations from this understanding began to
309 appear in the early 1990s, with efforts by Kogut et al. (1996); Leitch et al. (1997) to carefully inves-
310 tigate the CMB. They had found a component of the microwave sky which implied unlikely spectral
311 indices for free-free or synchrotron emission. AME generally takes the form of an ’excess’ contin-
312 num emission source, having a peak somewhere between 10 to 40 GHz (see Fig. 1.1). This excess
313 defies predictions for known microwave emission mechanisms. AME still lacks a concrete physical
314 explanation. Also, the term itself can be a bit confusing, as the word “anomalous” tends to imply
315 localized outlier. The AME is shown to be more than an isolated anomaly, but an added component
316 of microwave emission appearing throughout the galaxy (de Oliveira-Costa et al. 1997; Bennett et al.
317 2003a; Dickinson et al. 2013). Fig 1.2 shows two prominent AME regions, ρ Ophiuchus and the Per-
318 sues Molecular Cloud investigated by Tibbs et al. (2011); Planck Collaboration et al. (2011b), as they
319 appear in AKARI/IRC $9\mu\text{m}$ all-sky map (Ishihara et al. 2010). In this section we will explain that
320 while there is indeed much mystery as to the exact mechanism(s) producing the AME, what causes its
321 spectral variations, and what might be its physical carrier(s) - it is by now, perhaps less than anom-
322 lous. Following subsections will discuss the history of AME and the produced physical explanations,

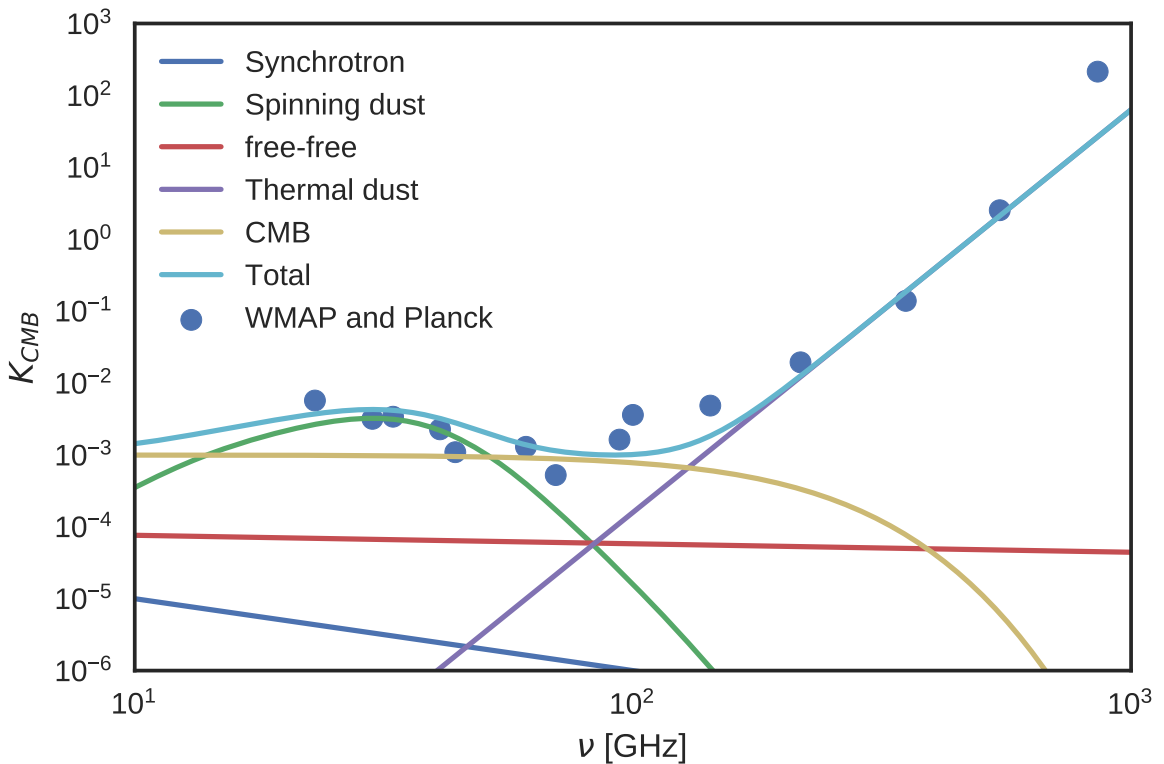


Figure 1.1: An example of a potential makueup of microwave emission components. Photometry points are extracted from the Planck and WMAP all-sky maps (Planck Collaboration et al. 2014b), for a part of the region well-known for prominent AME, ρ Ophiuchus (Planck Collaboration et al. 2011b). The AME curve is produced from a warm neutral medium spinning dust template (Ali-Haïmoud et al. 2009), with a frequency-shift applied to approximately fit the microwave data s in Planck Collaboration et al. (2016b)

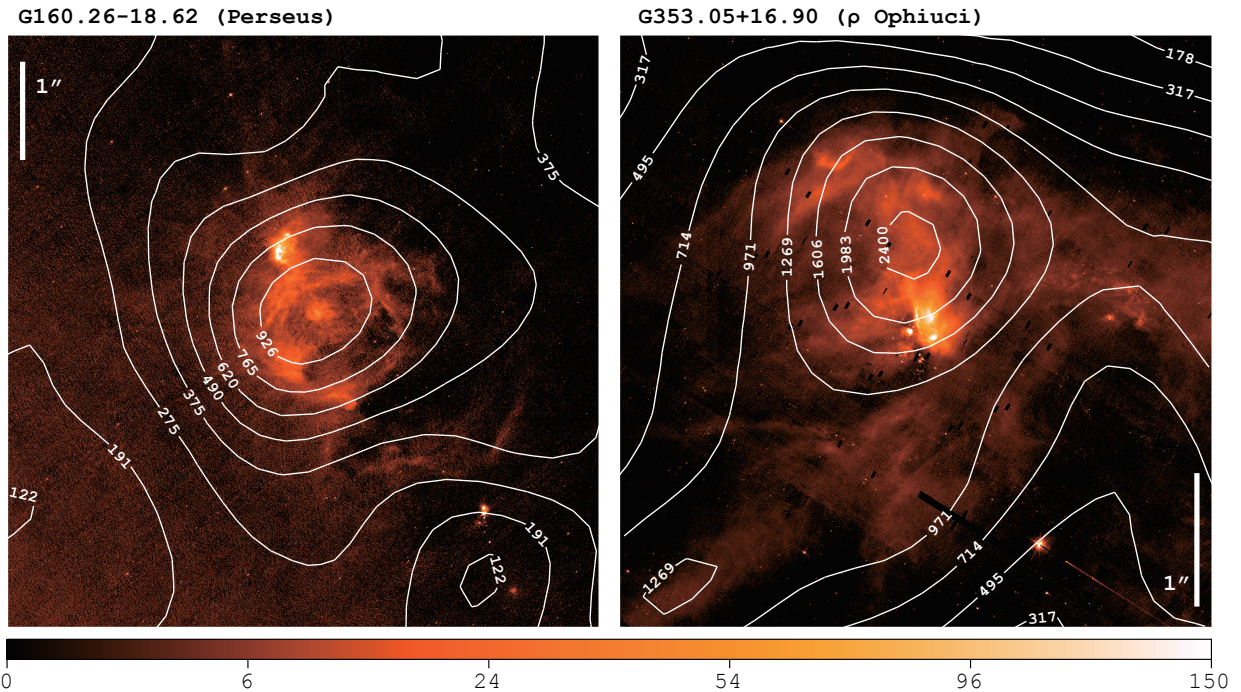


Figure 1.2: Two AME prominent regions investigated by Planck Collaboration et al. (2011b); Tibbs et al. (2011), ρ Ophiuchus and Perseus, as they appear in the PAH-feature-tracing AKARI/IRC $9\mu\text{m}$ all-sky data at native resolution (Ishihara et al. 2010). White contours show AME at 1-degree resolution, extracted from the map by Planck Collaboration et al. (2016b). The IRC data shown here is of a much finer resolution than the AME data, at around $10''$, demonstrating the critical gap in resolvability of all-sky AME-tracing data itself vs. the IR dust tracers we hope to compare it to.

323 as well comparisons between the AME and infrared emission from interstellar dust.

324 **Correlation with dust**

325 Since its first detection in early microwave observations, AME has been found to be a widespread
 326 feature of the microwave Milky Way (see the review Dickinson et al. (2013), and an updated state-
 327 of-play of AME research by Dickinson et al. (in prep). Kogut et al. (1996); de Oliveira-Costa et al.
 328 (1997) showed that the AME correlates very well with infrared emission from dust, via COBE/DIRBE
 329 and IRAS far-IR maps. Finkbeiner et al. (2002) reported the first detection of a “rising spectrum
 330 source at 8 to 10 GHz” in an observation targeting galactic ISM cloud. de Oliveira-Costa et al.
 331 (2002) further argued that this emission is in fact “ubiquitous”. The exact mechanism and carrier/s
 332 remain mysterious however. More recent works, employing observations by the Wilkinson Micrwave
 333 Anisotropy Probe (WMAP), Spitzer Space Telescope, the latest IR to microwave all-sky maps by
 334 Planck, and various ground based radio observations have strongly confirmed a relationship between
 335 interstellar dust emission and AME (Ysard & Verstraete 2010; Tibbs et al. 2011; Hensley et al. 2016).
 336 Exactly which physical mechanisms produces the AME however is still an open question, even if we
 337 assume a dusty AME origin. We equally puzzled as to the chemical composition and morphology of
 338 the carrier(s). We also lack an all-sky constraint on the emissivity of the AME spectrum at frequencies
 339 short of the WMAP cut-off, around 23 GHz. The typical peak frequency of AME, in those cases where
 340 it is constrained, does give us a clue.

341 **1.3.2 Proposed explanations**

342 From the observed spatial correlation between AME and dust emerged two prevailing hypotheses:
 343 1) Electric dipole emission by spinning small dust grains, a mechanism proposed in Erickson
 344 (1957) and Hoyle & Wickramasinghe (1970), with further discussion in Ferrara & Dettmar (1994).
 345 Draine & Lazarian (1998b) give the earliest thorough theoretical prediction of a spinning dust spec-
 346 trum. A decade later Ali-Haïmoud et al. (2009) contributed substantial updates, expanded modeling
 347 of grain excitation mechanisms and adoption of an updated grain size distribution by Weingartner
 348 & Draine (2001). Ysard & Verstraete (2010) introduced the first model of a spinning dust spectrum
 349 based on rotational emission from polycyclic aromatic hydrocarbons (PAHs), which are implicated
 350 due to their size. Draine & Lazarian (1998b), gives the expected rotational frequency of spinning dust

351 oscillators ω , as follows:

$$\frac{\omega_T}{2\pi} = \langle \nu^2 \rangle^{1/2} \approx 5.60 \times 10^9 a_{-7}^{-5/2} \xi^{-1/2} T_2^{1/2} \text{ Hz}, \quad (1.3.1)$$

352 where T is the gas temperature, a is the grain size, and ξ represents the deviation from a spherical
 353 moment of inertia. For example, we can take a typical peak frequency of the AME of 20 GHz, a gas
 354 temperature of 100 K, roughly spherical grains, and a dipole moment on the order of 1 debye, and
 355 get:

$$\frac{\omega_T}{2\pi} = 20 \text{ GHz} \left(\frac{T}{100 \text{ K}} \right)^{1/2} \left(\frac{\rho}{3 \text{ g cm}^{-3}} \right)^{-1/2} \left(\frac{a}{5 \text{ \AA}} \right)^{-5/2} \quad (1.3.2)$$

356 implying an oscillator size of approximately 1 nm. Thus PAHs, as considered by Ysard & Verstraete
 357 (2010), are a primary candidate spinning dust carrier, due to their expected size range.

358 2) Magnetic dipole emission, caused by thermal fluctuations in grains with magnetic inclusions,
 359 proposed by Draine & Lazarian (1999). More recently, modeled spectra for potential candidate carri-
 360 ers have appeared in the literature: PAHs, grains with magnetic inclusions (Draine & Hensley 2013;
 361 Ali-Haïmoud 2014; Hoang et al. 2016).

362 A third, but not widely accepted, possible explanation for AME is discussed in Jones (2009).
 363 They have suggested that the emissivity of dust, in the spectral range related to AME, could contain
 364 features caused by low temperature solid-state structural transitions.

365 Spinning dust

366 Spinning dust need not be the only emission mechanism, a convention as arisen in AME observational
 367 works. The photometric signature of the AME is frequently interpreted via spinning dust parameters
 368 (Ysard et al. 2011; Ali-Haimoud 2010). Archival all-sky AME data products exclusively assume
 369 a spinning dust SED templates. Both WMAP and Planck used a base template with 30 GHz peak
 370 frequency, and an assumed cold neutral medium environment. Using the “spdust” spinning dust SED
 371 model code to fit excess microwave foreground emission has become analogous fitting a modified
 372 blackbody function to the far IR.

373 We explore the case that the AME signature arises from spinning dust emission. If the AME
 374 is carried by spinning dust, the carrier should be small enough that it can be rotationally excited to
 375 frequencies in the range of 10-40 GHz, and must have a permanent electric dipole. Within contem-
 376 porary dust SED models, only the polycyclic aromatic hydrocarbon family of molecules (PAHs), or

377 nanoscale amorphous carbon dust fit these criteria. Those PAHs which have a permanent electric
 378 dipole (i.e. coranulene, but not symmetric molecules like coronene), can emit rotationally. How-
 379 ever the carrier need not be carbon-based. Indeed, Hensley & Draine (2017) claim that AME can be
 380 explained without carbonaceous carriers, using only spinning nanosilicates.

381 Spinning PAHs?

382 Assuming the rotational emission model of Draine & Lazarian (1998b), the AME signature (consis-
 383 tent with peaked, continuum emission having a peak between 15 and 50 GHz) implies very small
 384 oscillators (~ 1 s nm).

385 In any case, the PAH class of molecules are the only spinning dust candidate so far which show
 386 both:

- 387 1) Evidence of abundance in the ISM at IR wavelengths, and
- 388 2) A predicted range of dipole moments (on order of 1 debye), to produce the observed AME signature
- 389 (Draine & Lazarian 1998b; Lovas et al. 2005; Thorwirth et al. 2007).

390 However, it should be noted that although nanosilicates have not yet been detected in the ISM,
 391 Hensley & Draine (2017) propose that an upper bound on the abundance of nanosilicates by Li &
 392 Draine (2001) (based on IRTS observations by Onaka et al. (1996)), allow such small spinning grains
 393 to be composed primarily of silicates.

394 While neither nanosilicates nor any particular species of PAHs have been conclusively identified in
 395 the ISM, there is far more empirical evidence for PAH-like dust than for nanosilicates. Mid-infrared
 396 features associated with PAH-like aromatic materials have been observed. In fact, “the PAH features”
 397 are ubiquitous in the ISM (Giard et al. 1994; Onaka et al. 1996; Onaka 2000), such that the carriers
 398 must be abundant. Andrews et al. (2015) strongly argue for the existence of a dominant “grandPAH”
 399 class, containing 20 to 30 PAH species.

400 1.3.3 Excitation factors

401 In the spinning dust model, there are several possible excitation factors for spinning dust. For the
 402 grains to have rotational velocities high enough to create the observed AME, they must be subject
 403 to strong excitation mechanisms. The dominant factors that would be giving grains their spin, are
 404 broken down by Draine (2011) into basically two categories: 1) Collisional excitation. 2) Radiative
 405 excitation, the sum of which could lead to sufficient rotational velocities for sufficiently small grains.

406 However the extent of excitation will depend on environmental conditions, i.e. there will be more
 407 frequent encounters with ions and atoms in denser regions (so long as the density is not high enough
 408 to coagulate the small grains), and more excitation due to photon emission with increasing ISRF
 409 strength (Ali-Haïmoud et al. 2009; Ali-Haïmoud 2014). One of the strongest potential excitation
 410 mechanims listed in Draine (2011) is that of negatively charged grains interacting with ions. Thus
 411 not only must we consider environmental factors, grain composition and size, but also the ionization
 412 state of the carriers. (For example, ionized vs. neutral PAHs.) The dependence of the observed AME
 413 on ISM density is modeled by Ali-Haimoud (2010).

414 1.3.4 AME vs. IR in the literature

415 The overall pattern among large-scale studies seems to show that all of the dust-tracing photometric
 416 bands correlate with the AME (and each other) to first-order. On an all-sky, pixel-by-pixel basis,
 417 at 1° angular resolution, Ysard et al. (2010) find that $12\ \mu\text{m}$ emission, via IRAS, correlates slightly
 418 more strongly with AME (via WMAP) than with $100\ \mu\text{m}$ emission. They also find that scaling the IR
 419 intensity by the interstellar radiation field strength (given as G_0 , a measure of ISRF relative to that of
 420 the solar neighborhood) improves both correlations. They interpret this finding as evidence that AME
 421 is related to dust, and more closely related to the small stochastically emitting dust — predominantly
 422 PAHs — that is traced by $12\ \mu\text{m}$ emission. The improvement of the correlations after scaling by G_0
 423 is expected, as long as the $12\ \mu\text{m}$ or $9\ \mu\text{m}$ photometric bands are by stochastic emisson from PAHs,
 424 in other words:

$$I_{12\ \mu\text{m}} \propto G_0 N_{PAH}, \quad (1.3.3)$$

425 where N_{PAH} is the column density of emitting PAHs (Onaka 2000). Thus it implies that $I_{12\ \mu\text{m}}/G_0$
 426 is giving us a measure of the column density of spinning dust.

427 In a similar work however Hensley et al. (2016) report a lack of support for the spinning PAH
 428 hypothesis. Finding that fluctuations in the ratio of PAH-dominated $12\ \mu\text{m}$ emission (via WISE) to
 429 dust radiance, R , (via Planck) do not correlate with the ratio of AME intensity to R , they conclude
 430 that the AME is not likely to come from PAHs. In terms of emission intensity however, their findings
 431 are consistent with Ysard et al. (2010) in that $I_{12\ \mu\text{m}}$ correlates well with I_{AME} . Thus there remains
 432 an open question as to what the actual carrier of the AME is.

433 The story is no more clear when looking at the average properties of individual regions. Planck
 434 Collaboration et al. (2014d) find that among 22 high-confidence “AME regions” (galactic clouds

435 such as the ρ Ophiuchus cloud and the Perseus molecular cloud complex) AME vs. $12\ \mu\text{m}$ shows a
 436 marginally weaker correlation than AME vs. $100\ \mu\text{m}$ (via IRAS). Tibbs et al. (2011) examined the
 437 AME-prominent Perseus Molecular Cloud complex, finding that while there is no clear evidence of a
 438 PAH-AME correlation, they do find a slight correlation between AME and G_0 .

439 **1.4 Scope of this Dissertation**

440 We attempt to add to the understanding of AME and the possibility of spinning dust emission. With
 441 ample multiwavelength data now available, and a new PAH-focused all-sky survey in preparation by
 442 AKARI, we further test the PAH hypothesis, and assess how the IR to AME correlation changes as a
 443 function of wavelength.

444 **1.4.1 An application of all-sky archival data**

445 This is an astrophysical data archive based work. The primary goal is to highlight a particular ap-
 446 plication of multiwavelength (mid-IR to radio), cross-archive all-sky data analysis. We describe the
 447 interrelatedness between mid to far IR dust emission and possible microwave emission from dust.
 448 This is accomplished through an investigation of photometric all sky maps mainly from AKARI,
 449 IRAS, and Planck.

450 **1.4.2 Testing the spinning PAH hypothesis**

451 For the present work, we consider the spinning PAH hypothesis to have the highest degree of testa-
 452 bility, due to the well-established presence of aromatic emisison features in the ISM. We do not argue
 453 against the physical plausibility of nanosilicates to produce the AME. Indeed, there is no argument to
 454 date that these potential physicalities are mutually exclusive, as long as both potential carriers are suf-
 455 ficiently abundant. Nor does spinning dust emission theoretically exclude magnetic dipole emission
 456 or microwave thermal dust emissivity fluctuations.

457 **1.4.3 Limitations**

458 We do not explore the modeling of microwave dust emission itself, rather we refer to estimates of
 459 spinning dust emisison provided in the literature (Planck Collaboration et al. 2014c; Bennett et al.
 460 2003a) in the form of archival data and parameter maps. We consider this problem first on an all-sky

461 basis, not focusing on any pre-selected object of the sky — in order to assess if there any general
462 pattern between the IR and the AME, beyond the AME-dust correlation already described above. We
463 then focus on a region highlighted by the Planck Collaboration as being especially worthy of further
464 investigation (Planck Collaboration et al. 2016b), and has a resolvable topology even at 1-degree
465 resolution. Essentially all of the analyses and conclusions presented in this work apply to an angular
466 scale of approximately 1-degree, and only for the given component separation methods (Solar system,
467 galactic, extragalactic) used by each of the data providers.

468 **1.4.4 Code availability**

469 This dissertation is accompanied by a github repository.¹ Virtually all of the analyses code are avail-
470 able in that repository, in the form of Jupyter notebooks (along with the figures and the code used to
471 generate them.) The dust SED fitting code is not part of that repository, but is described in Galliano
472 et al. (in prep.)

¹Available at: <https://github.com/aaroncnb/CosmicDust>.

⁴⁷³ **Chapter 2**

⁴⁷⁴ **Data Sources**

⁴⁷⁵ **2.1 A collection of skies**

⁴⁷⁶ This work relies completely on all-sky surveys. All of the maps utilized are photometric-band infrared
⁴⁷⁷ maps, except for the AME data, which is an all-sky component separation analysis product, from the
⁴⁷⁸ Planck Collaboration's efforts to separate galactic foregrounds from the CMB. Table 2.1 summarizes
the observational data used in this thesis. In total, we employ all-sky maps from 12 photometric

Table 2.1: Observational data sources used in this article

Instrument	Central Wavelength	FWHM	Cali	Reference
AKARI/IRC	9 μm	~10"	<10%	¹
AKARI/IRC	18 μm	~10"	<10%	"
AKARI/FIS	65 μm	63"	<10%	²
AKARI/FIS	90 μm	78"	<10%	"
AKARI/FIS	140 μm	88"	<10%	"
AKARI/FIS	160 μm	88"	<10%	"
IRAS/IRIS	12 μm	4.0'	<5.1%	³
IRAS/IRIS	25 μm	4.0'	<15.1%	"
IRAS/IRIS	60 μm	4.2'	<10.4%	"
IRAS/IRIS	100 μm	4.5'	<13.5%	"
Planck/HFI	345 μm	4.7'		⁴
Planck/HFI	550 μm	4.3'		"

⁴⁷⁹

⁴⁸⁰ bands, spanning the wavelength range of 6.9 μm to 550 μm as showin in Fig. 2.1 The following
⁴⁸¹ sections give the details of the observational data from each instrument as well as of the parameter

¹Ishihara et al. (2010)

²Doi et al. (2015); Takita et al. (2015)

³Miville-Deschénes & Lagache (2005)

⁴Planck Collaboration et al. (2014b)

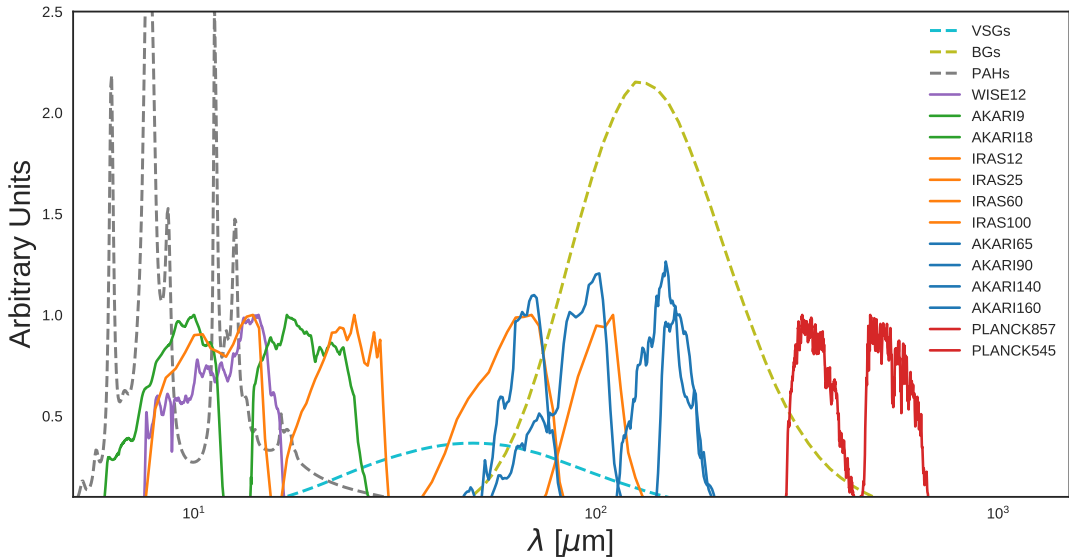


Figure 2.1: Relative spectral response curves of the bands used in this study. Expected dust emission components, assuming the dust SED model by (Compiègne et al. 2011) are also shown. The components are summarized as emission from big grains (BGs, dashed yellow line), emission from very small grains (VSGs, dashed blue line), and emission from PAHs (dashed grey line).

maps provided in Planck Collaboration et al. (2016b).⁵ From this point in the thesis, we will mostly use abbreviations to refer to the different bands, as follows: 'A' indicates AKARI; 'D', DIRBE; 'I', IRAS, and 'P' Planck. The number after each letter indicates the band central nominal wavelength in microns (or frequency in GHz, in the case of the Planck bands.)

2.2 AKARI

The AKARI infrared space telescope revealed an entire sky of infrared light, from the mid to far infrared, via two instruments (Murakami et al. 2007) the Infrared Camera (IRC)(Onaka et al. 2007) and the Far Infrared Surveyor (FIS) (Kawada et al. 2007b). In this section we will discuss the all-sky surveys produced by these two instruments.

2.2.1 AKARI/Infrared Camera (IRC)

IRC provided us with both spectroscopic and photometric data from the near to mid-infrared. In this work, we utilize the all-sky maps centered at 9 and 18 μm , created during by the IRC's fast-scanning mode. We utilize the most recent version of the IRC data (Ishihara, et al., in prep.) This version has

⁵Planck bands are named according to their central frequency, not wavelength.

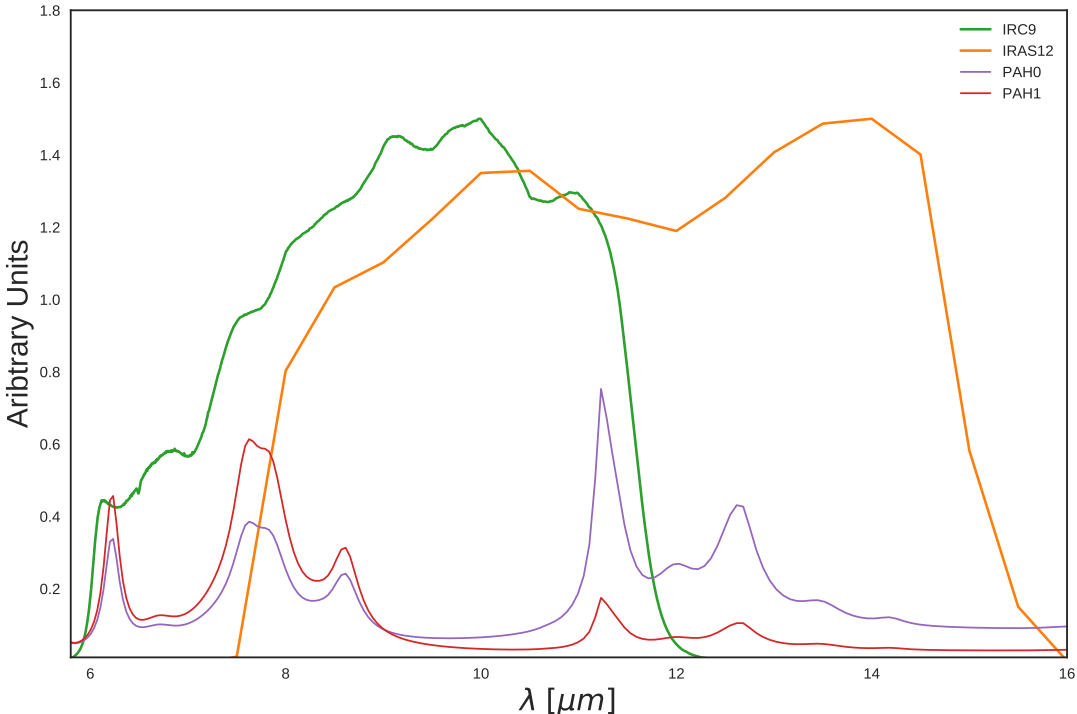


Figure 2.2: The I12 (orange) and A9 (green) filters coverage of modeled ionized (PAH1, red) and neutral (PAH0, purple) components of PAH features by Compiègne et al. (2011). The difference in the PAH feature coverage mainly comes from the $6.2 \mu\text{m}$ and $7.7 \mu\text{m}$ feature.

495 had an updated model of the Zodiacial light, fitted and subtracted. The details of the improved Zodi-
 496 model, which offers an improvement over that used for the IRAS all-sky maps, are given in Kondo
 497 et al. (2016).

498 PAH feature coverage

499 The A9 all-sky map demonstrates the abundance of the PAH bands carrier in the Milky Way (Ishihara
 500 et al. 2010). Figure 2.2 shows the coverage of the PAH features (from both ionized and neutral PAH
 501 components), as they are theoretically determined in Compiègne et al. (2011). The A9 band uniquely
 502 covers major ionized PAH features at $6.2 \mu\text{m}$ and $7.7 \mu\text{m}$; as well as neutral PAH features at $8.6 \mu\text{m}$ and
 503 $11.2 \mu\text{m}$ across the entire sky (Onaka et al. 2007). The I12 band covers the $11.2 \mu\text{m}$ and $8.6 \mu\text{m}$ features,
 504 and the similarly-shaped W12 band covers primarily the $11.2 \mu\text{m}$ feature but do not cover the $7.7 \mu\text{m}$
 505 completely. According to the distribution of PAH features across the response filters in Fig. 2.2, and
 506 referring back to the various dust components in Fig. 2.1 it is also expected that the A9 band is most
 507 dominated by PAH emission even with increasing G_0 . This may seem counter-intuitive, since, as
 508 described in Ch. 1, the PAH spectral shape does not show a temperature variation. However as T

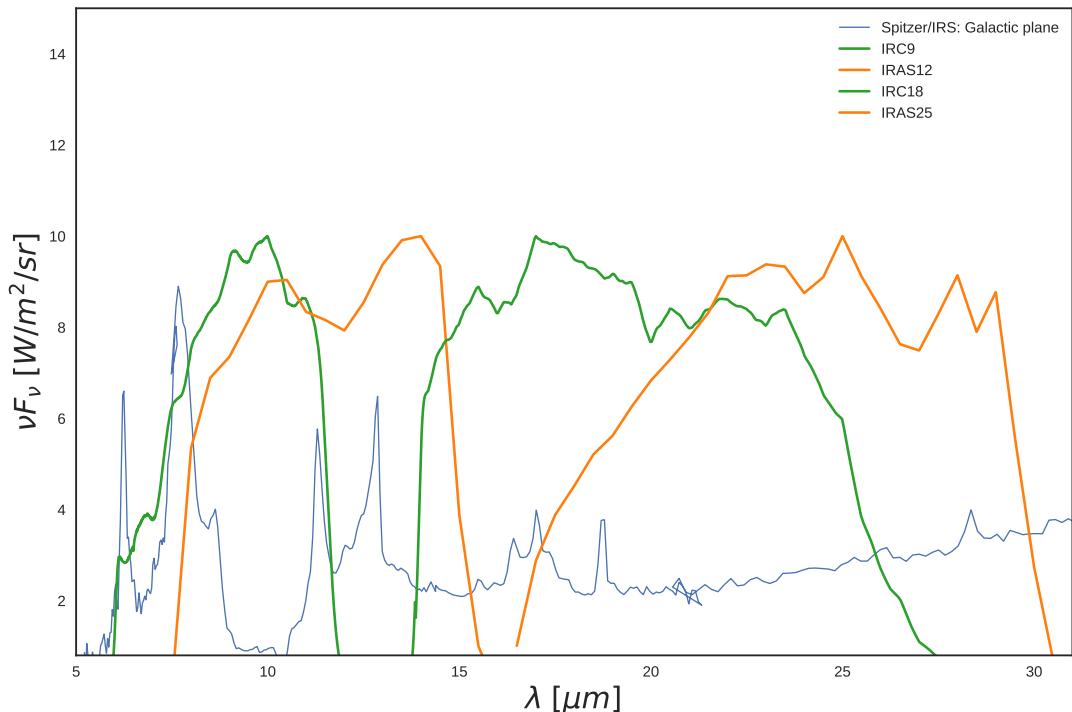


Figure 2.3: Coverage of MIR wavelengths by the filters used in this work. An Spitzer/IRS spectrum (see AOT4119040) of the galactic plane (thin blue line) demonstrates how IRC and IRAS photometric bands trace these features on an all-sky basis (Ishihara et al. 2007). Strong PAH features overlap with the A9 and I12, while the A18 and I25 micron bands only trace much weaker features.

increases, the MIR extent of thermal dust emission and emission from VSGs encroach on I12 and WI2 sooner than A9, diluting emission from PAHs. In some ionized regions, I12 may also include non-significant contributions from the NeII line at $12.8\text{ }\mu\text{m}$. Figure 2.3 demonstrates an example observational galactic cirrus spectrum in the MIR, from Spitzer Infrared Spectrograph (IRS) (Werner et al. 2004) data from), along with filters for all of the MIR bands used in this study. It indicates that the other MIR bands, A18 and I25, do cover strong PAH features and are expected to be dominated rather by emission from very small grains (VSGs), as was indicated in Fig. 2.1.

To help demonstrate how the relative contribution from PAHs will change for each band, for different ISRF strengths, Fig. ?? gives just such a calculation. These contributions remain relatively constant out to a G_0 of about 100, with the contribution from warm dust becoming a larger factor for the I12 and W12 bands. Thus, according to the DL01 template, A9 should have the highest contribution from PAHs out to extreme radiation fields. At least to the extent with which PAHs can endure harsh UV radiation, as PAHs are expected to be destroyed in some environments (Allain et al. 1996a,b; Pilleri et al. 2012; Pavlyuchenkov et al. 2013).

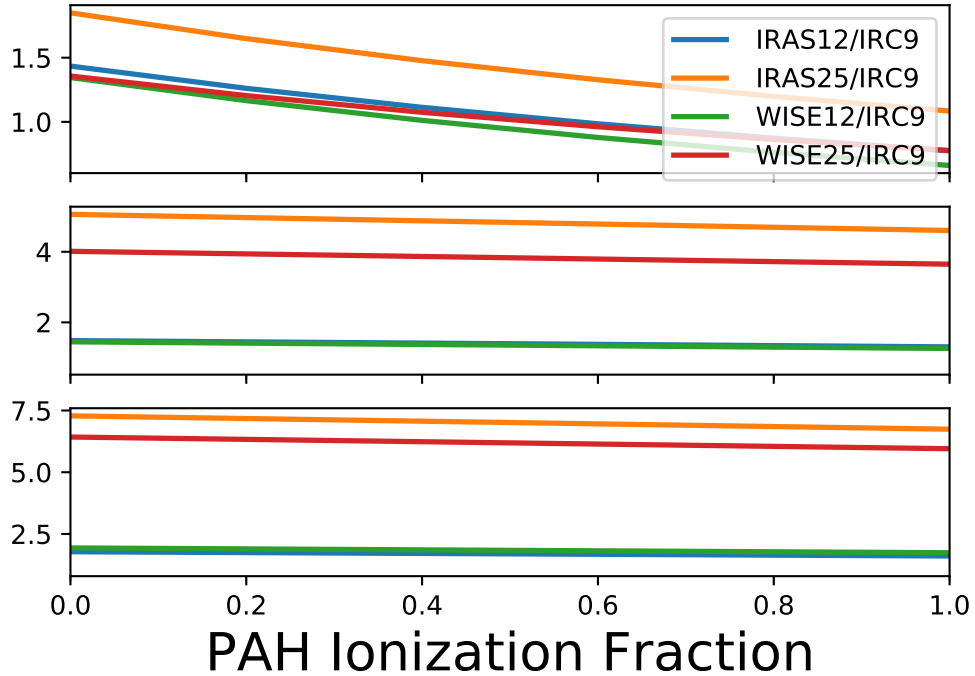


Figure 2.4: Ionization fraction of PAHs vs. band ratios of I12, I25, W12, W25 vs. A9, for three ISRF strengths: Top: $G_0 = 100$, Middle: $G_0 = 1000$, and Bottom: $G_0 = 10000$. These ratios are determined by assuming the SED template of Compiègne et al. (2011)

523 PAH ionization

524 Figure 2.2 indicates that expected emission from ionized PAHs will preferentially contribute to the A9
 525 band, even though both I12 and A9 cover ionized and neutral features. To estimate the extent to which
 526 the ionization fraction would effect the intensity ratio of these two bands, Fig. 2.4 gives the results of
 527 a calculation based on the Draine & Li (2001b) dust model, for various strengths of G_0 . demonstrates
 528 how the band ratios of the IRC μm band vs. the other MIR bands change with different modeled
 529 PAH ionization fractions (determined using the DustEM default model template, by Compiègne et al.
 530 (2011)). This band ratio can be determined, because the IRC9 filter is more sensitive to ionized PAH
 531 features, relative to IRAS12 or to WISE12.

532 IRC 9 μm shows a larger contribution from ionized PAHs and a conversely smaller contribution
 533 from neutral PAHs. Fig. 2.5 and Fig. 2.6 show the R(A9:I12) and R(A9:I25) ratio maps, demon-
 534 strating the relative variations in these MIR bands accross the sky- or at least the portions of the sky
 535 where S/N is sufficient. While from visual inspection the various MIR intensity all-sky maps appear
 536 to essentially trace the same stuctures of the galaxy, the ratio maps reveal that there are indeed dif-
 537 ferences to be explored. In regions where noise is dominant, ascertaining the ionization fraction will
 538 be quite difficult. This can be easily seen upon visual inspection of the ratio maps, in that there is

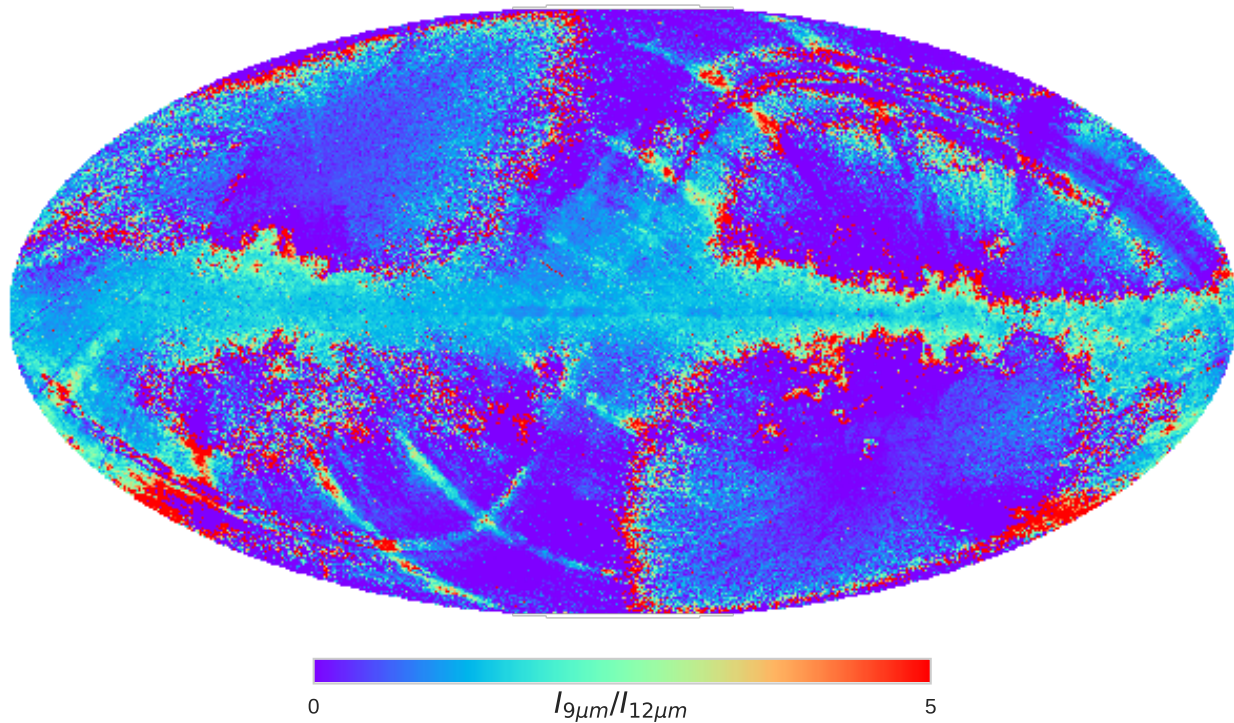


Figure 2.5: AKARI/IRC 9 μm to IRAS 12 μm intensity ratio.

539 a clear deliniation between brighter emission towards lower galactic latitudes, and the high latitude
 540 sky where the ratio shows very little discernible structure (except for the Zodi-residual patterns which
 541 differ between IRC and IRAS.) Thus even with the high latitude issues, there remains a large portion
 542 of the sky where a tracing of the ionization fraction may be feasible. This possibility is explored in
 543 Ch. 3, in looking at the PAH distribution within λ Orionis.

544 2.2.2 The AKARI Far Infrared Surveyor (FIS)

545 FIS gives us photometric data around the peak of the typical thermal dust SED. FIS was equipped
 546 with four wavebands: two narrow bands centered at 65 μm and at 160 μm , and two wide bands at
 547 90 μm and at 140 μm . An all-sky survey was carried out at each band (Kawada et al. 2007a), and the
 548 processed maps have been publicly released (Doi et al. 2015).

549 2.2.3 Planck Observatory High Frequency Instrument (HFI)

550 The HFI all-sky maps, spanning 100 to 857 GHz (Planck Collaboration et al. 2014b) help constrain
 551 the far IR dust emissivity. This study utilizes the 857 GHz (345 μm) and 545 GHz (550 μm) bands.

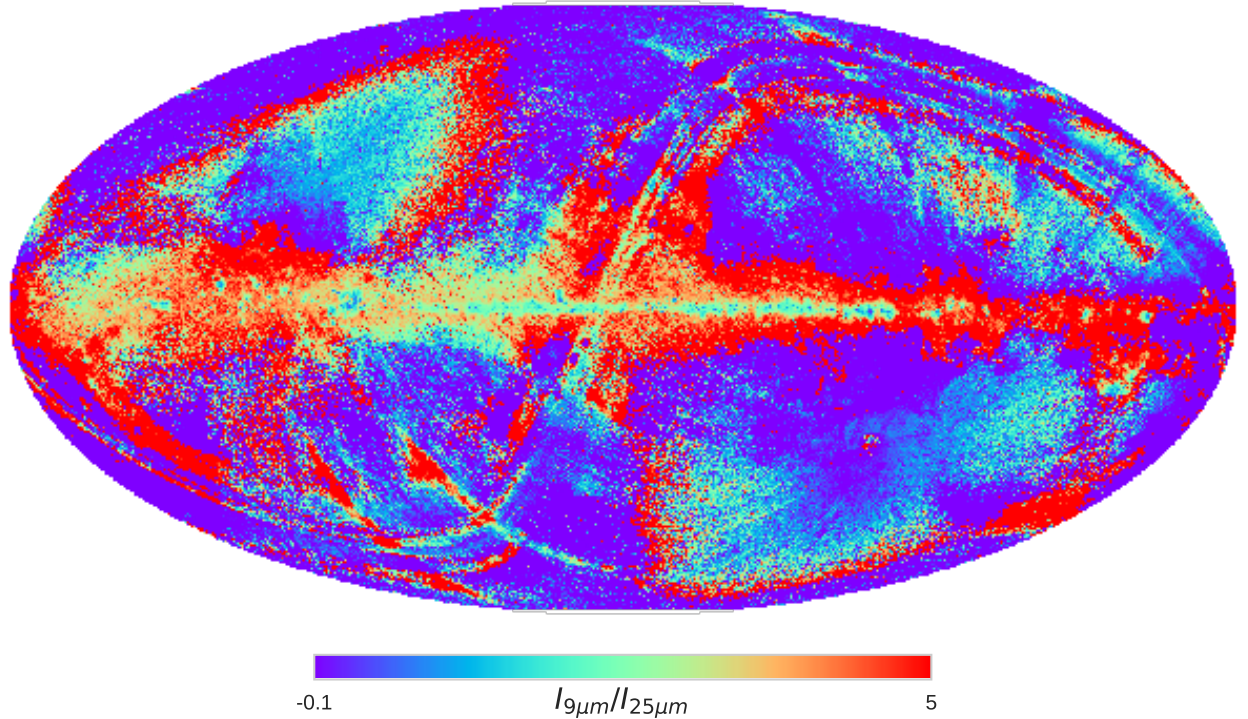


Figure 2.6: AKARI/IRC 9 μm to IRAS 25 μm intensity ratio.

552 2.3 Infrared Astronomical Satellite (IRAS)

553 Data from the IRAS (Neugebauer et al. 1984) all-sky surveys are used to supplement the similarly-
 554 centered AKARI photometric bands. The IRAS 12 μm band is similar to the IRC 9 μm band in terms
 555 of the sky coverage, central wavelength, and especially in that both surveys are heavily dominated by
 556 zodiacal light. We use the Improved Reprocessing of the IRAS Surveys (IRIS) (Miville-Deschénes
 557 & Lagache 2005), which have undergone a zodiacal-light removal. The Zodiacal light model, however
 558 differs between the two bands. The IRAS Zodi-subtraction is primarily based on the Kelsall et al.
 559 (1998) model. Although WISE provides higher resolution than IRAS, we do not utilize the WISE
 560 data because we found the WISE all-sky 12 μm product to essentially trace the Planck HFI 857 GHz
 561 map, at 1 degree angular resolution. Hensley et al. (2016) had noted that this scaling of the WISE
 562 map may artificially suppress actual PAH-related variations at low resolution. Moreover, since we are
 563 conducting our analysis at 1 degree resolution in order to match the AME data, the higher resolution
 564 offered by WISE is not a significant advantage.

565 2.4 Planck COMMANDER Parameter Maps

566 We utilize the COMMANDER-Ruler astrophysical component separation maps (Planck Collaboration et al. 2014c), from the Planck Collaboration’s Public Data Release 2 (hereafter, PR2)(Planck
567 Collaboration et al. 2016a). These contain estimates of known microwave foreground components
568 (free-free, synchrotron, thermal dust emission contributions to the Planck photometric bands. Fig. 2.7
569 demonstrates the correlatedness of these component maps, taken as provided in the PR2 archive.
570 Without considering noise levels or variations of scale, we see evidence these major components are
571 correlated with one another. In the case of free-free emission, von Hausegger & Liu (2015) found that
572 by taking S/N ratios into account, the correlation between COMMANDER free-free and AME com-
573 ponents turns negative. More generally they suggest that the intercorrelations between these products
574 varies with scale. We will first describe the ‘non-AME’ components, so as to not give any indication
575 that their estimation is trivial.

577 2.4.1 Synchrotron

578 While the Planck observations themselves do limit our resolution when assessing the AME - it is
579 the primary constraint on synchrotron emission, 408 MHz map by Haslam et al. (1982) that is the
580 major resolution limiting factor. While an impressive early effort to reveal the low-frequency sky,
581 (Haslam et al. 1982) is limited to an approximately 1 degree resolution. The map also contains many
582 artifacts. For the time being however, it is still the most synchrotron-dominated all-sky map available,
583 and for this reason PC15X included it in their COMMANDER component separation. Enhanced
584 synchrotron mapping efforts are currently in progress by the ‘The final synchrotron product produced
585 by COMMANDER (hereafter, PCSync) highly resembles the Haslam et al. (1982) map, however it
586 is also demonstrated PCSync does not fully capture the synchrotron signal. This can be visualized
587 by inspecting the PCAME:PCdust ratio map (see Fig. 2.12), which Hensley et al. (2016) describe as
588 containing synchrotron emission patterns at high latitudes.

589 2.4.2 Free-free emission

590 Unlike the PCSync component, the fitting of the Planck COMMANDER free-free component map
591 (hereafter, PCff) does not employ any free-free dominated emission map, even though an earlier
592 Planck AME paper (Planck Collaboration et al. 2014d) had employed the H- α map by Reynolds

	AMEvar	AMEfix	AMErad	AMEfreq	ff	Sync	$I_{dust}(545)$	T	B
AMEvar	1	0.81	1	-0.37	0.64	0.68	0.8	-0.52	0.39
AMEfix	0.81	1	0.83	-0.011	0.73	0.71	0.89	-0.59	0.42
AMErad	1	0.83	1	-0.32	0.66	0.7	0.83	-0.54	0.4
AMEfreq	-0.37	-0.011	-0.32	1	0.023	0.063	0.093	-0.051	0.042
ff	0.64	0.73	0.66	0.023	1	0.56	0.74	-0.51	0.44
Sync	0.68	0.71	0.7	0.063	0.56	1	0.74	-0.41	0.38
$I_{dust}(545)$	0.8	0.89	0.83	0.093	0.74	0.74	1	-0.69	0.38
T	-0.52	-0.59	-0.54	-0.051	-0.51	-0.41	-0.69	1	-0.38
B	0.39	0.42	0.4	0.042	0.44	0.38	0.38	-0.38	1

Figure 2.7: r_s cross correlation matrix of the PCCS maps: temperature T , emissivity index β , and amplitude at 545 GHz $I_{dust}(545)$ of thermal dust; intensity of free-free emission ff at ; intensity of synchrotron emisison at 4 MHz $Sync$; intensity of the AME var. freq. component AME at 22.8 GHz.

593 et al. (1998). Uncertainties in this map arise from uncertainties in the gas temperature, and the Gaunt
594 factor. This emission source is the dominant source of confusion with AME, especially for Hii regions
595 (Planck Collaboration et al. 2014d,c; Paladini et al. 2015).

596 **2.4.3 Thermal dust emission**

597 “Thermal dust emission” in the COMMANDER context refers to dust emission in the Rayleigh Jeans-
598 regime, as the COMMANDER fitting does not include photometric constraints on the thermal emis-
599 sion peak, or consider small grain emission on the Wiens side. This component essentially involves
600 the fitting of a modified blackbody curve (Eq. 1.2.1.) to the Planck Photometry. This approach
601 however results in an apparent anti-correlation between β and T (Fig. 2.7). Whether or not this anti-
602 correltion is genuine is still unsettled in the literature. In any case, we do not utilize the β and T , only
603 the dust intensity at 545 GHz (I_{dust}) parameter map.

604 **2.4.4 AME data**

605 The COMMANDER map release also provides an “AME component map”, which presumes that
606 AME originates from spinning dust. While acknowledging that such a decomposition lacks a strong
607 physical interpretation, Planck Collaboration et al. (2016b) break the AME into two components:
608 a spatially varying peak frequency component, and a spatially constant peak frequency component.
609 As seen in Fig. 2.8, virtually all of the fitted peak frequncies for AME_{var} are beyond the reach of
610 WMAP and Planck. Only the fitted global frequency, 33.5 GHz for the spatially constant component,
611 is covered. However they note that the combined components, per pixel, would have an average peak
612 at least within the WMAP coverage range. In general, AME_{var} is the dominant component, account-
613 ing for approximately 90% of the total AME intensity at a given frequency, indicated by the full-sky
614 histograms in Fig. 2.9. As they are provided in PR2, the intensities are in fact the fitted spinning
615 dust profiles for each pixel, evaluated at reference frequencies: 22.8 GHz for AME_{var} , 41 GHz for
616 AME_{fix} (for convenient comparison to the WMAP total intensity maps at those frequencies). Fig. 2.9
617 in fact indicates our own re-evaluation of the fitted spinning dust SEDs at their peak frequencies, as
618 the reference frequencies to not have any special physical relevance. This conversion does not have
619 a significant effect on the results in the chapters to follow, except in the case of some outlying pixels
620 with very low peak frequencies, easily seen in the map of the fitted frequencies in Fig. 2.10. However
621 on comparison to point source masks by Planck, we find that these outliers correspond to intensity

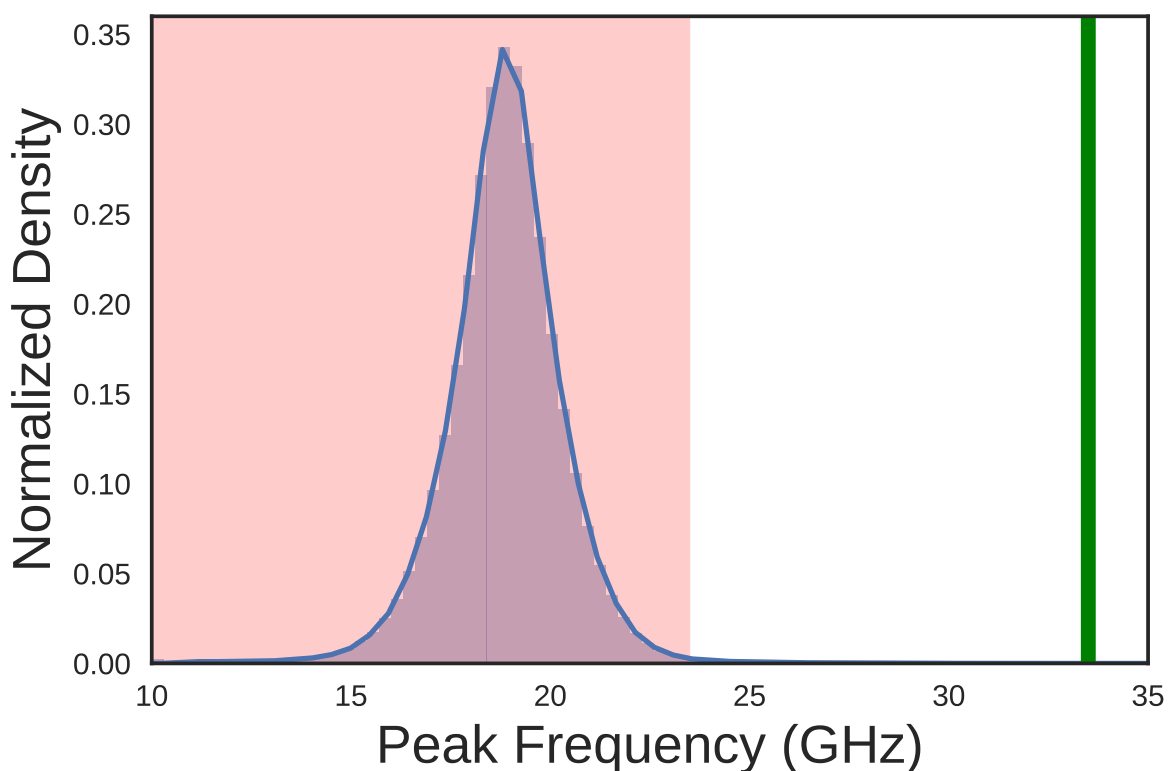


Figure 2.8: The peak frequencies of the varying component AME_{var} . The pink shaded region indicates frequencies not covered by either WMAP or Planck. The green line at 33.5 GHz indicates the peak frequency of AME_{fix} .

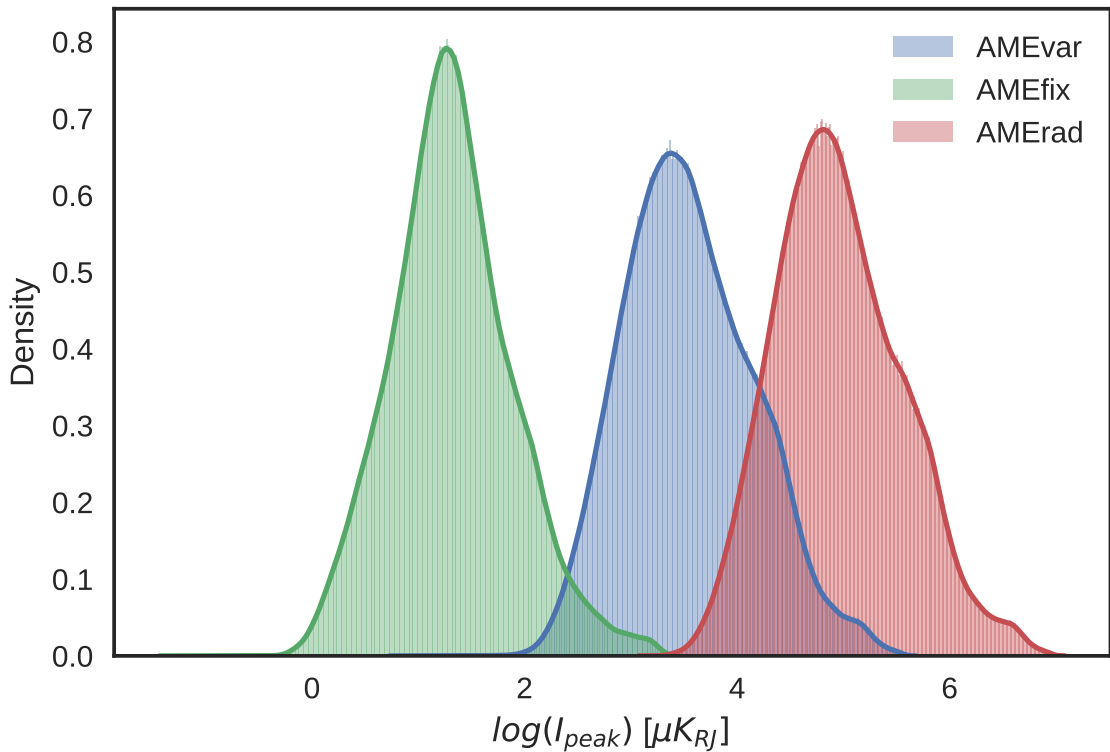


Figure 2.9: Histograms of the peak intensity AME maps calculated from the original COMMANDER-AME reference frequency maps. The dominant component, AME_{var} is indicated in blue, for all pixels in the map, with their spinning dust intensities evaluated their peak frequencies (see Fig. 2.8.) AME_{fix} gives the peak intensity of the spatially-constant frequency component, indicating it is essentially always the weaker component.

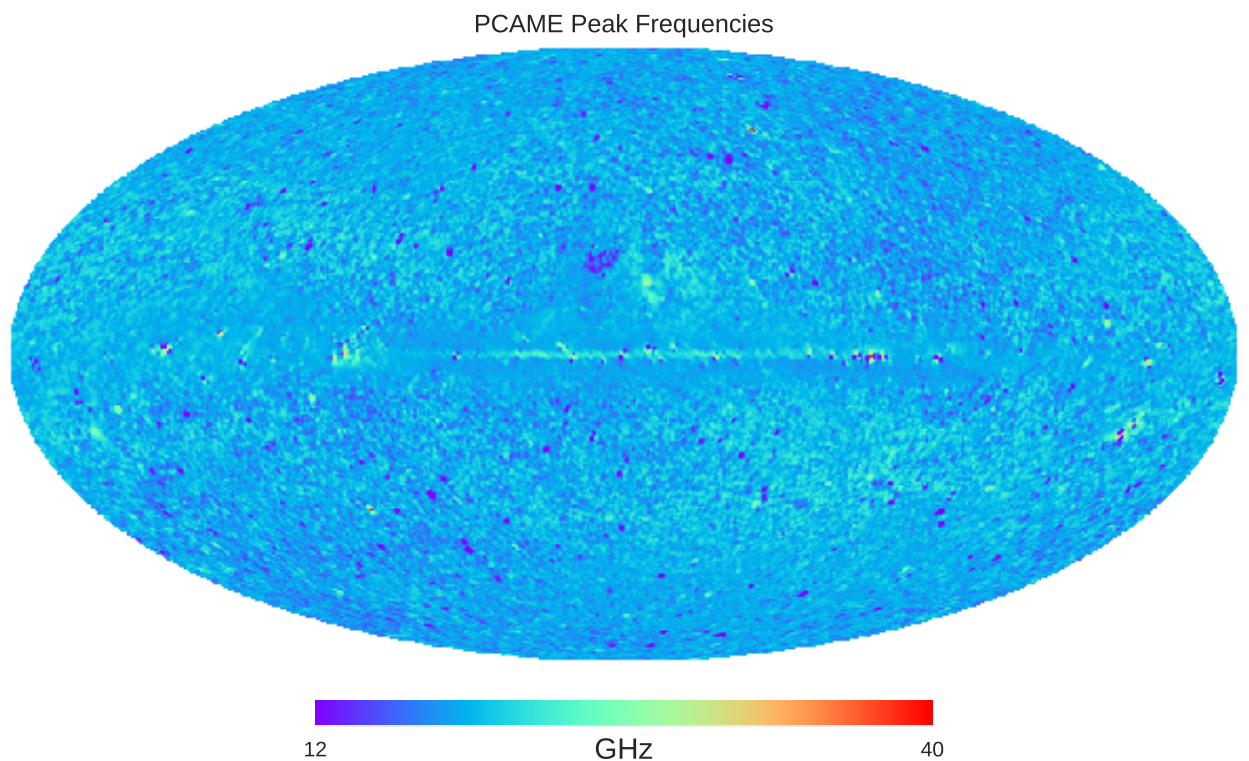


Figure 2.10: All-sky map of the peak frequencies of the varying component AME_{var} , corresponding to Fig. 2.8. Virtually all of the purple regions of the map correspond to pixels flagged for point sources in the LFI data. There are very few notable structures in the frequency map overall, other than the galactic plane itself, ρ Ophiuchus, and Perseus.

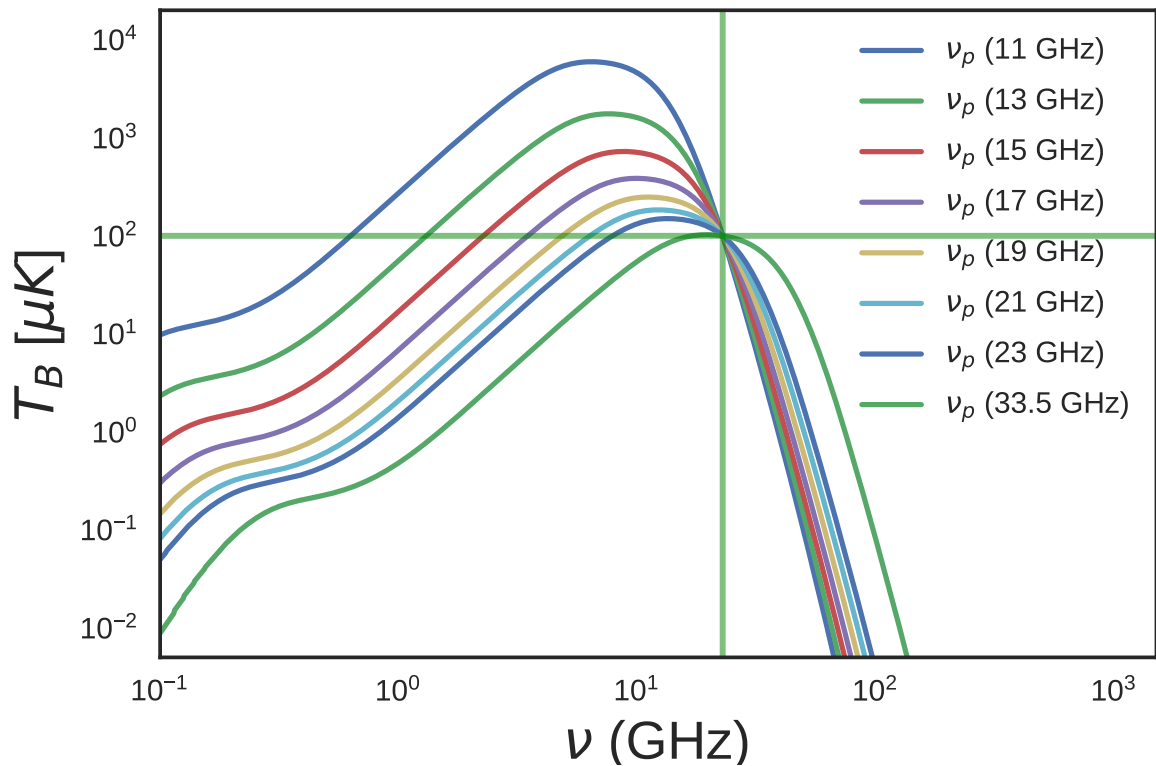


Figure 2.11: Spdust template spinning dust profiles fitted by PC15X when calculating AME_{var} . The reference frequency, 22.8 GHz is indicated by the vertical green line. Each template has the same AME_{var} amplitude of $100 \mu\text{K}$, indicated by the horizontal green line, plotted to highlight the potential deviation between AME_{var} and the actual peak intensity.

622 outliers in the LFI 30 GHz map. This is not readily apparent when viewing the AME_{var} , evaluated at
 623 22.8 GHz, as it is provided in Planck Collaboration et al. (2016b).

624 Spinning dust fitting

625 The actual spinning dust SED which is fitted to the Planck data by is indicated by Fig. 2.11, which
 626 we have reproduced from the original template provided in Ali-Haïmoud et al. (2009). PC15X fit
 627 the AME by applying a frequency shift and intensity shift parameter to this template. The physical
 628 parameters of the 'spdust' model itself are not directly varied in PC15X. In any case, the spinning dust
 629 model SED shape does not show significant variation from environment to environment (Ali-Haïmoud
 630 et al. 2009). Because of the phenomenological approach of the AME fitting method, the PC15X authors
 631 themselves suggest caution in deriving conclusions from comparisons with the COMMANDER AME
 632 map. However it is the most thorough all-sky component separation currently available, and has
 633 not been well analyzed relative to the wavelength range of IR all-sky maps produced. Improving
 634 on the COMMANDER AME map will likely require lower frequency constraints (in the red-shaded

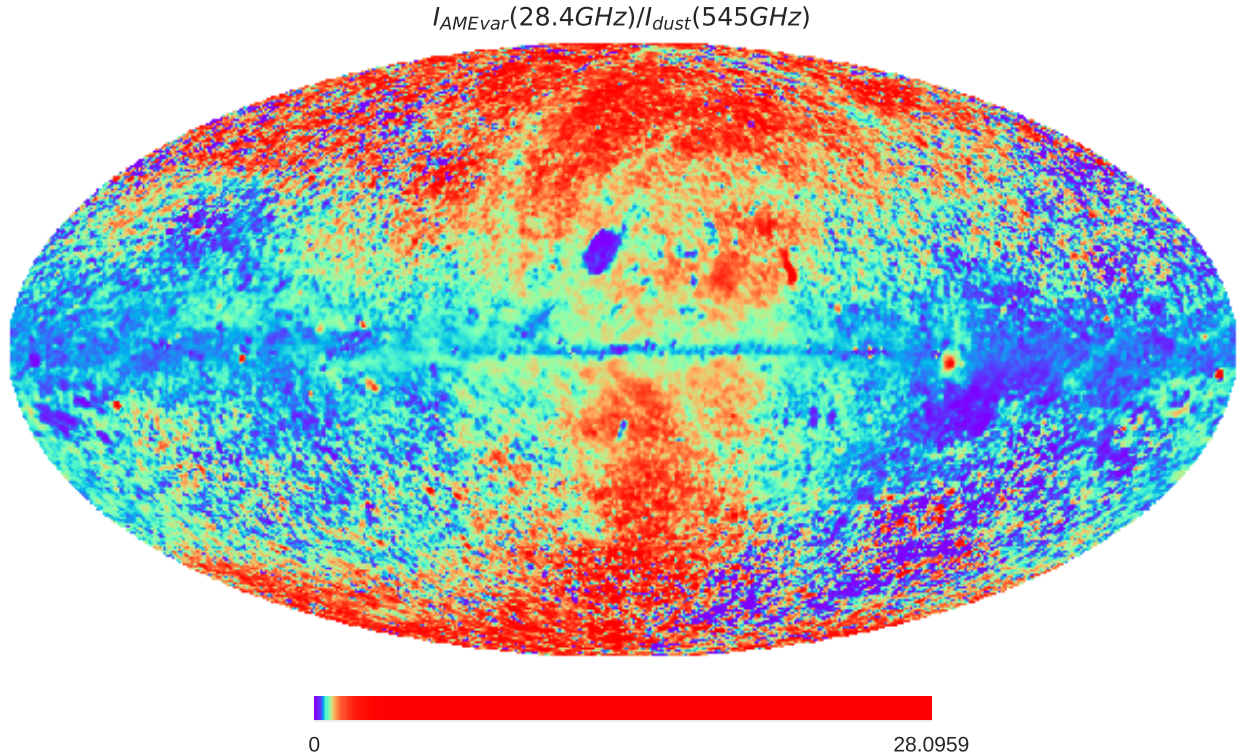


Figure 2.12: All-sky map of the ratio of two COMMANDER components- the frequency-varying AME component divided by the intensity of thermal dust emission at 545 GHz. There are some recognizable AME emission regions, such as λ Orionis. Large-scale patches of AME excess are noted to correspond to synchrotron emission (Hensley et al. 2016)

portion of) and/or higher resolution observations of not only the AME itself but the contribution from synchrotron and free-free emission. This way some of the inherent degeneracies between free-free, synchrotron, thermal dust, and AME parameters may be able to be broken.

2.5 All-sky Data Processing

The HFI, FIS, and IRIS maps used here are downloaded from their respective online repositories, as all-sky HEALPix⁶ maps (Górski et al. 2005). NSIDE 2048 maps. In the case of the IRC maps, we first create HEALPix maps from the 4,857 all-sky survey tiles using the Aladin all-sky data visualization platform (Bonnarel et al. 2000). NSIDE 2048 implies an average pixel spacing of $1.7'$. The maps are then degraded to NSIDE 1024 before carrying out a Gaussian-beam smoothing to a 1° FWHM. Map smoothing itself is done in spherical harmonic space, before the maps are transformed back to position space. These steps are handled by the smoothing function contained in the healpy python package. Following the smoothing process, the maps are degraded once more to NSIDE 256, or $15'$

⁶HEALPix core software is described at <http://healpix.sourceforge.net>. The HEALPiX python package “healpy” used in this work is available at: <https://github.com/healpy/healpy>

647 pixel-width⁷. The value of each of the larger NSIDE 256 pixels, comes from the mean of its parent
648 NSIDE 1024 pixels. The purpose of this processing is to ensure that all of the maps have the same
649 resolution as the PR2 AME map.

⁷HEALPix pixel scale rebinning carried out with healpy.ud_grade

650 Chapter 3

651 Analysis of an interesting AME region: 652 λ Orionis

653 3.1 An interesting AME region

654 The λ Orionis molecular ring, also known as the Meissa Ring is a massive stucture surrounding the
655 λ Orionis O-type star. The ring contains an HII region, ionized by LOrí itself and its OB associates
656 (Murdin & Penston 1977). What had been thought of as a starforming region of missing molecular
657 gas. At the time Murdin & Penston (1977) even speculated that this could be evidence of an alternate
658 starformation pathway, writing: “Notably we need to know if λ Ori is an example of a different mode
659 of star formation or [...] simply a case in which the progenitor molecular cloud was exhausted within
660 the last one or two million years.”

661 Maddalena (1986); Maddalena & Morris (1987). (and references therein) noted a ring of material
662 likely being pushed out by the central, historically well-known λ Orionis Association of B-type stars
663 and surrounding HII reigon.

664 3.1.1 Where does the ring come from?

665 Cunha & Smith (1996) argued that the ring may have resulted from a supernova explosion, further
666 speculating that LOrí may have been a companion of the progenitor. λ Orionis is a known binary
667 system, however its current companion is the a B-type star. (Murdin & Penston 1977) . The central
668 region is heated by the λ Orionis star itself, and the Orion OB association it belongs to (Ochsendorf
669 et al. 2015). The region is known to host several young stellar and protostellar objects (Koenig et al.

670 2015).

671 At approx. 10° wide, we can see the outline of the structure even in the low (1° FWHM) resolution
672 PCAME map. The ring shape itself is thought to originate from a supernova, or perhaps combined
673 effects of the entire star formation history of the λ Orionis Association, including the formation of its
674 surrounding HII region (Aran 2009).

675 3.1.2 A well-studied region

676 Although the λ Orionis region has been a popular target for study since approximately the 1980s. Duerr
677 et al. (1982) wrote of the relative lack of work on the overall region: “Surprisingly, this interesting
678 complex has been little studied”. While this seems surprising given the number of works on the region
679 in the literature now, it is really the advent of all-sky missions that have driven more recent interest.
680 The large angular size is such that all-sky surveys were a natural boon for study of such extended
681 structures. WISE especially was a huge source of insight (Koenig et al. 2015). More recently, Planck
682 Collaboration et al. (2016c) strongly highlighted the region as a strong candidate for further AME
683 investigation.

684 3.2 Investigative approach

685 We have carried out an initial comparison of the AME of this region with its mid to far-IR dust
686 emission. The region is shown in Fig. 3.1 as it appears in 1° -smoothed A9 data. Images at each
687 wavelength used here are included as in appendix to this thesis. The ring structure itself indicates
688 excess microwave emission attributed to AME (white contours) while the central region is dominated
689 by free-free emission (Aran 2009; Koenig et al. 2015). Free-free emission coming from the Hii phase
690 surrounding the λ Orionis association dominates the region’s morphology in LFI images. (Planck
691 Collaboration et al. 2016c). Taking the hint from Planck Collaboration et al. (2016c) that this may
692 be among the more reliably component separated regions, we evaluate if there is any preferential
693 relationship between any parameter of dust emission and the AME. Fig. 3.2 shows the expected dis-
694 tribution of free-free emission in the region, assuming that $H\alpha$ line emission is a tracer of microwave
695 free-free. This indicates that free-free is strong within the central region, where radiation fields are
696 more intense, and AME is minimal. The strongest AME follows the ring-shaped morphology outside
697 the central bubble of free-free emission.

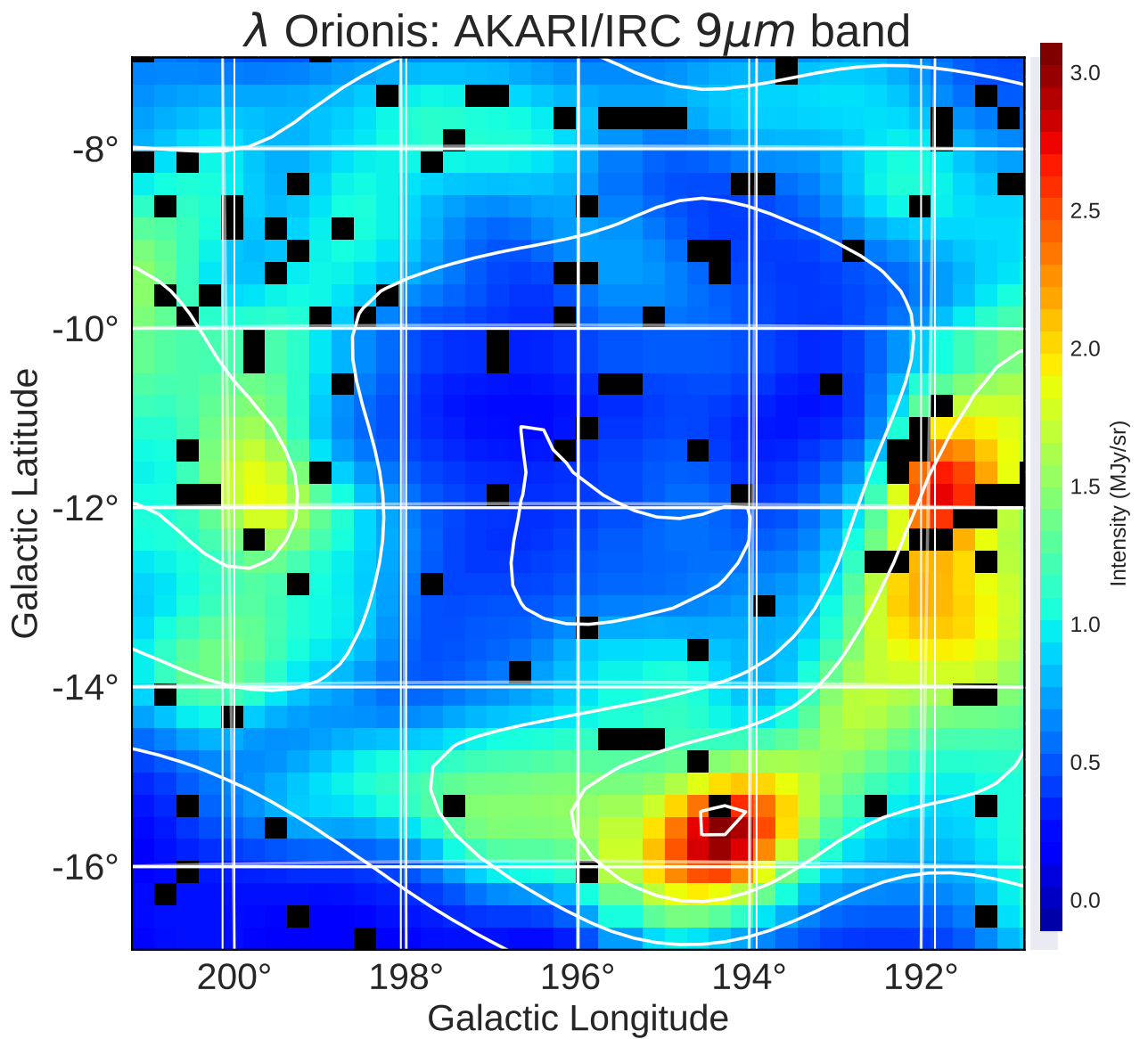


Figure 3.1: λ Orionis as it appears in the AKARI 9 μ m data. Contours indicate the AME, as given by the Planck PR2 AME map. The image is smoothed to a 1° PSF (much larger than the original 10 arcsec map). The λ Orionis star itself is approximately located at the center of the image.

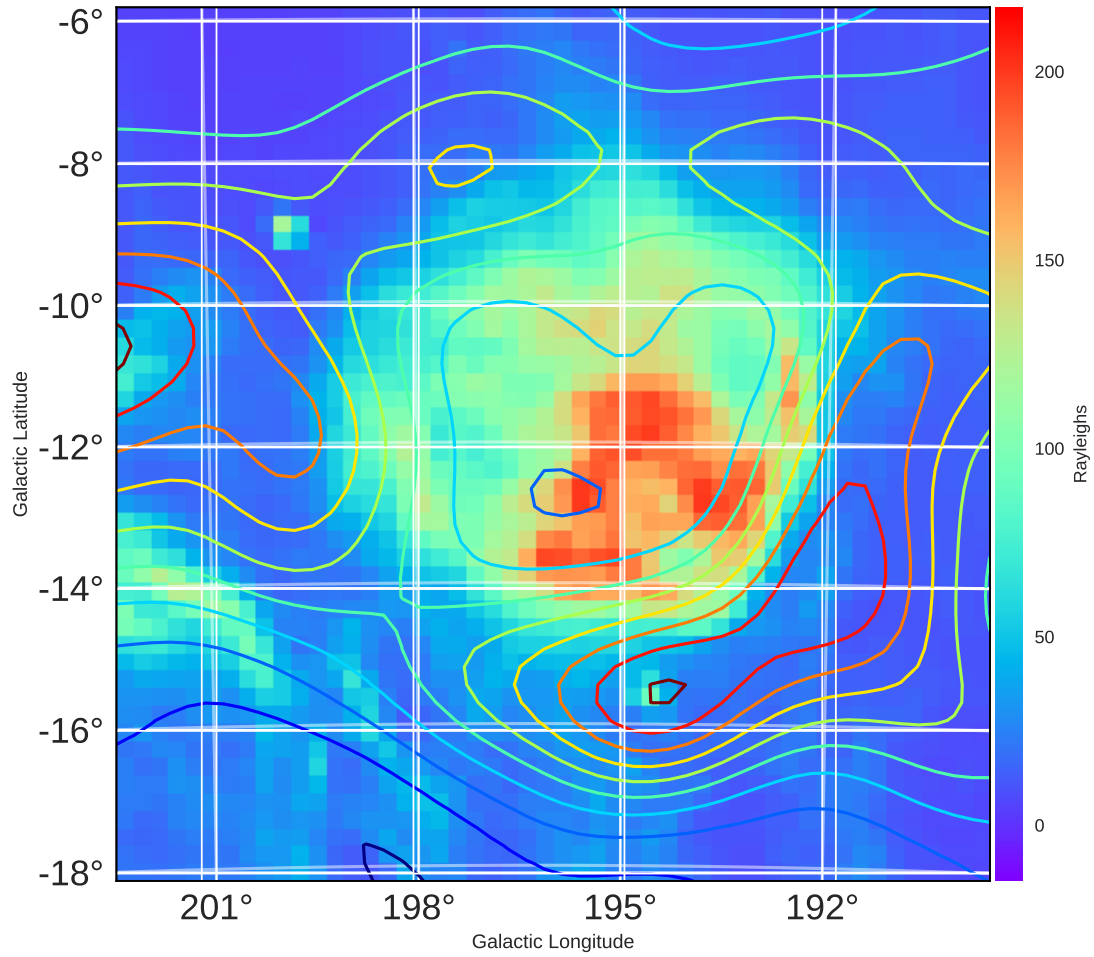


Figure 3.2: λ Orionis as it appears in H-alpha emission by ?. Contours indicate AME emission, from the variable frequency component. The colorbar indicates $H\alpha$ emission in Rayleighs. The field of view is slightly larger than that used for the IR comparison.

698 3.3 Data preparation

699 As indicated in Ch. 2, we use 12 photometric all-sky maps. For the IRC data (A9 and A18), we
 700 produce mosaics of λ Orionis from the individual tiles provided in the internal all-sky archive.¹ For
 701 the other sources, HEALPix all-sky maps are available publicly, at sufficient resolution relative to
 702 their native resolutions.²³⁴

703 3.3.1 Extraction from HEALPix maps

704 For the data obtained via HEALPix maps, we employ the “healpix2wcs” functionality provided in the
 705 “gnomdrizz” python package⁵⁶ A9 and A18 images are produced by regridding the images with the
 706 “montage” software by NASA/IPAC. All of the images for all of the bands are based on a common
 707 FITS header which has a pixel grid spacing equal to the average pixel width in the NSIDE 256
 708 HEALPix scheme. A background estimation and subtraction is made

709 3.3.2 Point-source and artifact masking

710 **Missing stripes** The AKARI all-sky survey suffers from a few missing stripe errors throughout the
 711 IRC and FIS maps (Ishihara et al. 2010; Doi et al. 2015). These are more a more serious issue for the
 712 far infrared maps. They can generally be characterized as a competition for integration time between the
 713 all-sky observing mode, and pointed observations during AKARI’s cryogenic phase. Unfortunately
 714 for the present work, some of these stripes pass directly through the λ Orionis region. Figs. 3.3 and ??
 715 display the data at near-native resolution, demonstrating where these patterns occur. Additionally
 716 there are some saturated pixels in both IRC and FIS data.

717 **Point sources** A caveat that comes with added ionized PAH feature coverage of the A9 band, is that
 718 the shorter central wavelength placement allows more contamination from point sources. We identify
 719 point sources with a moving-window approach provided in the astropy Python package, flagging
 720 pixels which have higher than 5σ intensity among the surrounding 100 pixel window. We then place

¹IRC all-sky data is still in the proprietary phase at the time of this writing, but should be public by April 2018.

²Planck data was retrieved from the NASA IPAC online archive at http://irsa.ipac.caltech.edu/data/Planck/release_2/all-sky-maps/

³AKARI/FIS data

⁴IRAS/IRIS data

⁵Available at <http://cade.irap.omp.eu/dokuwiki/doku.php?id=software>

⁶“drizzlib” 1.2.2 and earlier were not able to correctly access HEALPix files with multiple fields/columns. See appendix for our recommended workaround.

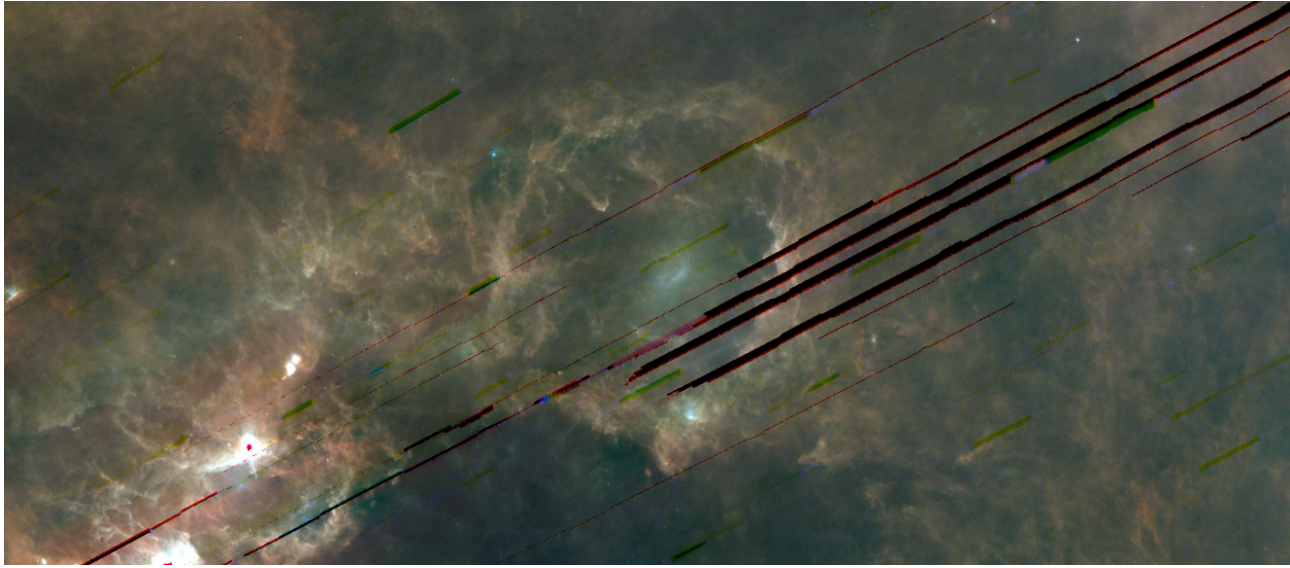


Figure 3.3: Th λ Ori ionis region and its surroundings in AKARI FIS data, where A65 is blue, A90 is green, and A140 is red. The missing stripe patterns are visible, and affect all 3 bands shown here as well as the A160 data.

721 a mask at the center of the flagged point-sources. The masks are propagated through the regridding
722 step, such that the low-resolution pixels having more than 50% of their area masked in the high
723 resolution tiles, also become masked. Such pixels appear black in Fig. 3.1. The same process is
724 applied to the A18 data. For other maps, which we extract from HEALPix data, we first regrid from
725 HEALPix to rectangular grids, and then apply the point-source search and masking as above. For
726 the I12 and I25 images, the rejected pixels were fewer than with A9, but positions overlapped with
727 those already masked in A9. For bands longer than I25, this process did not result in rejected pixels.
728 For the D12 and D25 bands, which are natively at a much lower resolution than AKARI or IRAS,
729 point-sources present more of a challenge. For these images, we visually inspect and mask 3 regions
730 with bright point source contamination consistent with the DIRBE beamsize and with point-sources
731 identified in IRAS and IRC images.

732 3.3.3 PSF Smoothing

733 We smooth the pixels in the spatial domain, to have a 1 degree FWHM PSF, in order to have a resolu-
734 tion approximating that of the PC AME data. The smoothing process relies on “convlution” module
735 provided in the “astropy” package. We assume simple circular gaussian kernel for the smoothing
736 process. While they may be asymmetries in the effective beam shapes of the IR bands used, the target
737 resolution of the AME data is large enough relative to the native resolution of the input IR data (es-
738 pecially A9 and A18, see Fig. 2.1) as to render the beam shapes and positional variations negligible.

739 Note that we do not use the image-reconstruction capability provided by the “convolve” function.
 740 Finally, we “zoom” the image, masking pixels along the edge of the FOV where the convolution
 741 produces artifacts.

742 3.3.4 Background subtraction

743 We do not expect simple band-by-band intensity correlation tests with the AME to be sensitive to
 744 background and foreground emission along the line of sight towards the λ Orionis region. The mor-
 745 phology is well pronounced and S/N is each band. However analyses such as dust SED fitting, to
 746 determine the relative abundances of different dust components, may be effected by the background
 747 level. We estimate an average, flat background level for this region. The background level is deter-
 748 mined by the two ‘OFF’ zones, indicated in Fig. ???. From pixels in these OFF zones, we determine a
 749 mean, flat background level.

750 The final images are shown in Fig. ??, with the full mask applied (masked pixels are indicated in
 751 white.)

752 3.4 Multi-wavelength characterization

753 Contours indicate the region’s shape in the PCAME map. Figure 3.12 shows IR to AME cross corre-
 754 lation plots, for all pixels within the 10° by 10° λ Orionis region.

755 The correlation matrix results corresponding to data shown in Fig. ??, are shown in Fig. 3.5. This
 756 immediately confirms a correlation between the IR and AME, however this was readily visibly from
 757 the spatial morphology of the region. Interestingly though, the correlation strengths with AME_{var}
 758 show a pattern from short to long wavelengths: A9, P857, and P545 show the strongest correlations,
 759 with the correlation weakening from A18 to A90, and again strengthening at longer wavelengths. The
 760 fixed peak frequency AME_{fix} , which is the much fainter component, shows the strongest correlation
 761 with A90- though all of the IR correlations relative to AME_{fix} are weaker than those for AME_{var} .
 762 The overall pattern is for bands dominated by PAH emission (as discussed in Ch. 2), and those which
 763 trace Rayleigh-Jeans thermal dust emission are equally good predictors of the AME. Bands dominated
 764 by a mixture of VSGs, and warm dust emission, show a weaker correlation. Comparing the images
 765 in Fig. ??, most of the variation in the correlation scores appears to come from the central region of
 766 λ Orionis. Because of the known heating present within the ring, from the λ Orionis association, and

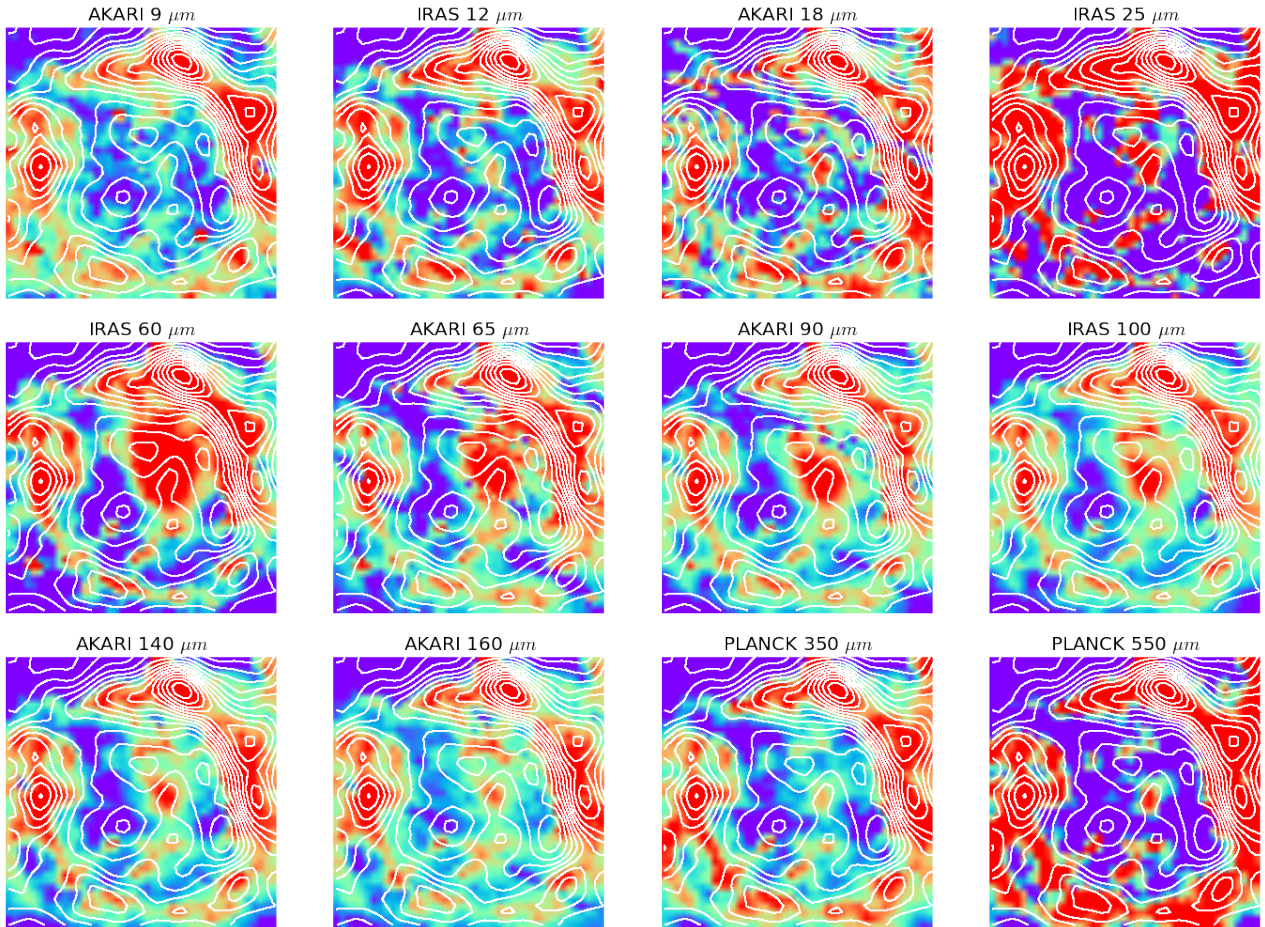


Figure 3.4: A grid of thumbnails showing the λ Orionis region's structure, at 12 wavelengths, along with AME contours (shown in white contours). Spatial correlation seems to be the best at the shortest and longest wavelengths (AKARI/IRC 9 μm and Planck/HFI 550 μm). The images are smoothed and interpolated for demonstration. Figure 3.1 demonstrates the actual pixel grid used for the SED fitting and intensity correlation tests.

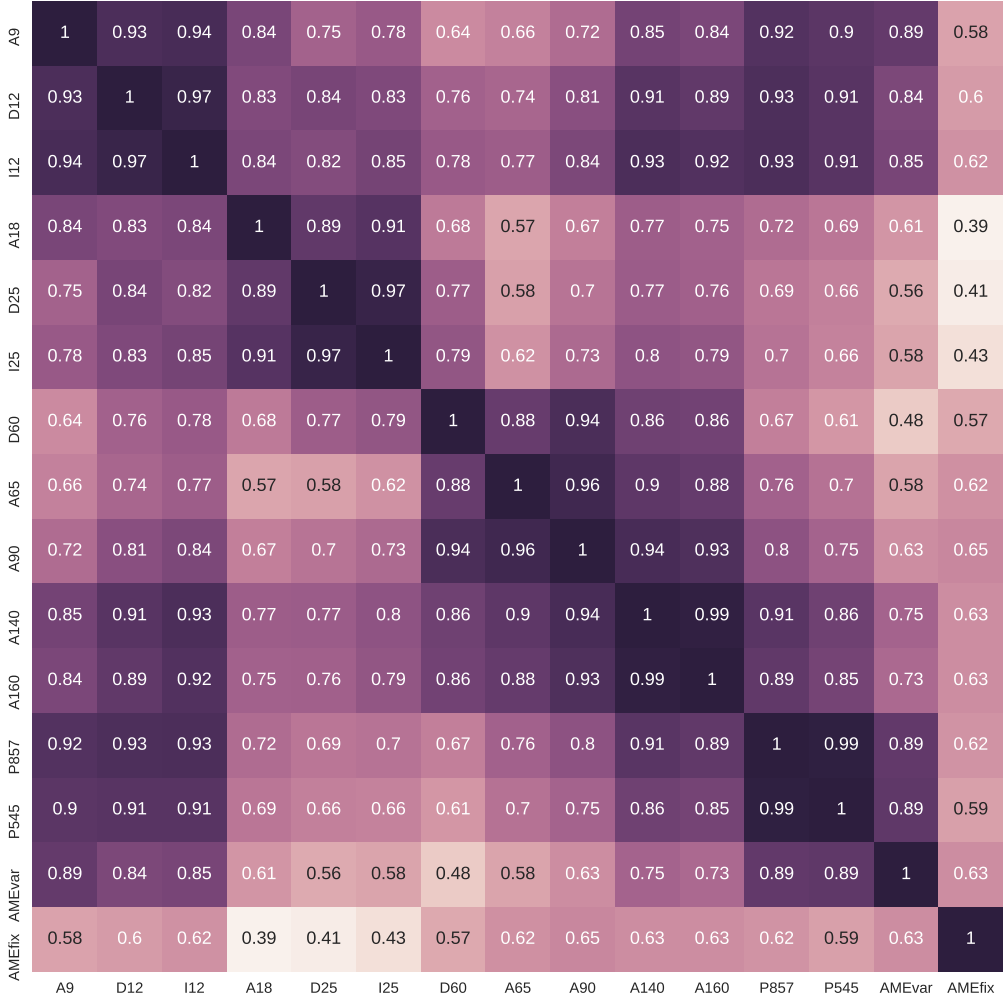


Figure 3.5: r_s correlation matrix for all of the data used in the λ Orionis analysis, similar to that presented for the Planck Commander component maps in Fig. 2.7. The shade and annotation for each cell indicates the r_s score, where r_s of 1 indicates a monotonically increasing relationship for a given pair of images. The two AME components, as described in Ch. 2, are listed separately: AME_{var} for the frequency-varying component, and AME_{fix} for the constant frequency component.

767 given the brightening of bands between A18 and A90, this variation appears to be due to a temperature

768 increase.

769 **3.4.1 Bootstrap analysis**

770 To assess the robustness of the correlation scores, we employ the Bootstrap re-sampling approach,
771 first introduced by Efron (1979) (see Feigelson & Babu (2013) for an updated description within
772 an astronomical context). This involves creating random re-sampled sets of the data. We use the
773 ‘with replacement’ approach, meaning that a data point may be selected multiple times in a single
774 re-sampling iteration. The size of the re-sampled set is the same as the input set size. For each random
775 set we run a correlation test, resulting in a distribution of correlation coefficient. This allows us to
776 estimate error bars for the correlation scores. We carry out bootstrap correlation tests for each IR
777 band’s intensity vs. the AME_{var} intensity. The data are resampled 10,000 times for each correlation
778 test. This is repeated for both r_s and r_p based tests. The distributions of the bootstrap resamplings are
779 shown in Fig. 3.6. For both test cases, the best correlations are the longest and shortest wavelength
780 bands, consistent with the straight-forward r_s scores shown in Fig. 3.5. In the r_p case, the strongest
781 correlation is the A9 band vs the AME.

782 **3.5 Comparison with SED Fitting**

783 We performed a full dust SED fitting on the λ Orionis photometry, according to the dust model by
784 Galliano et al. (2011) (to be thoroughly introduced in Galliano, et al., in prep.) We used a mixture
785 of silicate and carbonaceous dust, silicate dust, the two dominant categories of interstellar dust as
786 described in Ch. 1. However, instead of the graphite-based carbon dust invoked by the canonical
787 Draine & Li (2007b) model (DL07), we assume amorphous carbon. This choice is an attempt to
788 account for the “sub-mm excess” of dust emission, reported by Israel et al. (2010); Bot et al. (2010),
789 in the Large Magellanic Cloud (LMC). The increased emissivity of amorphous carbon (a factor of
790 2-3 more than DL07) allows a better fit to Herschel observations of the LMC (Galliano et al. 2011),
791 and Planck observations of the Milky Way (Planck Collaboration et al. 2016d). We assume that the
792 radiation field heating this dust mixture is the Galactic ISRF (Mathis et al. 1983), scaled by a factor
793 U . We also assume, following Dale et al. (2001), that the dust is exposed to a distribution of starlight

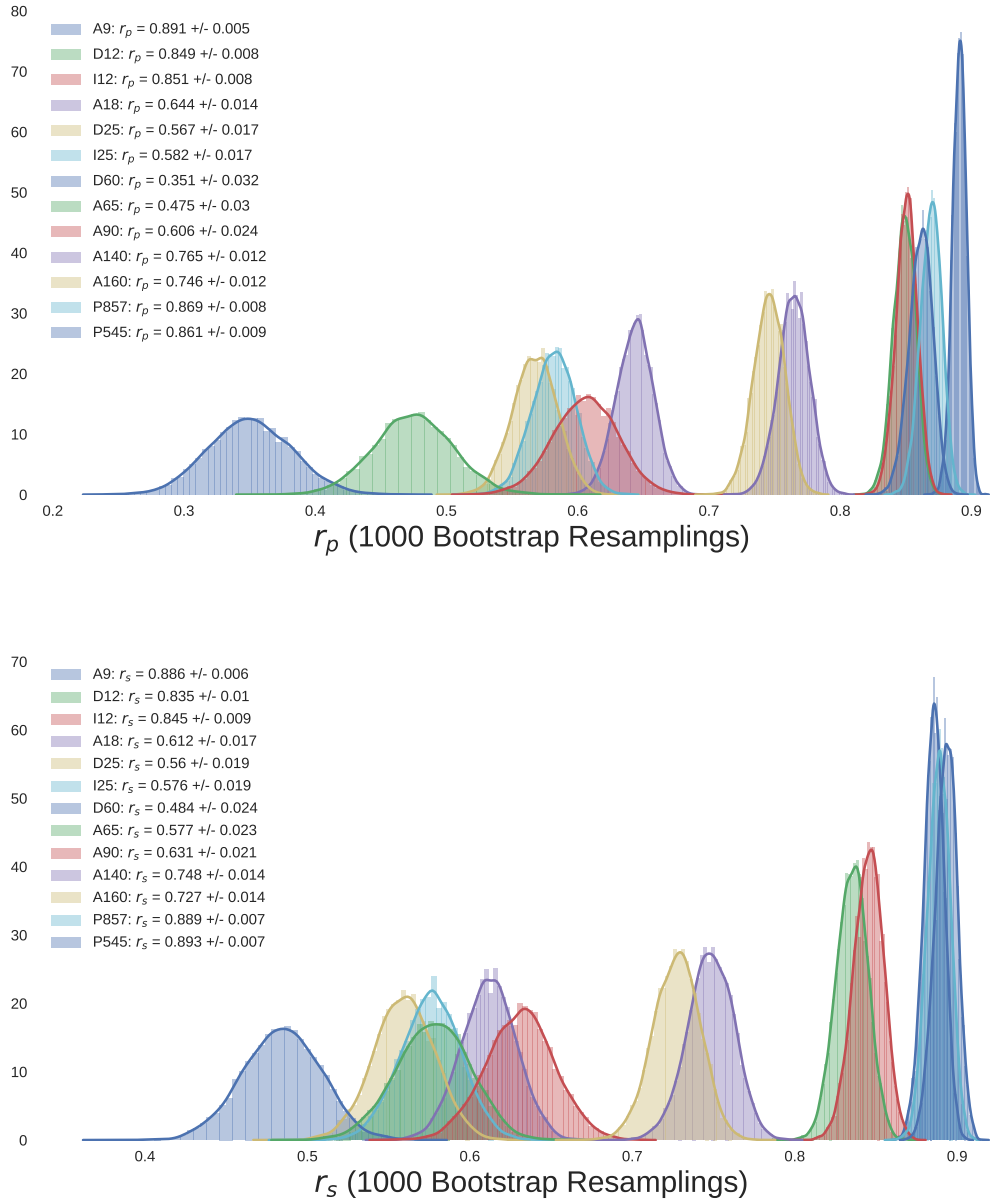


Figure 3.6: Re-sampled (Bootstrap) correlation tests for IR emission in λ Orionis vs. AME, for both Spearman and Pearson correlation tests.)

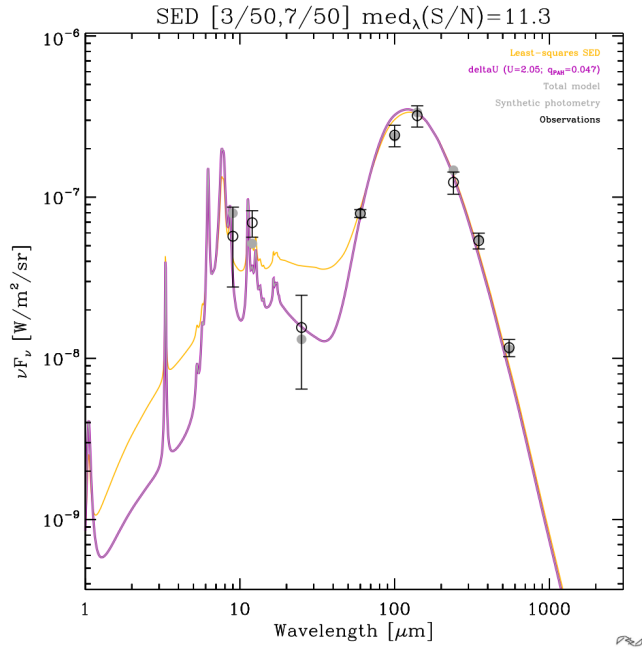


Figure 3.7: Observed (black circles and errors) and synthetic photometry (gray dots) SED of a pixel within λ Orionis, along with the dust SED model fit results. Two SED fits are shown: one for the Bayesian fitting (magenta), and another showing the standard least-squares result for comparison (yellow). The fitted ISRF strength U , and fraction of mass in PAHs, q_{PAH} are also given.

794 intensity, distributed as:

$$dM_{dust} \propto U^{-\alpha} dU \quad (3.5.1)$$

795 between U_{min} and U_{max} , where U_{min} , U_{max} and α are free parameters. We utilize both the Bayesian
 796 dust SED fitting approach by Galliano (in prep.), and a least-squares analysis. The SED fitting
 797 accounts for estimates of the respective calibration uncertainties, and the spectral response curves
 798 (Fig. 2.1). As outputs, metrics of the total dust mass M_{dust} , PAH mass M_{PAH} , ionized PAH mass
 799 M_{PAH+} , and ISRF intensity U are produced. We only carry out the fitting for unmasked pixels. We
 800 are primarily interested in which of the correlations M_{dust} vs. I_{AME} or M_{PAH} vs. I_{AME} is stronger.
 801 Two sample fitting results are shown in Figs. 3.7, and 3.8. Performing such fits for all of the pixels,
 802 we are able to see how I_{AME} varies with the bulk dust physical characteristics of the region. Fig. 3.9
 803 shows the fitted dust mass per pixel, relative to the AME intensity. AME intensity is scaled by the
 804 ISRF intensity U . Although spinning dust emission is not predicted to vary directly with U , we con-
 805 sider that the ISRF may serve as a diagnostic of environmental conditions in the ISM. In any case,
 806 we find that performing such a scaling improves the correlations with dust mass. Figs. 3.10 and 3.11
 807 describe the variation with M_{PAH} and M_{PAH+} . Based on the dust properties derived from these SED
 808 fits, we attempt investigate whether any fitted parameter shows a preferential relation with the AME.

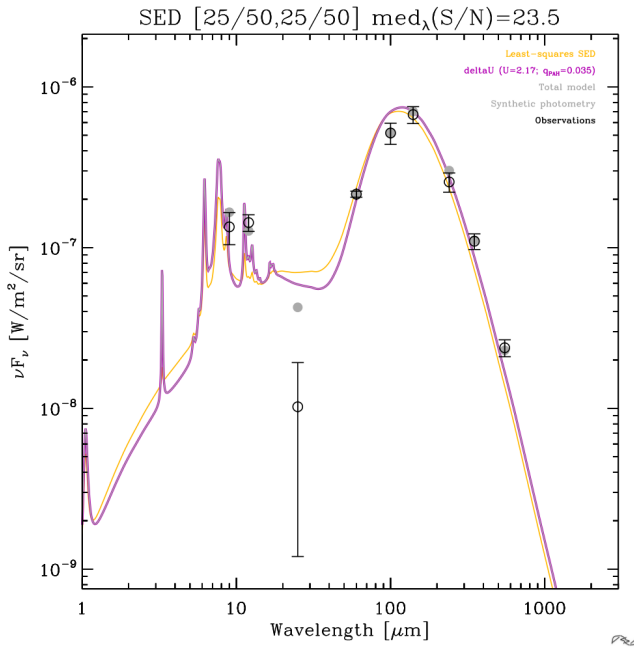


Figure 3.8: The same as Fig. 3.7, but for a different pixel position. Corresponds to galactic coordinates...

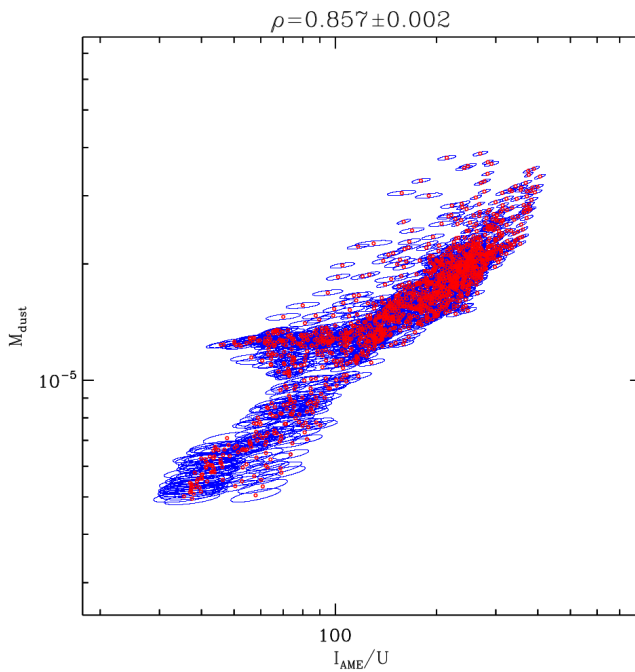


Figure 3.9: Scatter plot with error ellipses generated through the Bayesian SED fitting, of total dust mass M_{dust} vs. I_{AME} scaled by U .

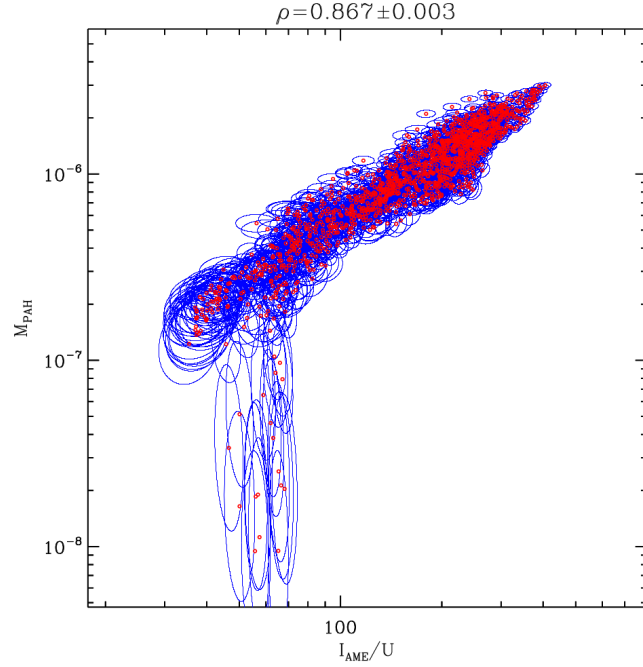


Figure 3.10: The same comparison is given by 3.9, but showing total mass of PAHs (M_{PAH}) rather than total dust mass on the y-axis.

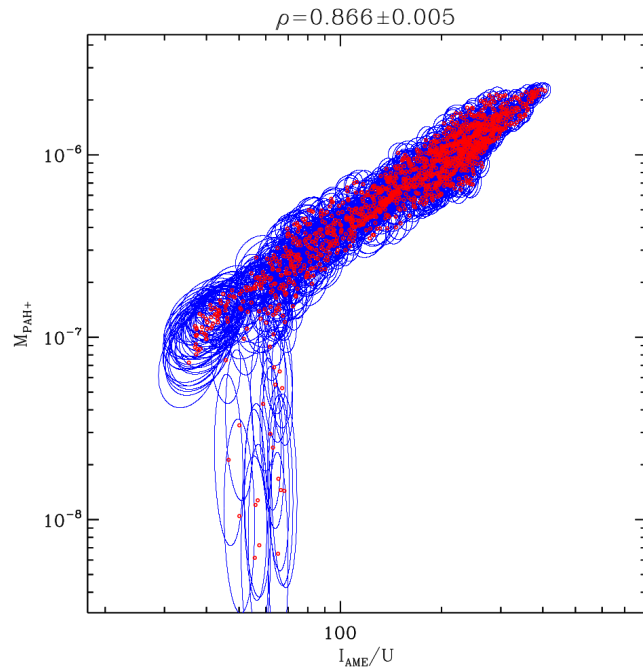


Figure 3.11: The same as in Figs. 3.9 and 3.10 , but specifically comparing an estimate of the ionized component of PAH mass.

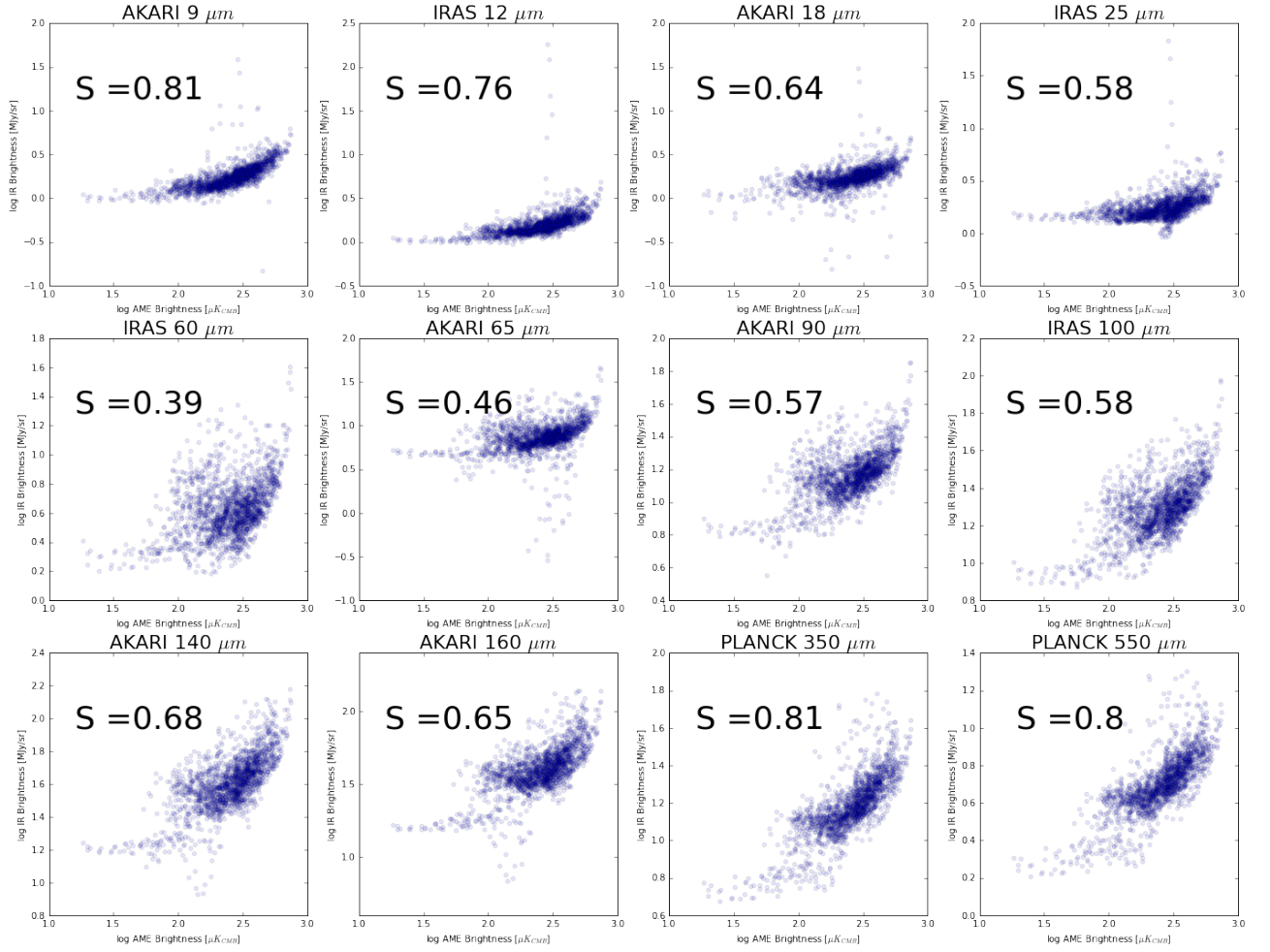


Figure 3.12: Intensity cross-correlation for all pixels in the λ Orionis cut-out region. r_s indicates the Spearman rank correlation coefficient for each plot.

809 3.5.1 Comparison with unmasked results

810 To assess the effect of applying the mask and background subtraction from Sec. 3.3, Fig. 3.12

811 3.6 Discussion

812 In λ Orionis we found that across the whole region, A9 emission and P545 emission were the most
 813 strongly correlated with AME. This is apparent both in the photometric band analysis, and in the dust
 814 SED fitting. The fact that the correlation strengths of PAH-tracing mission and sub-mm emission
 815 are similar is in-line with what we have seen in Ysard et al. (2010) and Hensley et al. (2016). In
 816 those works, the two relationships (MIR vs. AME and FIR vs. AME) are very close, although
 817 these two papers are odds as to which relationship is stronger, and thus in their final interpretation.
 818 With the present data and analysis of λ Orionis, we fail to rule out PAHs as carriers of the AME.
 819 Fig. 3.13 indicates that although total dust mass and PAH mass are both correlated with AME, there

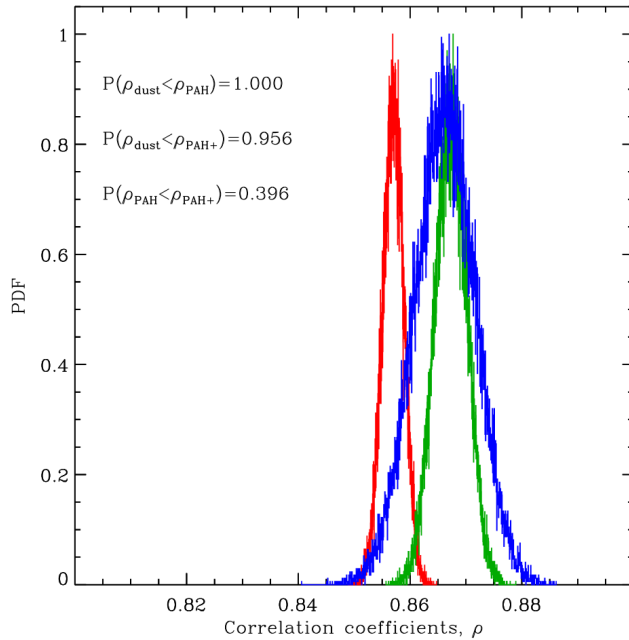


Figure 3.13: The Bayesian correlation probability distributions of Pearson's correlation coefficient (ρ) for the three physical parameters vs. the AME intensity: total dust mass, ρ_{dust} (red); total PAH mass ρ_{PAH} (green); and only the ionized PAH mass ρ_{PAH+} (blue). Also given are the probabilities of either PAH component being better correlated with AME than dust mass, as well as the probability that ionized PAH mass correlates better than total PAH.

is a strong (100%) probability that PAH mass is the stronger predictor of AME intensity. The results are consistent with a scenario in which PAH mass, cold dust, and the AME are all tightly correlated. Weaker correlation from 25 to 70 μm may indicate that AME is weaker in regions of warmer dust and stronger radiation fields. Such an anti-correlation with harsher radiation are consistent with the carriers of AME being destroyed in the central region of λ Orionis, thus leading to substantially decreased spinning dust emission.

3.6.1 PAH Ionization fraction

As described in Ch.2 it is expected that relative variations between the A9 and I12 intensities could be explained by the fraction of PAHs that are charged. Simply examining λ Orionis in intensity, we find that the A9 intensity correlates more strongly with AME than I12 or D12. In the Pearson correlation case, A9 correlates more strongly with AME than any other band. This is consistent with the spinning PAH hypothesis, and taken alone may that the 6.2 μm feature emission from ionized PAHs, may be a better predictor of AME intensity.

As shown by the dust SED fitting however, the probability distributions (Fig. 3.13) of $r_p(M_{PAH+} : I_{AME})$ does not indicate that ionized PAH mass correlates better with the total PAH mass. Attempts to

835 estimate the PAH fraction based on the available data appear to only add noise relative to $r_p(M_{PAH} : I_{AME})$.
836 The means of the two distributions $r_p(M_{PAH+} : I_{AME})$ and $r_p(M_{PAH} : I_{AME})$ are similar
837 and $r_p(M_{PAH+} : I_{AME})$ shows a wider distribution.

838 Thus the question of whether or not AME comes predominantly from charged PAHs remains
839 open. The fact that A9 correlates more strongly than the 12 μm bands, at least suggests that this topic
840 is worth further investigation. Future wide-area spectral mapping of the λ Orionis region would be
841 able to indicate precisely which PAH features are dominating the A9 and I12 emission, and infer the
842 charged PAH fraction with higher confidence than we can do with wide photometric band ratios. Such
843 observations could be coupled with higher resolution constraints of the AME variation, and a more
844 reliable fitting of the peak frequency of the AME.

845 **Chapter 4**

846 **All-sky Analysis**

847 What we present here is a test of the generalizability of results from Ch.3, which focused on a par-
848 ticular structure on the sky, λ Orionis. We first would like to note that “all-sky analysis” can be a bit
849 misleading. The term tends to lead readers to the idea of a definitive study, answering a particular
850 question for any given position on the sky. While a truly all-sky analysis would be ideal, signal-
851 to-noise constraints (mainly at high galactic latitudes), as well as confusion along the line of sight
852 (mainly in the galactic plane), make a uniformly powerful study of the whole sky very challenging.
853 Here we will indeed show results for the entire sky as a benchmark analysis, but for the core analysis
854 we must mask certain regions dominated by systematic effects in order minimize biases for particular
855 wavelengths.

856 **4.1 Resolution matching**

857 **Smoothing**

858 As in Ch. 3, this approach applies to a spatial resolution of approximately 1° . The resolution limim-
859 tation is imposed by the PC microwave component maps, which list an ‘effective resolution’ of $60'$
860 (Planck Collaboration et al. 2016b). Thus we must apply a smoothing to most of our input datasets,
861 which have native resolutions of a much finer scale (see Tab. 2.1), and Fig. 1.2. The data also come
862 in a wide range of beam shapes with their own degrees of uncertainty, thus we conservatively smooth
863 all of the data in the same way, using a circular Gaussian beam, to have 1° FWHM resolution. we ar
864 We start with an all-sky AME to IR comparison, looking for global patterns among all pixels.

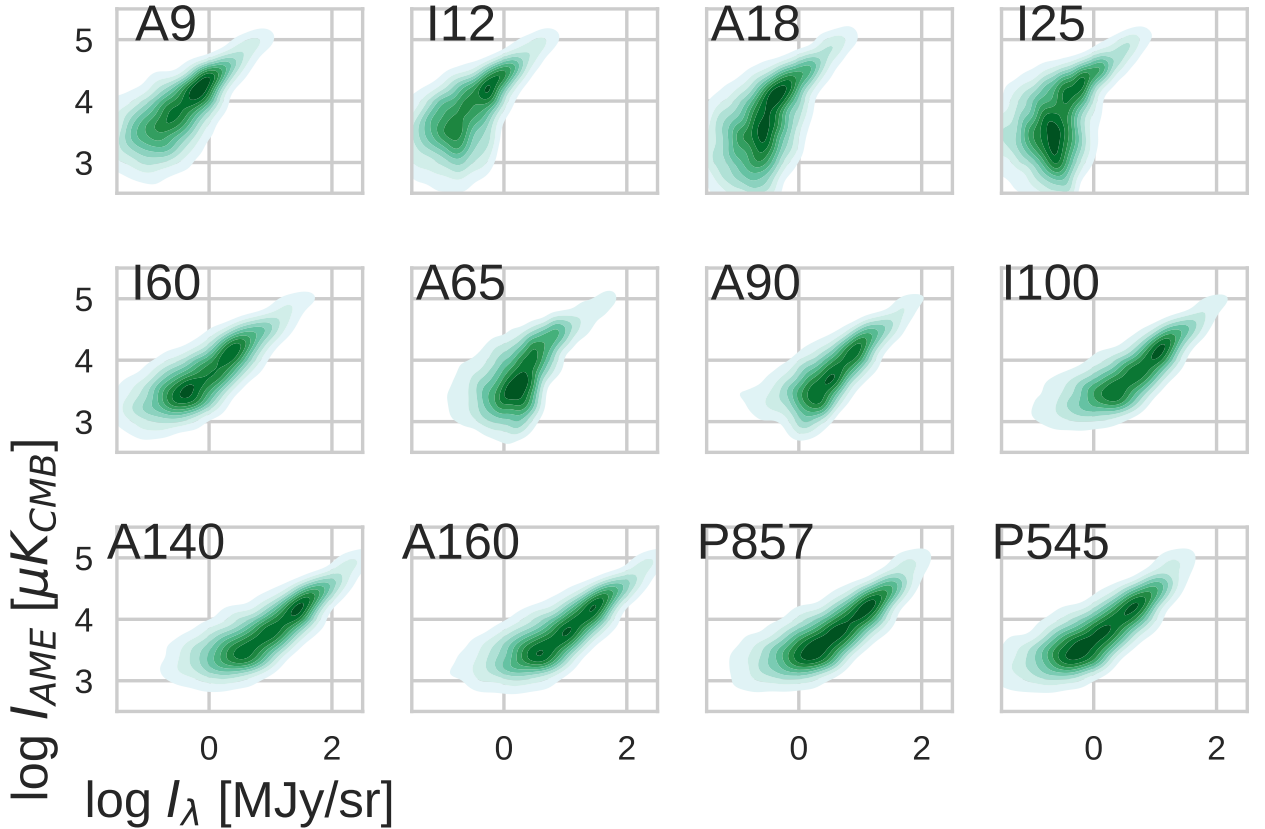


Figure 4.1: Point-density distributions of the AME intensity (Y-axis) vs. the IR bands' intensities. Darker regions indicated higher pixel densities. Only a simple mask of pixels near the ecliptic plane has been applied.

4.2 All-sky cross correlations

In order to look more closely how the the AME to IR relationship varies with wavelength, we first do a comparison without applying any pixel mask, as a benchmark. Fig. 4.1 shows the pizel-density plots of AME vs. the IR bands' intensities. Darker regions show higher pixel densities, unshaded or more lightly shaded regions show low or zero pixel densities. We see immediately that each band shows evidence of a positive trend with AME intensity, as in Ch. 3. For the MIR bands, at lower IR intensities we see the effects of detector noise become dominant, turning into a more defined positive trend with increasing IR intensity. This effect is less pronounced in the FIR. We consider that the IR maps used must not only be compared to the AME, but to each other, to assess multi-wavelength patterns. We also compare the AME and IR maps to ancilliary maps, as decribed in Ch. 2 and Tab. ??.

Fig. 4.2 confirms the weaker trend in the MIR vs. AME, via a cross-correlation matrix, similar to that used in Ch. 3 and Fig. 3.5. This is reflected in the comparison between high and low latitude plots: for pixels $|\beta| > 15\text{deg}$, we see a dramatic effect. In the most extreme case r_s of A18 to AMEvar drops from 0.72 at high latitude, to 0.02 at lower latitudes. $r_s(A9 : AME_{var})$ drops from 0.79 to

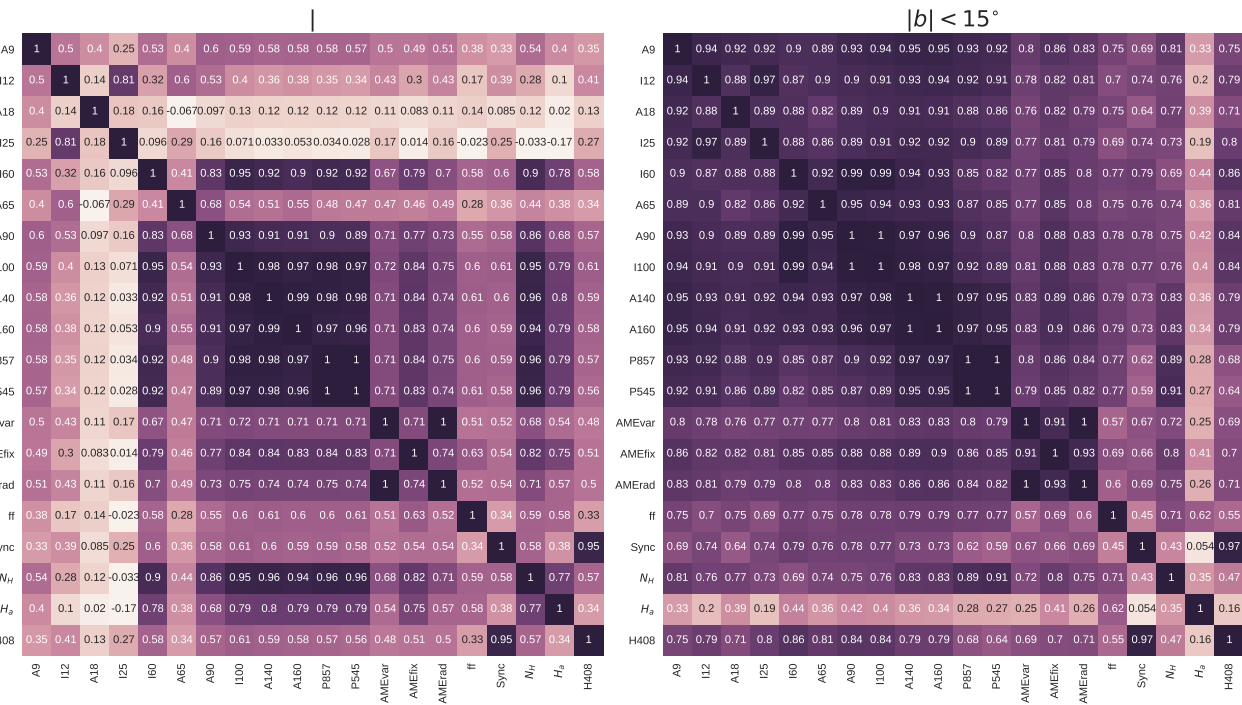


Figure 4.2: ALL-SKY cross-correlation matrix for the 12 infrared bands sampled, as well as the PC component maps described in Ch. 2: the two AME components evaluated at their peak frequencies AME_{var} , AME_{fix} ; Syncrotron, and free-free), and ancillary maps of N_H , H_α emission, and 408 MHz emission Haslam et al. (1982). The color-scale indicates (r_s). Results are based on the unmasked sky, but are split by Galactic latitude: pixels with $|\beta| < 15deg$ (left) and $|\beta| > 15deg$. The color and annotations indicate r_s as in Fig. 3.5.

42. Correlations between the MIR bands and FIR bands also weaken. Only the the interrelations
 879 between the FIR bands from I60 to P545 remain eseentially latitude independent (with the exception
 880 of A65, which has an especially high noise level.)

882 In the lower latitudes, with $|\beta| < 15deg$, bright emission in and around the galactic plane seems to
 883 homogenize the bands. We see little change from band to band both in terms of the relationship with
 884 AME or with other IR bands. Thus the increase of S/N with decreasing brightness at higher latitudes
 885 has a strong effect on such intensity correlation tests. Bands tracing bright thermal dust emission at
 886 higher latitudes are more robust against this effect. The only case where the trend is reversed, is with
 887 the maps of $N(H)$ and H_α . Both of these maps show higher r_s when compared to high latitude FIR
 888 emission. The next section descibes a pixel-masking strategy designed to mitigate both r_s suppressing
 889 effects from band-to-band S/N variations, and r_s enhancing effects from confusion near the galactic
 890 plane.

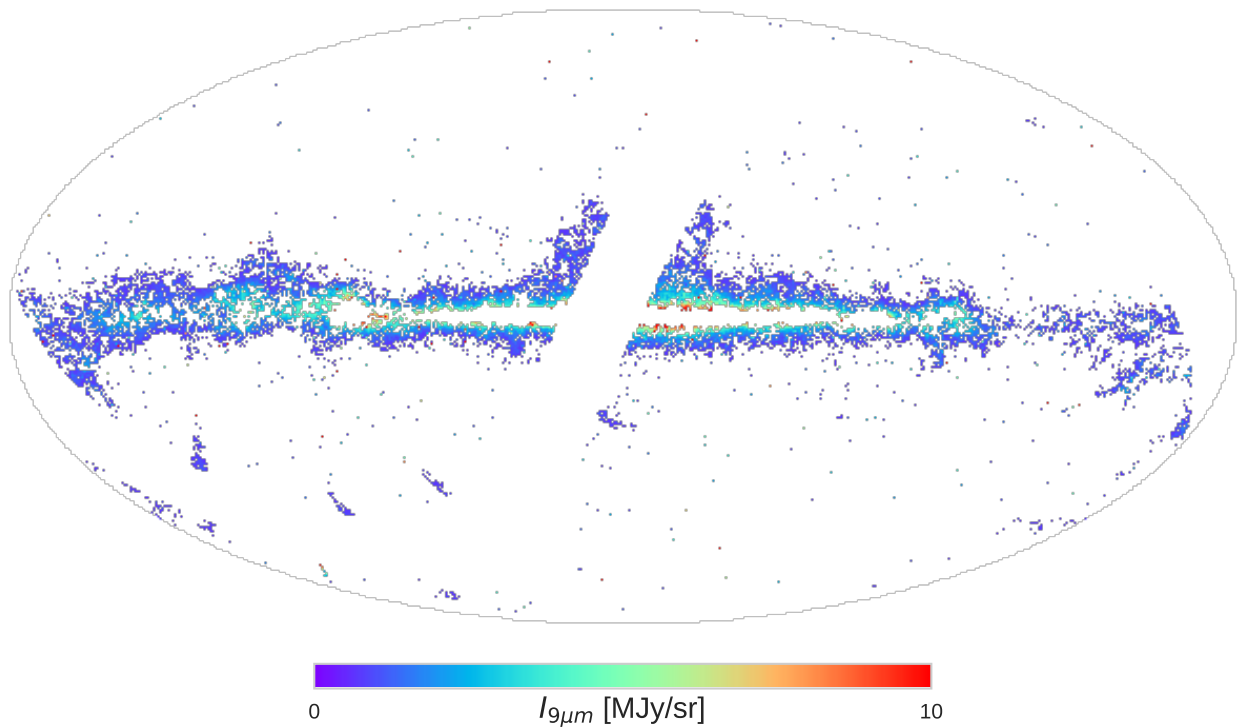


Figure 4.3: All-sky map in A9 emission after applying the combined masks: ecliptic plane, galactic plane, point sources, and pixels with $S/N < 1$. This mask essentially outlines the galaxy, except for the most confused regions.

891 4.3 Masked Comparison

892 For the reasons described in the previous section, we consider that an exhaustive comparsion of the
 893 AME with IR requires the use of a pixel mask. In this section we describe the various masks applied
 894 to the full dataset. We then repeat both the comparisons above (as in Figs. 4.1 and 4.2) for the masked
 895 dataset, and present additional analyses. The full mask, applied to the A9 map, is shown in Fig. 4.3.
 896 The same mask is applied to all maps, including the AME.

897 4.3.1 Pixel mask

898 We prepare a global pixel mask (pixel positions masked in any map are excluded from the analysis).

899 **Zodical light** To keep our analysis comparable to previous works, we exclude pixels within 10° of
 900 the ecliptic plane (Hensley et al. 2016). Even though we use the Zodi-subtracted maps (Kelsall et al.
 901 1998; Kondo et al. 2016; Ootsubo et al. 2016), the Zodi residuals are still problematic (especially in
 902 the MIR.) This corresponds to regions with the heaviest contamination from Zodiacal light, where
 903 Zodi residuals are apparent even with visual inspection for all of the MIR bands used in this study. In

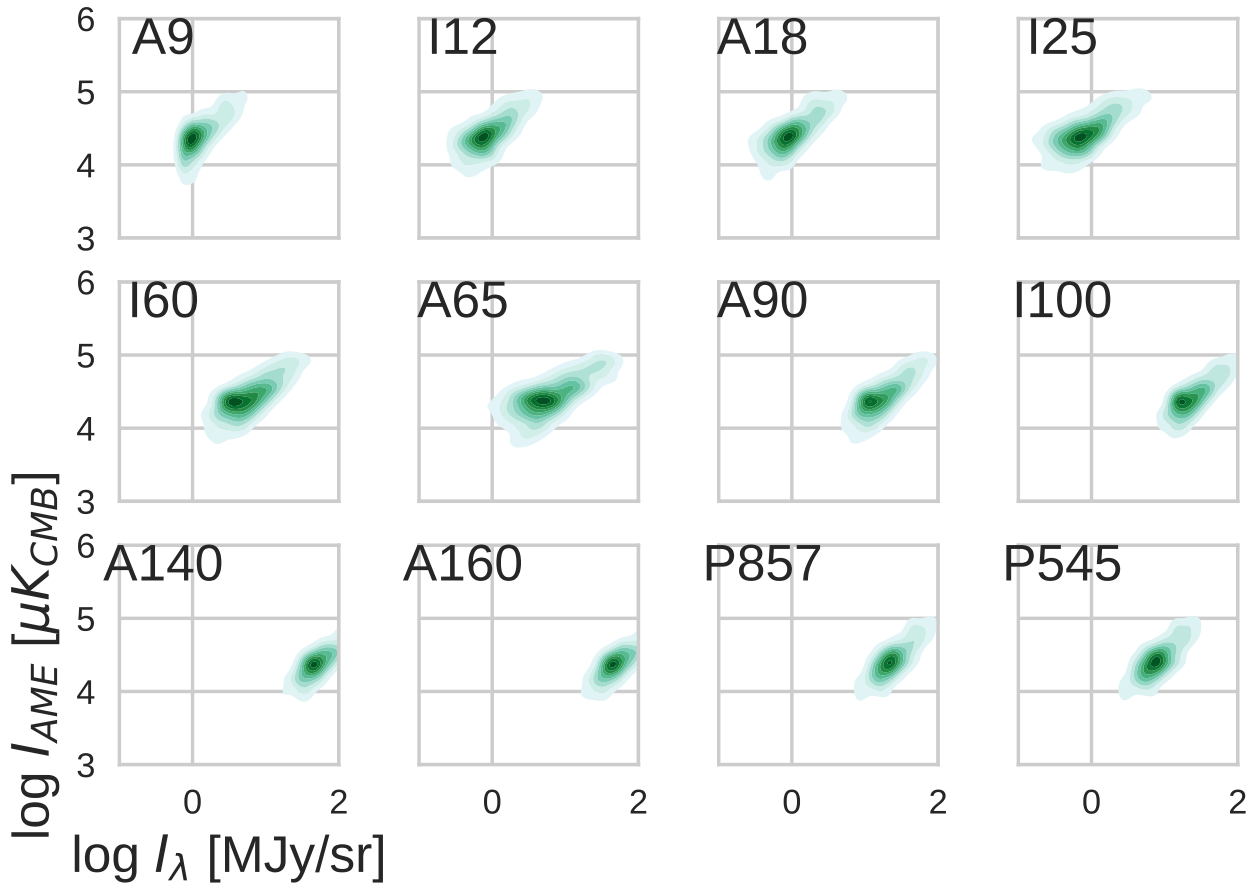


Figure 4.4: The same comparison as shown for Fig. 4.1, but with the mask applied as in Fig. 4.3.

904 Ch. ??, Figs. 2.5, and 2.5 clearly display these residual patterns.

905 **Signal to noise** Some of the bands used lack sufficient sensitivity to trace fainter emission, espe-
906 cially at higher galactic latitudes. This is mainly an issue for the mid-infrared bands. As such, we
907 enforce a 3σ threshold for all of the maps— adding to the mask any pixel that has lower than σ
908 detection in any of the maps. This removes nearly all pixels beyond approx. 15 degrees from the
909 galactic plane, with the pronounced exception of regions affected by stray moonlight. The extent of
910 this particular mask is primarily defined by the IRC A9 and A18 maps, which have the highest noise
911 levels.

912 **Point Sources** The Planck Collaboration provides masks of the pixels they find to include point
913 sources. We mask pixels which are flagged as being point-source contaminated, in the most heavily
914 affected maps: Planck/HFI 857 GHz and Planck/LFI 30 GHz. Fig. 4.4 shows point-density plots for
915 AME_{var} vs. each of the IR bands, after applying the mask described above. As expected with such a
916 drastic reduction of the number of noise-dominated points, the scatter, especially for the MIR bands,

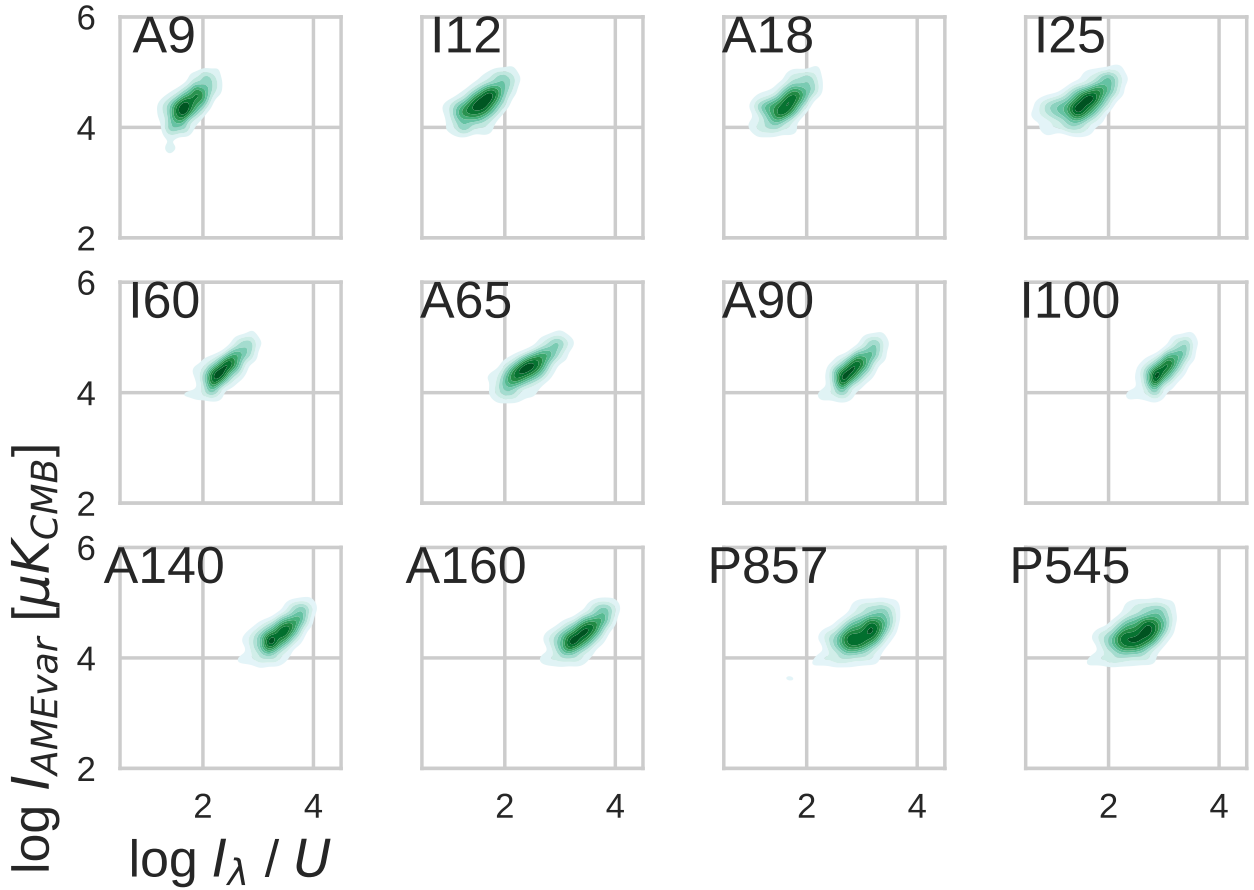


Figure 4.5: Similar comparison to Fig. 4.1, with the IR intensities scaled by U for each pixel.

is reduced. Otherwise the application of the mask does not bring about any special distinction among the bands when compared to the AME. What is notable however is that the persistent weakening of trend of I25 vs. AME, relative to A9 and the FIR bands. Following the logic that the PAH-tracing bands intensity is essentially a product of the ISRF (U) and the column density of PAHs (σ_{PAH}), we redraw the comparison after scaling the IR bands by U . We do this not only for the MIR bands, simply for comparison. We do not have a theoretical prediction as to the relationship between AME intensity and the FIR bands' intensities scaled by U . The pixel density plots for such a comparison are given by Fig. 4.5, which is the same as Fig. 4.4 except for division of the X-axes by U . Corresponding to the plots vs. AME given in Figs. Fig. 4.5 and 4.4, we again perform a cross-correlation matrix test, to understand how the bands relate to one another- not only to the AME. This cross-correlation is done for both intensity, shown by Fig. 4.6 and U normalized intensities showin in Fig. 4.7.

Bootstrap test In addition, for the masked comparison, we carry out a bootstrap analysis similar to that discussed in Ch. 3 and Fig. 3.6. The Spearman rank correlation coefficents r_S of all of the bands, in intensity, vs. the $AMEvar$ component are shown. This is done only for the masked case, due to

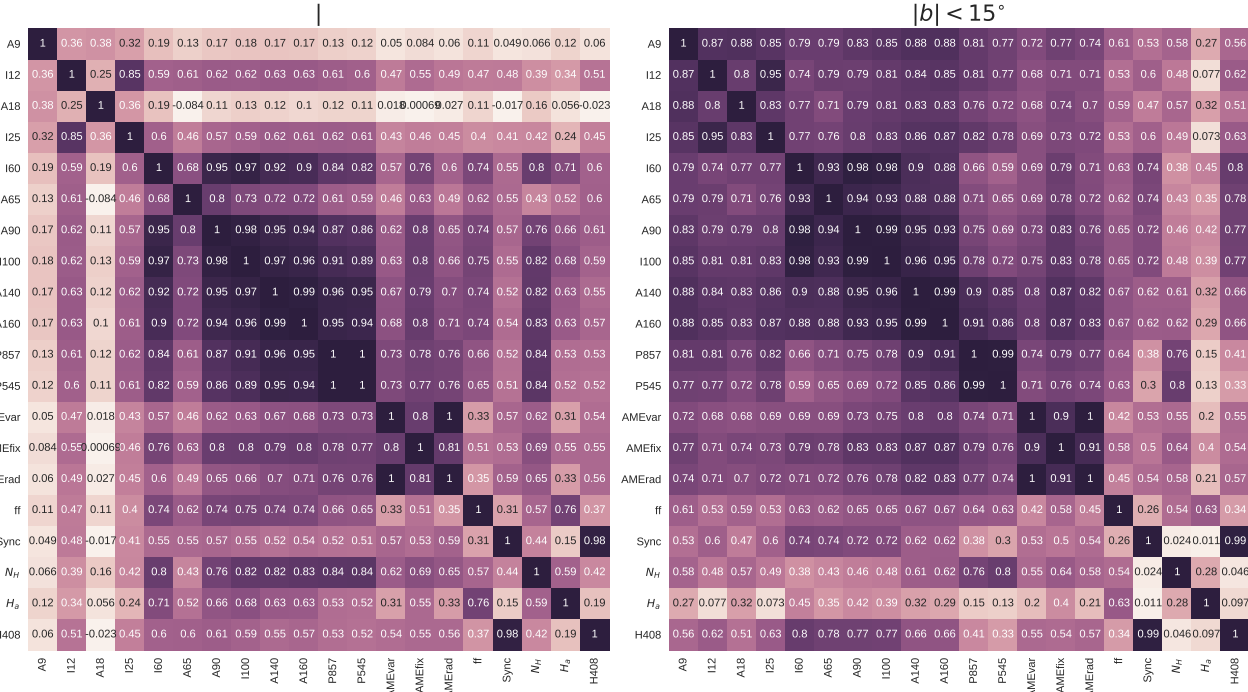


Figure 4.6: Cross-correlation (r_s) matrix for the IR intensities (unscaled) vs. each other, essentially the same comparison as in Fig. 4.2, except that the pixel mask is applied.

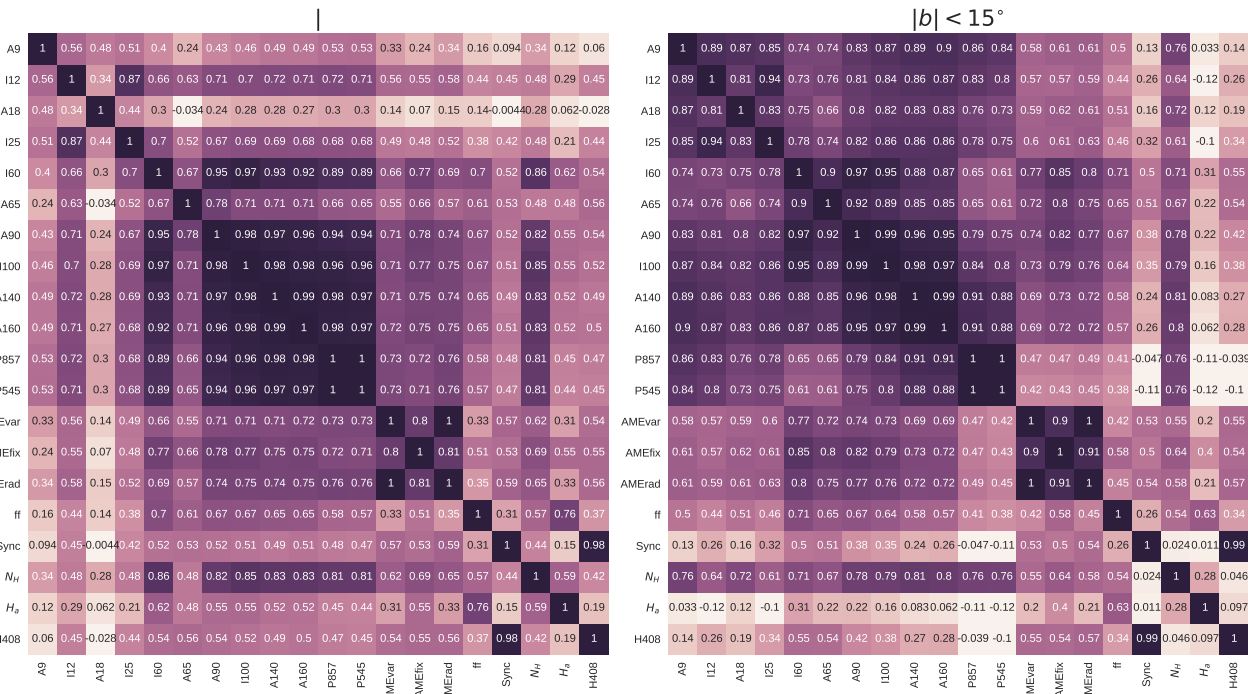


Figure 4.7: Cross-correlation (r_s) matrix for the U -normalized IR intensities vs. each other, and also against the AME components, other PC products, and ancillary data. Only the IR maps are divided by U -other data is unchanged from Fig. 4.6)

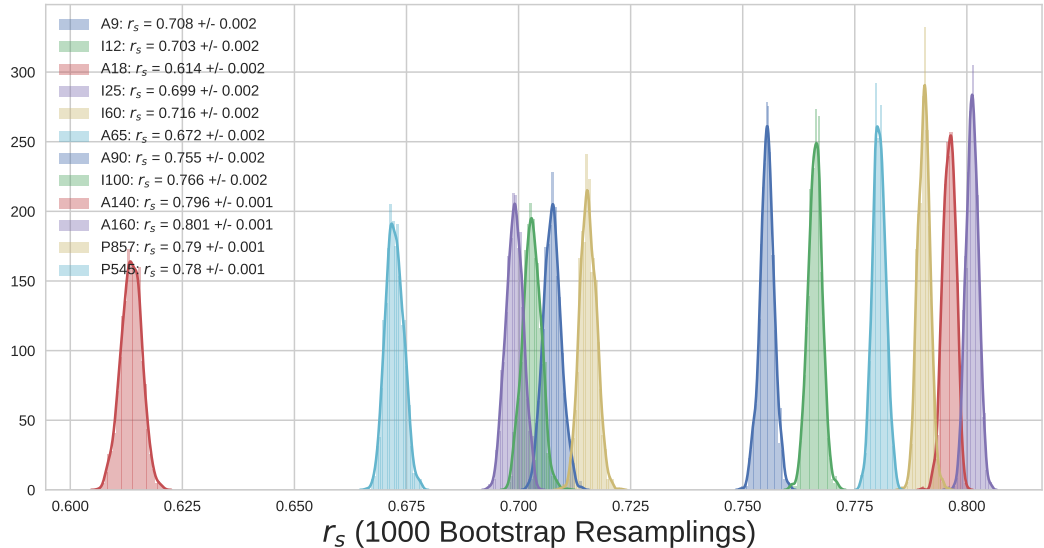


Figure 4.8: .

the computational challenges presented by a well-sampled bootstrap of all 700,000 pixels in the full sky. Because the mask applied here leaves us with approximately 1/7 of the sky, a bootstrap of N iterations with N pixels becomes tractable (though ideally we would prefer $n_{iterations} > n_{samples}$). We show the comparison only for the AME_{var} component also due to computational constraints. The r_s distributions for each IR band vs. AME are shown in Fig. 4.8

4.4 Spatial variation of correlations

To understand how these trends may vary across the sky, we produce an all-sky maps of r_s for AME vs. IR emission, without employing any pixel mask. From the NSIDE 256 input maps of AME and 4 IR wavelength maps, we produce NSIDE 8 maps of r_s . These maps are shown in Figs. 4.9 and 4.10.

940

4.5 Discussion

4.5.1 AME:Dust

As noted in Ch. 1, previous studies found that the AME generally correlates at dust-related IR wavelengths (Ysard et al. 2010; Planck Collaboration et al. 2014d; Hensley et al. 2016). We see the same overall pattern in the present study.

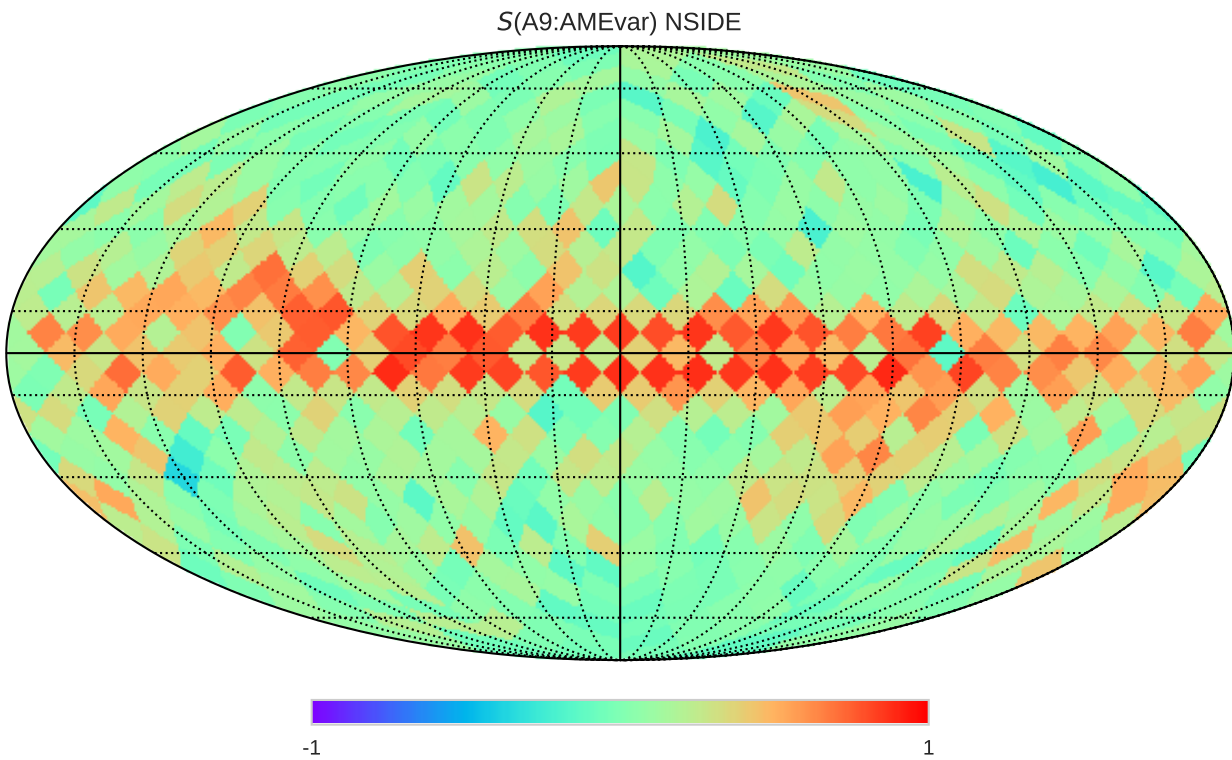


Figure 4.9: Spatial map of r_s between the AME and IR intensity for 4 bands: 9 μm , 12 μm , 25 μm , and 140 μm . r_s is calculated for all NSIDE 256 pixels within each NSIDE 8 pixel-sized bin.

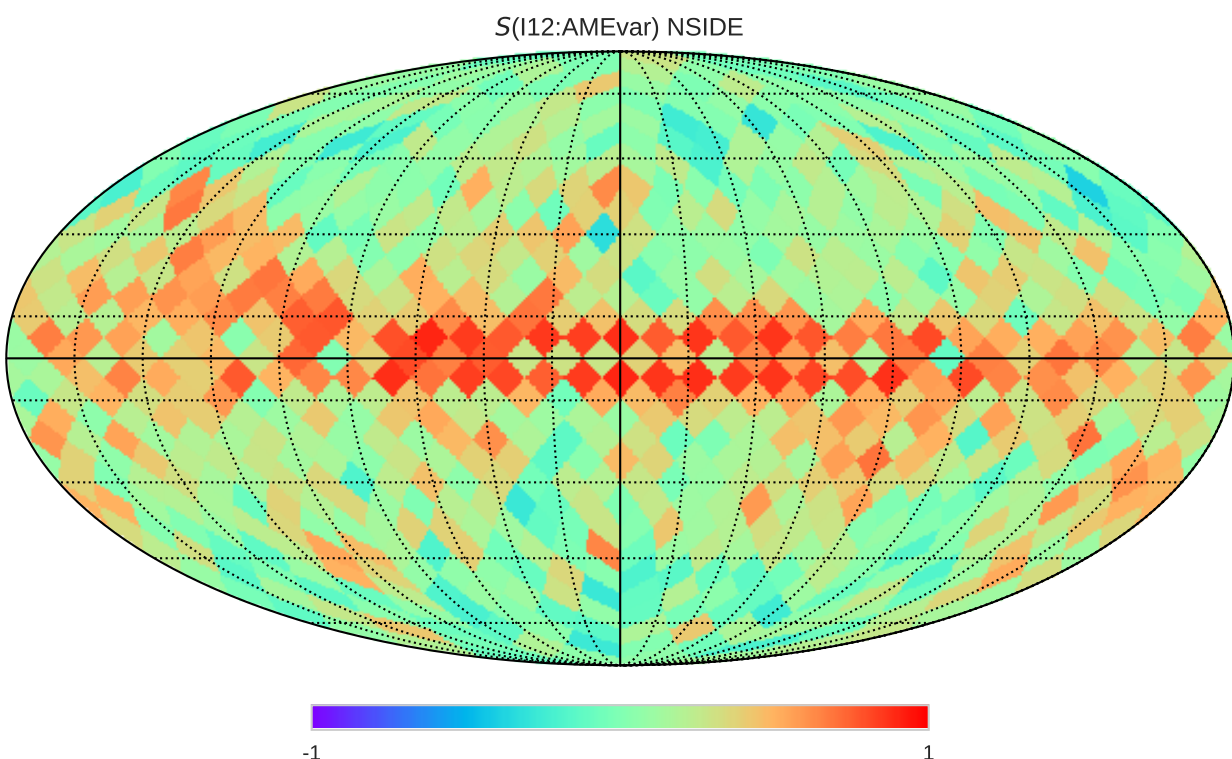


Figure 4.10

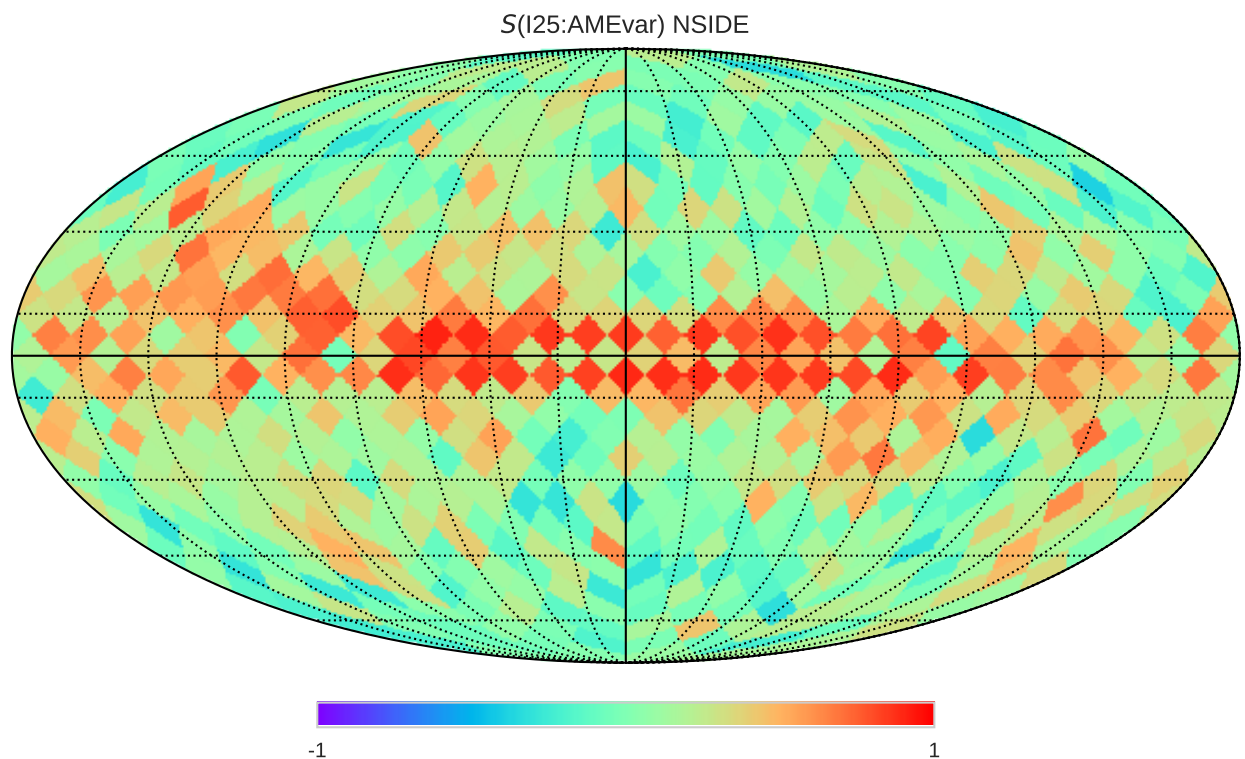


Figure 4.11

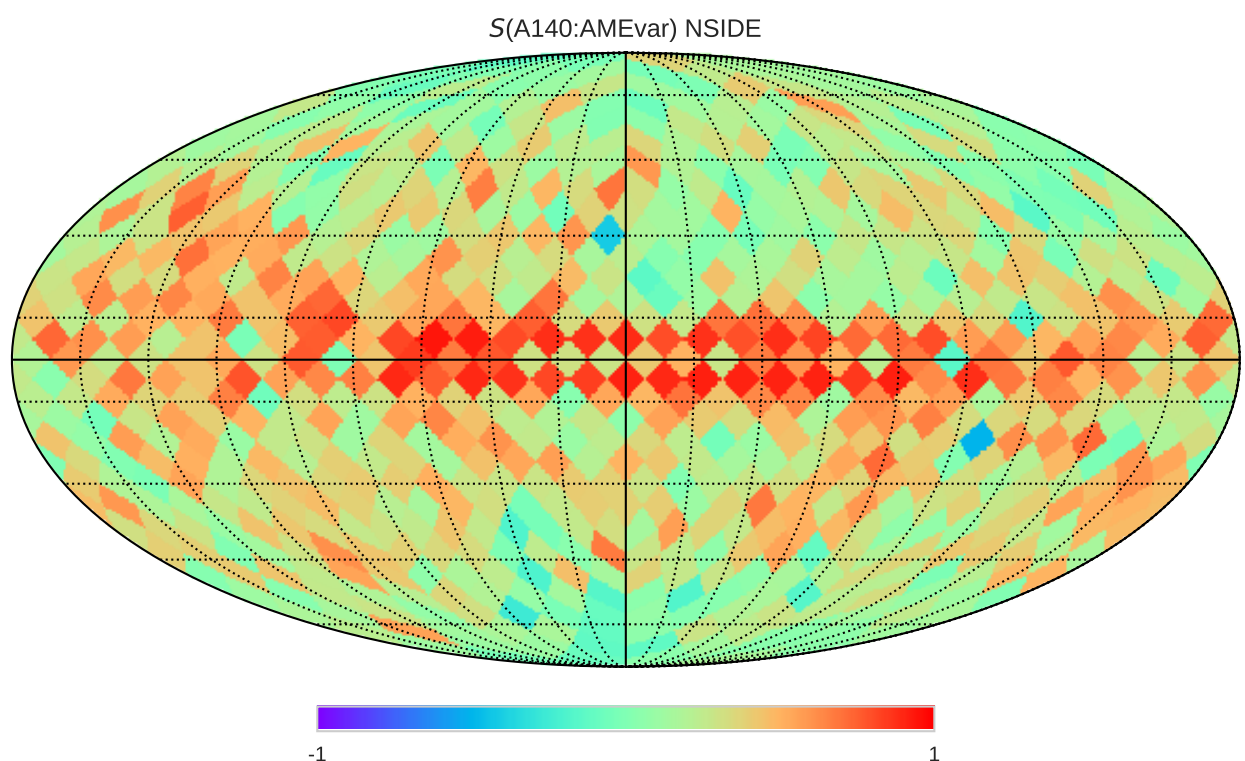


Figure 4.12

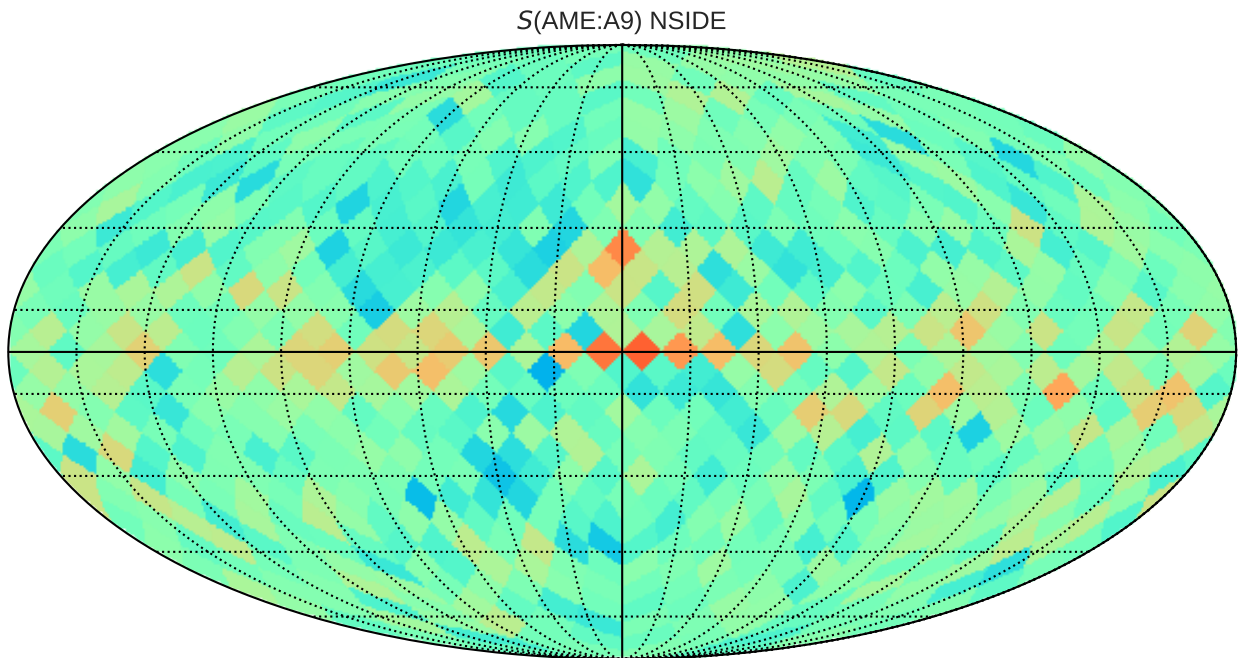


Figure 4.13: Spatial map of r_s between the AME and IR intensity as in Fig. ??, but with the AME and IR maps first normalized by dust radiance R .

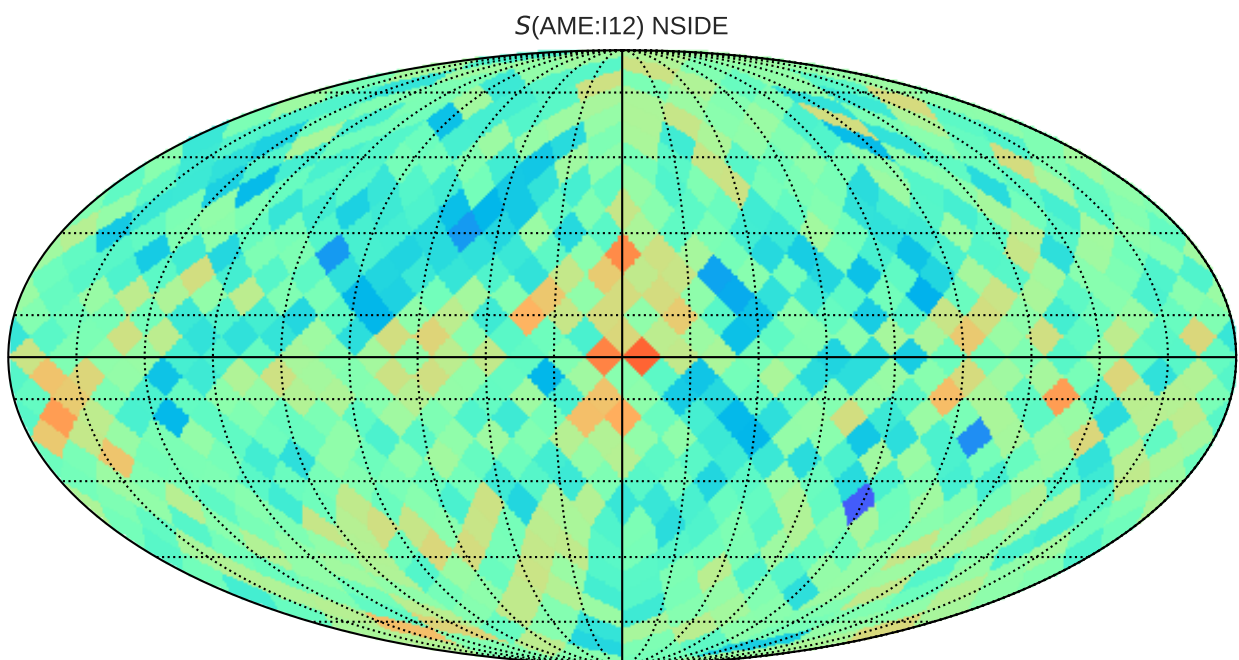


Figure 4.14

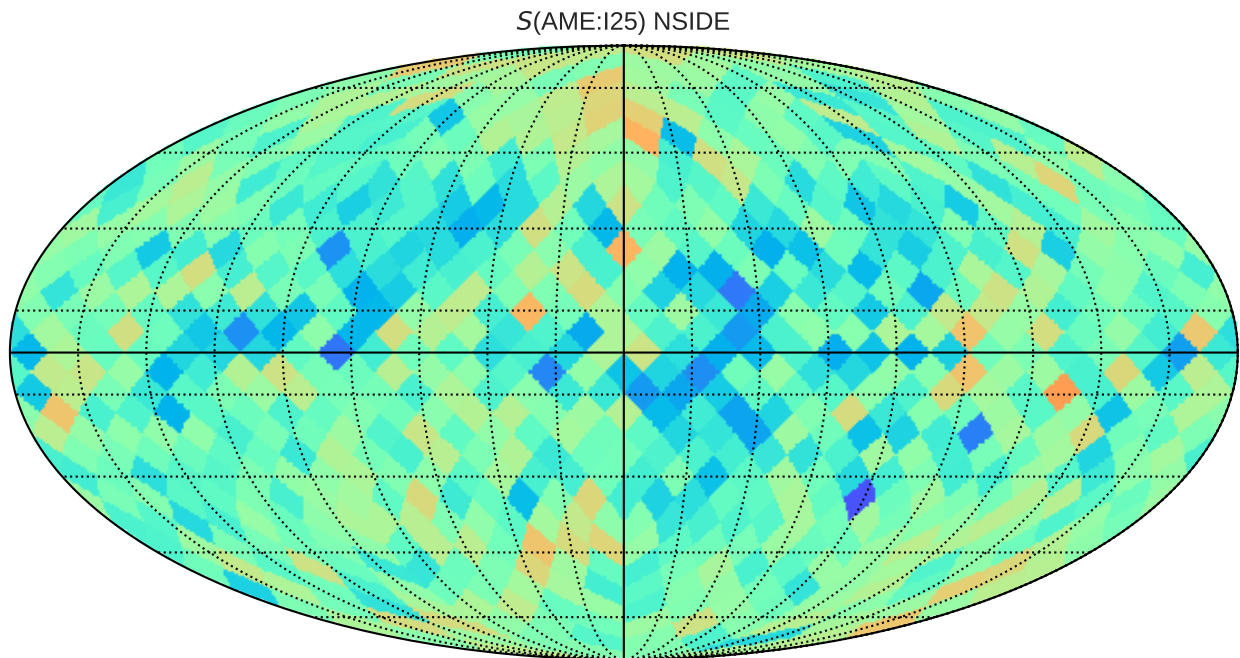


Figure 4.15

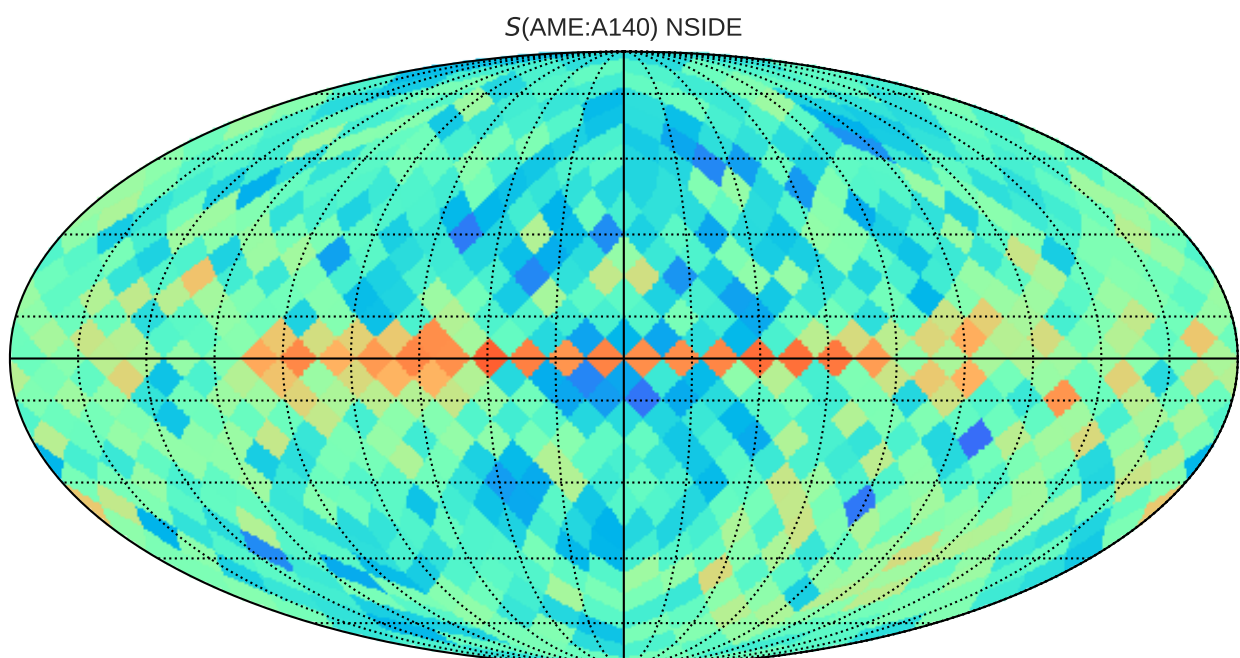


Figure 4.16

946 In our all-sky comparison, we find a first-order correlation between IR intensity and AME inten-
947 sity, for each of the 12 wavelengths sampled. This is again consistent with the previous investigations
948 of the AME cited above, in that the FIR emission shows the tightest correlation with the AME inten-
949 sity.

950 In testing for a second-order correlation, we divided the IR intensities and AME intensity by
951 the dust radiance, and again performed the band-by-band all-sky comparison. There is evidence of
952 a residual correlation between I_{MIR} and I_{AME}/R . Unsurprisingly, the strong correlation between
953 I_{FIR} and I_{AME} disappears when scaling by R , as the the FIR bands are dominated by thermal dust
954 emission. In this case, we again find no evidence of an improved correlation for the PAH-dominated
955 bands.

956 The closeness of the correlation coefficients found here is consistent with the results of the IRAS
957 vs. AME correlation test result from Planck Collaboration et al. (2014d). They found that the corre-
958 lation coefficient among the 4 IRAS bands (12, 25, 60, and 100 μm) differ from one another only by
959 about 5%, across the whole set of 98 regions. The trend of AKARI MIR and FIR data vs. the AME
960 does not disagree with their IRAS comparison. This work adds that bands longer than IRAS 100 μm
961 also correlate strongly with AME, especially the two Planck/HFI bands used.

962 4.5.2 AME:PAH

963 Each of the bands sampled show correlation with the AME, however the FIR bands always show the
964 strongest correlation. In fact, the correlation pattern of AME vs. each of the IR bands, very strongly
965 resembles the correlation results of the FIR vs. all of the other maps. This is readily apparent from
966 the pixel-density plots in Figs. 4.1 and 4.4, wherein the FIR bands pixels show a very similar density
967 profile vs. the AME. In attempting to factor out this first-order correlation, dividing the AME and IR
968 intensities by U for each pixel, we find the there is still a residual correlation between the MIR bands
969 and the AME.

970 4.5.3 AME: T, G_0

971 According to spinning dust theory outlined in Draine & Lazarian (1998a) and in subsequent works
972 by Ysard & Verstraete (2010), the AME profile and intensity will depend in part on the ISRF- but as
973 is well-stated in Hensley & Draine (2017), exactly how the ISRF will affect the AME SED is a more
974 complicated question. Absorbed starlight photons may be able to rotationally excite the carriers, but

975 if an enhanced ISRF leads to increased dust heating, then the increased IR emission can rotationally
976 de-excite the carriers. Moreover the ISRF affects not only the dust temperature but ionization of the
977 carriers.

978 **4.5.4 Microwave foreground component separation**

979 There are known degeneracies between the foreground parameters of the COMMANDER maps
980 (spinning-dust, and free-free, synchrotron components as described in Planck Collaboration et al.
981 (2016b).) This can be demonstrated by comparing the ratio map of the PCXV intensity to thermal
982 dust intensity.

⁹⁸³ A Note on Data Dimensionality

⁹⁸⁴ While we aim to demonstrate the application of high dimensionality in these studies, we do not wish
⁹⁸⁵ to mislead readers that we have assembled a 12-dimensional photometric dataset, simply because we
⁹⁸⁶ have 12 wavebands. This statement may seem nonsensical at first, but makes sense when we consider
⁹⁸⁷ the covariance of the data. Just from the outside, and our faithful belief that FIR dust emission looks
⁹⁸⁸ something like a blackbody, or modified blackbody, or at the very least we can agree that emission
⁹⁸⁹ from dust in thermal equilibrium would produce some sort of peaked continuum emission spanning
⁹⁹⁰ multiple photometric bands' width. If we agree on this point, then it follows naturally that said bands
⁹⁹¹ would be highly correlated with one another. This means that the number of truly independent data
⁹⁹² dimensions is not only lower than the number of bands used here, it is much lower.

⁹⁹³ Fig. 17 shows the % of variance in the data retained by the first n principal components. Principal
⁹⁹⁴ components are found essentially by first finding the covariance matrix of the input data, and then
⁹⁹⁵ diagonalizing this matrix- the eigenvectors will be the basis vectors of each principal component. The
⁹⁹⁶ eigenvalues will give the explained covariance per component. Applied in this manner, the compo-
⁹⁹⁷ nents may not necessarily have a clear physical interpretation, but from a data analytics perspective
⁹⁹⁸ we can at least assess the redundancies in our data. Thus from Fig. 17, and choosing an arbitrary
⁹⁹⁹ covariance "acceptable loss" of 99%, our photometric data set steeply reduces to 3 dimensions. The
¹⁰⁰⁰ first component contains 98% of the total variance.

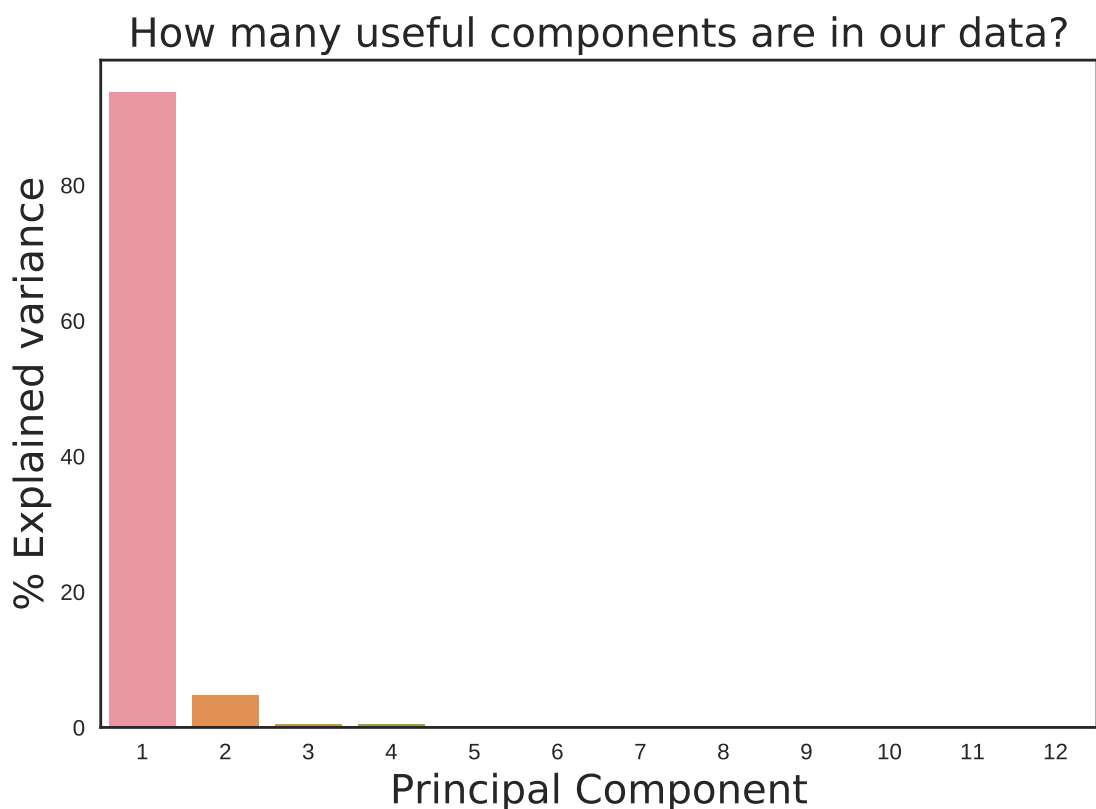


Figure 17: Explained variance decline for principal component analysis performed on a set of 12 all-sky infrared maps. The first three components account for over 99% of the total variance. The PCA fit is performed on the whole sky, after whitening the data, using the “scikitlearn”

1001 This research made use of Montage. It is funded by the National Science Foundation under Grant
1002 Number ACI-1440620, and was previously funded by the National Aeronautics and Space Admin-
1003 istration's Earth Science Technology Office, Computation Technologies Project, under Cooperative
1004 Agreement Number NCC5-626 between NASA and the California Institute of Technology

1005 References

- 1006 Ali-Haimoud, Y. 2010, SpDust/SpDust.2: Code to Calculate Spinning Dust Spectra, Astrophysics Source Code
1007 Library
- 1008 Ali-Haïmoud, Y. 2014, MNRAS, 437, 2728
- 1009 Ali-Haïmoud, Y., Hirata, C. M., & Dickinson, C. 2009, MNRAS, 395, 1055
- 1010 Allain, T., Leach, S., & Sedlmayr, E. 1996a, A&A, 305, 602
- 1011 —. 1996b, A&A, 305, 616
- 1012 Allamandola, L. J., Tielens, A. G. G. M., & Barker, J. R. 1985, ApJ, 290, L25
- 1013 AMI Consortium et al. 2012, MNRAS, 423, 1463
- 1014 Andrews, H., Boersma, C., Werner, M. W., Livingston, J., Allamandola, L. J., & Tielens, A. G. G. M. 2015,
1015 ApJ, 807, 99
- 1016 Aran, A. B. 2009, PhD thesis, UNIVERSIDAD AUTONOMA DE MADRID
- 1017 Atwood, W. B., et al. 2009, ApJ, 697, 1071
- 1018 Bennett, C. L., et al. 2003a, ApJS, 148, 97
- 1019 —. 2003b, ApJS, 148, 1
- 1020 BICEP2 Collaboration et al. 2014, Physical Review Letters, 112, 241101
- 1021 Boggess, N. W., et al. 1992, ApJ, 397, 420
- 1022 Bonnarel, F., et al. 2000, A&AS, 143, 33
- 1023 Bot, C., Ysard, N., Paradis, D., Bernard, J. P., Lagache, G., Israel, F. P., & Wall, W. F. 2010, A&A, 523, A20
- 1024 Boulanger, F., Baud, B., & van Albada, G. D. 1985, A&A, 144, L9
- 1025 Compiègne, M., et al. 2011, A&A, 525, A103
- 1026 Cunha, K., & Smith, V. V. 1996, A&A, 309, 892
- 1027 Dale, D. A., Helou, G., Contursi, A., Silbermann, N. A., & Kolhatkar, S. 2001, ApJ, 549, 215
- 1028 de Oliveira-Costa, A., Kogut, A., Devlin, M. J., Netterfield, C. B., Page, L. A., & Wollack, E. J. 1997, ApJ,
1029 482, L17
- 1030 de Oliveira-Costa, A., et al. 2002, ApJ, 567, 363
- 1031 Dickinson, C., Paladini, R., & Verstraete, L. 2013, Advances in Astronomy, 2013, 1
- 1032 Doi, Y., et al. 2015, PASJ, 67, 50
- 1033 Draine, B. T. 2011, Physics of the Interstellar and Intergalactic Medium

REFERENCES

- 1034 Draine, B. T., & Hensley, B. 2013, ApJ, 765, 159
- 1035 Draine, B. T., & Lazarian, A. 1998a, ApJ, 494, L19
- 1036 —. 1998b, ApJ, 508, 157
- 1037 —. 1999, ApJ, 512, 740
- 1038 Draine, B. T., & Li, A. 2001a, ApJ, 551, 807
- 1039 —. 2001b, ApJ, 551, 807
- 1040 —. 2007a, ApJ, 657, 810
- 1041 —. 2007b, ApJ, 657, 810
- 1042 Duerr, R., Imhoff, C. L., & Lada, C. J. 1982, ApJ, 261, 135
- 1043 Dwek, E. 1986, ApJ, 302, 363
- 1044 Dwek, E., et al. 1997, ApJ, 475, 565
- 1045 Efron, B. 1979, Ann. Statist., 7, 1
- 1046 Erickson, W. C. 1957, ApJ, 126, 480
- 1047 Feigelson, E. D., & Babu, G. J. 2013, Statistical Methods for Astronomy, ed. T. D. Oswalt & H. E. Bond, 445
- 1048 Ferrara, A., & Dettmar, R.-J. 1994, ApJ, 427, 155
- 1049 Finkbeiner, D. P., Schlegel, D. J., Frank, C., & Heiles, C. 2002, ApJ, 566, 898
- 1050 Flauger, R., Hill, J. C., & Spergel, D. N. 2014, J. Cosmology Astropart. Phys., 8, 039
- 1051 Galliano, F., et al. 2011, A&A, 536, A88
- 1052 Giard, M., Lamarre, J. M., Pajot, F., & Serra, G. 1994, A&A, 286
- 1053 Gillett, F. C., Forrest, W. J., & Merrill, K. M. 1973, ApJ, 183, 87
- 1054 Gillett, F. C., Forrest, W. J., Merrill, K. M., Soifer, B. T., & Capps, R. W. 1975, ApJ, 200, 609
- 1055 Górski, K. M., Hivon, E., Banday, A. J., Wandelt, B. D., Hansen, F. K., Reinecke, M., & Bartelmann, M. 2005,
1056 ApJ, 622, 759
- 1057 Hanson, D., et al. 2013, Physical Review Letters, 111, 141301
- 1058 Haslam, C. G. T., Salter, C. J., Stoffel, H., & Wilson, W. E. 1982, A&AS, 47, 1
- 1059 Hensley, B. S., & Draine, B. T. 2017, ApJ, 836, 179
- 1060 Hensley, B. S., Draine, B. T., & Meisner, A. M. 2016, The Astrophysical Journal, 827, 45
- 1061 Hoang, T., Vinh, N.-A., & Quynh Lan, N. 2016, ApJ, 824, 18
- 1062 Hony, S., Van Kerckhoven, C., Peeters, E., Tielens, A. G. G. M., Hudgins, D. M., & Allamandola, L. J. 2001,
1063 A&A, 370, 1030
- 1064 Hoyle, F., & Wickramasinghe, N. C. 1970, Nature, 227, 473
- 1065 Ishihara, D., et al. 2007, PASJ, 59, S443
- 1066 —. 2010, A&A, 514, A1

- 1067 Israel, F. P., Wall, W. F., Raban, D., Reach, W. T., Bot, C., Oonk, J. B. R., Ysard, N., & Bernard, J. P. 2010,
1068 *A&A*, 519, A67
- 1069 Johnson, H. L. 1966, *ARA&A*, 4, 193
- 1070 Jones, A. P. 2009, *A&A*, 506, 797
- 1071 Jones, A. P., Fanciullo, L., Köhler, M., Verstraete, L., Guillet, V., Bocchio, M., & Ysard, N. 2013, *A&A*, 558,
1072 A62
- 1073 Jones, A. P., Köhler, M., Ysard, N., Bocchio, M., & Verstraete, L. 2017, *A&A*, 602, A46
- 1074 Kawada, M., et al. 2007a, *PASJ*, 59, S389
- 1075 —. 2007b, *PASJ*, 59, 389
- 1076 Kelsall, T., et al. 1998, *ApJ*, 508, 44
- 1077 Kessler, M. F., et al. 1996, *A&A*, 315, L27
- 1078 Koenig, X., Hillenbrand, L. A., Padgett, D. L., & DeFelippis, D. 2015, *AJ*, 150, 100
- 1079 Kogut, A., Banday, A. J., Bennett, C. L., Gorski, K. M., Hinshaw, G., & Reach, W. T. 1996, *ApJ*, 460, 1
- 1080 Kondo, T., et al. 2016, *AJ*, 151, 71
- 1081 Lau, R. M., Herter, T. L., Morris, M. R., Li, Z., & Adams, J. D. 2015, *Science*, 348, 413
- 1082 Leach, S. M., et al. 2008, *A&A*, 491, 597
- 1083 Leitch, E. M., Readhead, A. C. S., Pearson, T. J., & Myers, S. T. 1997, *ApJ*, 486, L23
- 1084 Li, A., & Draine, B. T. 2001, *ApJ*, 554, 778
- 1085 Lovas, F. J., McMahon, R. J., Grabow, J.-U., Schnell, M., Mack, J., Scott, L. T., & Kuczkowski, R. L. 2005,
1086 *Journal of the American Chemical Society*, 127, 4345, pMID: 15783216
- 1087 Maddalena, R. J. 1986, PhD thesis, National Aeronautics and Space Administration. Goddard Inst. for Space
1088 Studies, New York, NY.
- 1089 Maddalena, R. J., & Morris, M. 1987, *ApJ*, 323, 179
- 1090 Martin, D. C., et al. 2005, *ApJ*, 619, L1
- 1091 Mathis, J. S., Mezger, P. G., & Panagia, N. 1983, *A&A*, 128, 212
- 1092 Mathis, J. S., Rumpl, W., & Nordsieck, K. H. 1977, *ApJ*, 217, 425
- 1093 Mattila, K., Lemke, D., Haikala, L. K., Laureijs, R. J., Leger, A., Lehtinen, K., Leinert, C., & Mezger, P. G.
1094 1996, *A&A*, 315, L353
- 1095 Merrill, K. M., Soifer, B. T., & Russell, R. W. 1975, *ApJ*, 200, L37
- 1096 Miville-Deschénes, M.-A., & Lagache, G. 2005, *ApJS*, 157, 302
- 1097 Murakami, H., et al. 1996, *PASJ*, 48, L41
- 1098 —. 2007, *PASJ*, 59, 369
- 1099 Murdin, P., & Penston, M. V. 1977, *MNRAS*, 181, 657
- 1100 Neugebauer, G., et al. 1984, *ApJ*, 278, L1

REFERENCES

- 1101 Ochsendorf, B. B., Brown, A. G. A., Bally, J., & Tielens, A. G. G. M. 2015, *ApJ*, 808, 111
- 1102 Onaka, T. 2000, *Advances in Space Research*, 25, 2167
- 1103 Onaka, T., Mizutani, M., Tomono, D., Shibai, H., Nakagawa, T., & Doi, Y. 1999, in *ESA Special Publication*,
1104 Vol. 427, *The Universe as Seen by ISO*, ed. P. Cox & M. Kessler, 731
- 1105 Onaka, T., Yamamura, I., Tanabe, T., Roellig, T. L., & Yuen, L. 1996, *PASJ*, 48, L59
- 1106 Onaka, T., et al. 2007, *PASJ*, 59, 401
- 1107 Ootsubo, T., et al. 2016, *PASJ*, 68, 35
- 1108 Paladini, R., Ingallinera, A., Aglizzo, C., Tibbs, C. T., Noriega-Crespo, A., Umana, G., Dickinson, C., &
1109 Trigilio, C. 2015, *ApJ*, 813, 24
- 1110 Pavlyuchenkov, Y. N., Kirsanova, M. S., & Wiebe, D. S. 2013, *Astronomy Reports*, 57, 573
- 1111 Perrott, Y. C., et al. 2018, *MNRAS*, 473, 1157
- 1112 Pettit, E., & Nicholson, S. B. 1922, *ApJ*, 56, 295
- 1113 —. 1928, *ApJ*, 68
- 1114 Pilleri, P., Montillaud, J., Berné, O., & Joblin, C. 2012, *A&A*, 542, A69
- 1115 Planck Collaboration et al. 2011a, *A&A*, 536, A1
- 1116 —. 2011b, *A&A*, 536, A20
- 1117 —. 2014a, *A&A*, 571, A1
- 1118 —. 2014b, *A&A*, 571, A8
- 1119 —. 2014c, *A&A*, 571, A12
- 1120 —. 2014d, *A&A*, 565, A103
- 1121 —. 2016a, *A&A*, 594, A1
- 1122 —. 2016b, *A&A*, 594, A10
- 1123 —. 2016c, *A&A*, 594, A25
- 1124 —. 2016d, *A&A*, 586, A132
- 1125 —. 2017, *A&A*, 599, A51
- 1126 Puget, J. L., Leger, A., & Boulanger, F. 1985, *A&A*, 142, L19
- 1127 Purcell, E. M. 1976, *ApJ*, 206, 685
- 1128 Reynolds, R. J., Tufte, S. L., Haffner, L. M., Jaehnig, K., & Percival, J. W. 1998, *PASA*, 15, 14
- 1129 Russell, R. W., Soifer, B. T., & Willner, S. P. 1977, *ApJ*, 217, L149
- 1130 Sakata, A., Wada, S., Tanabe, T., & Onaka, T. 1984, *ApJ*, 287, L51
- 1131 Sellgren, K. 1984, *ApJ*, 277, 623
- 1132 Sellgren, K., Werner, M. W., & Dinerstein, H. L. 1983, *ApJ*, 271, L13
- 1133 Sheehy, C., & Slosar, A. 2017, ArXiv e-prints

-
- 1134 Skrutskie, M. F., et al. 2006, AJ, 131, 1163
- 1135 Sodroski, T. J., Dwek, E., Hauser, M. G., & Kerr, F. J. 1987, ApJ, 322, 101
- 1136 Sodroski, T. J., et al. 1994, ApJ, 428, 638
- 1137 Takita, S., et al. 2015, PASJ, 67, 51
- 1138 Thorwirth, S., Theulé, P., Gottlieb, C. A., McCarthy, M. C., & Thaddeus, P. 2007, ApJ, 662, 1309
- 1139 Tibbs, C. T., et al. 2011, MNRAS, 418, 1889
- 1140 Truemper, J. 1982, 2, 241
- 1141 von Hausegger, S., & Liu, H. 2015, J. Cosmology Astropart. Phys., 8, 029
- 1142 Weingartner, J. C., & Draine, B. T. 2001, ApJ, 548, 296
- 1143 Werner, M. W., et al. 2004, ApJS, 154, 1
- 1144 Wright, E. L., et al. 2010, AJ, 140, 1868
- 1145 Young, E. T., et al. 2012, ApJ, 749, L17
- 1146 Ysard, N., Juvela, M., & Verstraete, L. 2011, A&A, 535, A89
- 1147 Ysard, N., Miville-Deschénes, M. A., & Verstraete, L. 2010, A&A, 509, L1
- 1148 Ysard, N., & Verstraete, L. 2010, A&A, 509, A12